52

Whispering-gallery-mode dye laser emission from liquid in a capillary fiber

J. C. Knight

Thesis Presented for the degree of
DOCTOR OF PHILOSOPHY
in the Department of Physics
UNIVERSITY OF CAPE TOWN
August, 1993

Abstract

The nature of optical whispering-gallery-mode resonances in a layered microcylinder is investigated numerically by studying the scattering characteristics and the internal electromagnetic fields of a normally-illuminated cladded dielectric fiber calculated using the boundary-value method. Computed resonant mode configurations are compared to the better-known results for homogeneous spheres and cylinders and coated spheres. It is shown that high-Q whispering-gallery-mode resonances can be supported by the curved interface between the core and cladding regions of a layered fiber if the core refractive index is sufficiently greater than that of the outer layer, and that these modes can be directly related to the so-called morphology-dependent resonances of a homogeneous cylinder of the same size and relative refractive index as the fiber core. The implications of these resonant modes for inelastic optical processes are made clear by developing a model for optical emissions from a molecule in the core of a capillary fiber. The results of the model show that the transition rates of molecules in the fiber core and near to the core/cladding interface are enhanced at frequencies corresponding to cavity resonances. It is shown experimentally that these high-Q cavity modes can be excited to above the threshold for laser emission by providing gain in the fiber core material. We have used a refractive dye-doped solvent as a gain medium and a fused-silica capillary to form the resonant cavity. Upon optical excitation of the dye by illuminating the fiber normally with the green beam from a frequency-doubled Nd:YAG laser, laser emission is emitted from the fiber core in the plane perpendicular to the fiber axis. We explain the novel spatial and spectral dependences of the laser emission in terms of the calculated frequencies and Q-values of the resonant cavity modes and the bulk properties of the cavity medium. We show that the thresholds observed in the laser system can be explained using a simplified rate-equation approach, and that this also explains some of the other observed features of the emissions. The heating of the dye solvent during a laser pulse has an observable effect on the resonance mode locations due to the temperature dependence of the refractive index. We demonstrate the use of observed laser spectra to determine the size and taper of the capillary fiber core.

Acknowledgements

I am grateful to my supervisors Professor G.N. Robertson and Dr. H.S.T. Driver for enabling me to do this work. Their knowledge and insight has inspired me, while their assistance and suggestions have always been useful. On several occasions, their help has proved invaluable. They have also ensured that I have been financially secure, enabling me to spend the maximum time on my thesis work. The Department of Physics at the University of Cape Town has proved to be a pleasant and stimulating environment in which to work – in particular the past and present members of the laser physics group, including Dr. R.J. Hutcheon, have been a pleasure to work with. The secretarial and workshop staff in the department have provided a friendly and professional atmosphere. Advice and extensive assistance was provided by Mr. D. Gerneke of the Electron Microscope Unit at U.C.T. The computing facilities at the university have been a great help, and their able and considerate management by the staff of Information Technology Services have made them all the more useful. The Foundation for Research Development has provided financial support for which I am most grateful. Lastly I would like to thank my parents for their interest and Di Dalgliesh for her tolerance, her humour and her company.

Contents

Chapter 1

Introduction

The light-scattering properties of fine particles must surely rate as one of the most enduring topics of scientific study. Natural manifestations of light-scattering phenomena are familiar to everyone, and have attracted the interest of scientists for centuries. The remarkable richness of the interaction of light with microparticles is demonstrated by the fact that light scattering is still a very active field of research. The development of the electromagnetic theory of light toward the end of the 19'th century provided a substantial boost to efforts to understand light-scattering phenomena, and even today the techniques of classical electromagnetism are arguably the most useful tool in the theoretical investigation of light-scattering. Similarly, the development of the laser as an intense, directional and spectrally pure light source has opened new vistas in experimental light scattering over the past three decades. Together, these two achievements have seen light scattering develop into a technologically useful science being routinely used for the morphological and chemical characterization of microparticles and microdroplets and their effect upon radiative transfer phenomena. With the modern trend towards miniaturization and the advent of optical communication and computing devices, this development looks set to continue for the forseeable future.

Many of the technological applications of light-scattering are based upon boundary-value solutions to the problem of the scattering of a plane wave – primarily the Lorenz-Mie theory in which the scattering centre is assumed to be a homogeneous

sphere. Recent research in light-scattering phenomena has been concentrated in two fields: one of these is the reformulation of the Lorenz-Mie scattering problem and its solution to describe the illumination of a more general (non-spherical or irregular) particle by a gaussian laser beam. The other fast-developing area of research, and the one with which this thesis is concerned, is the inelastic light-scattering properties of microparticles. These differ markedly from those of bulk material, primarily because of the complex electromagnetic field configurations which can occur within microparticles. Inelastic and non-linear optical processes in bulk media have been the subject of intense investigation over the past three decades and have become a most exciting and fast-moving field with extensive technological applications. The non-linear optical properties of microparticles are of immediate interest because of their potential use for microparticle or microdroplet characterization, because of their role in the interaction of high-energy laser beams with the atmospheric aerosol and also for the development of ultra-small optical devices such as microlasers and high-density memories for optical computing and communication, although the full-scale implementation of the more sophisticated of these applications appears to be still some way from fruition.

The majority of the experimental work which has been reported on non-linear optical properties of fine particles has been performed using liquid droplets in the size range $10 - 100\mu$m illuminated with an Nd:YAG or an argon-ion laser. Liquid droplets have several advantages for such studies: the results are directly relevant for experiments involving aerosols or fuel sprays, surface tension in the droplets causes them to form near-perfect spheres, and the internal fields at the pump frequency are in principle exactly calculable using the Lorenz-Mie theory. In addition, such internal-field calculations have been used to demonstrate some of the important modal features in the inelastic scattering process. This is possible because the fields within the microparticle must satisfy the same boundary conditions whether the light is incident from outside the particle as in the elastic-scattering case or has its origin in some inelastic scattering interaction with the particle medium itself. Thus it has been established that the natural high-Q resonances of the microdroplet cavity play an important role in the observable non-linear optical processes; the long photon life-

times and enhanced fields coupled with the increased transition rates for molecules due to the altered density of final states within the resonant cavity have the effect of reducing the thresholds for non-linear optical processes to well below those observed in bulk material. One of the simplest experiments in which these effects may be observed is the microdroplet laser in which a dye-doped liquid droplet, either suspended or flowing freely in a gas, is illuminated with a high-power laser beam. The resonant modes of the natural cavity formed by the droplet may be brought above the threshold for laser emission in a manner completely analogous to that occurring in a conventional laser cavity. These resonant modes correspond to counterpropagating travelling waves confined to near to the droplet surface and traversing the droplet perimeter by repeated total internal reflection and are called morphology-dependent resonances (MDR's), or sometimes optical whispering-gallery modes in analogy with the acoustic modes described by Rayleigh in 1891. Similar modal features have been predicted to occur in the cylindrical cavity formed by a homogeneous dielectric fiber, and corresponding peaks have been observed in the fluorescent spectra from such fibers. In this thesis, we present the results of an investigation into such resonances in a capillary fiber, and the effect which these have on the inelastic scattering processes observable from a liquid in the core of such a fiber. We have concentrated our investigation upon the laser emission observable from the liquid when it contains a fluorescent dye, with the aim of elucidating the physical processes in microparticle lasers in general. There are several advantages to studying such a system rather than the better-known microdroplet laser: one of these is the permanence of our capillary fiber when compared to a moving, volatile liquid droplet. This enables the study of cavity features under different experimental conditions over an indefinite period of time, and physical examination (by e.g. electron microscopy) of the sample.

The nonlinear optical properties of materials in the form of fibers are currently of great interest, particularly in the field of optical communications, where the development of rare earth-doped fiber lasers and fiber amplifiers has necessitated the consideration of the effect of confinement within a cylindrical cavity upon the transition rates and fluorescent lifetimes of molecules. Some of the results of our investigation will also be of use to chemists using the analytical technique of capillary gel

electrophoresis, and to those interested in the characterization of capillary core size and uniformity.

This thesis begins with an introduction to optical resonances and inelastic light-scattering from microparticles, which details the background to the current state of knowledge and reviews the literature, concentrating upon the developments of the past decade. Thereafter (chapter 3) we derive the solution to the boundary-value problem of the elastic scattering of a plane wave incident normally upon an infinite coated cylinder. We describe the implementation of this solution in FORTRAN programs to calculate the scattering characteristics and the internal and external near-field patterns for such a cylinder. A range of numerical results are presented and discussed, with particular attention to parameters relevant to the experiments to be described. We next extend a known model for inelastic light scattering from a molecule embedded in a homogeneous fiber to describe the emissions from a molecule in the core of a capillary fiber. Numerical results from the extended model are interesting because they demonstrate the importance of certain modal features in the fiber core which is not apparent from cursory examination of the corresponding elastic-scattering results.

The main experiments performed and results obtained are presented in chapter 5. The primary spectral features of the observed laser emission are explained in terms of the computed resonance widths and locations: the results are compared with similar published results for dye-doped microdroplets. Experimental values for the laser thresholds for different fibers are compared to those predicted by a simple rate equation analysis. We demonstrate several novel physical effects, and report the use of laser emission from a capillary fiber for fiber core size characterization.

Finally, the important results and their implications for other whispering-gallery-mode lasers are summarized, while we propose further research with the capillary fiber laser.

Chapter 2

Optical resonances and their role in inelastic light-scattering from microparticles: a review

2.1 Overview

The scientific literature on the interaction of light with small particles is vast. In this chapter I shall try to place our work in the proper historical context, while summarizing for the reader those published results which form the immediate background to this thesis. It would be impossible and inappropriate to describe fully the ideas and principles developed in the last 100 years, which have led to the comparatively recent revitalization of the study of light and the development of modern optics; for this, the reader is referred to one of the standard texts on the subject [20]. Instead, this review aims to direct attention towards those aspects of the interaction of light with microparticles which have shown novel effects not observable in bulk matter. Unavoidably, an understanding of some of these aspects requires a familiarity with related results, a familiarity which only a specialist in the field might be expected to have; to keep the review to a reasonable length standard textbooks on the subject have been referenced where appropriate.

I shall deal first with the application of Maxwell's equations to solving optical

elastic-scattering problems by the boundary-value method. This is relevant not only because the boundary-value solution enables the immediate calculation of the internal electromagnetic fields within an absorbing scatterer (which fields serve as the excitation source in inelastic-scattering processes) but also because the boundary-value formalism provides valuable insight into the significant electromagnetic modes within an illuminated microparticle. As will be shown, some of these play important roles in nonlinear optical processes in microparticles. The detailed solutions to boundary-value problems for simple geometries are well known, and are treated in several standard monographs [19, 87, 169]. Consequently such work is outlined only briefly in this review. However, the application of modern high-speed computers to the numerical evaluation of these solutions in the last thirty years has revealed a wealth of detail about the internal and scattered fields, while the use of the laser as an intense, spectrally pure and directional light source has enabled the observation of fine structure in the scattering characteristics of single circularly-symmetric fine particles. Some of this work has particular relevance for this thesis and will be described in some detail.

The review then moves naturally to a more modern application of the boundary-value method: the problem of fluorescence or Raman scattering by a molecule embedded in a microparticle. The microparticle boundary affects both the spectral and the angular distribution of the emitted light, and descriptions of several experiments which were performed in this regard in the late 1970's and early 1980's are included. These experiments led directly to the discovery of lasing and nonlinear optical processes in microparticles. The pioneering experiments in this regard reported by Chang and colleagues at Yale University in the early 1980s have been followed by a multitude of research publications on this and related topics over the past decade. Some of this work will be described in detail, particularly that related to laser emission from microparticles. The review is concluded with a description of some suggested technological applications of the described research.

In none of the above fields is the literature exhaustively surveyed; I have tried to include that work which has had or may have a substantial effect upon the development of the field, as well as that which has been found to be useful during the

course of the work to be described in this thesis. A central theme is the existence of a series of natural electromagnetic resonant modes in circularly symmetric particles. These are traced from their first discovery (as the 'ripple structure' appearing in the boundary-value solutions to elastic light-scattering problems) to their use as high-Q cavity modes supporting nonlinear optical processes in microparticles. It may initially seem inappropriate to have devoted so much attention to reporting examinations of spherical particles, while this thesis concerns primarily optical processes in cylinders, but, as will become apparent with the reading of this review, many of the features of optical processes in spheres are significant in cylinders as well. Indeed, if the work in this thesis on nonlinear optical processes in cylinders contributes to the understanding of such processes in spheres to a fraction of the extent to which previous studies of microspheres assisted our progress, our purpose will have been well served.

2.2 Elastic scattering from microparticles - boundary-value computations and modern experiments

The early development of the boundary-value solution for the scattering of a plane electromagnetic wave of wavelength λ by a spherical microparticle of radius a and refractive index m, known as Mie or Lorenz-Mie scattering, has been surveyed and documented by Logan [119], to whom the reader is referred for an authoritative account. It suffices here to mention that the mathematical tools required for the solution, i.e. the construction of the solution to the scalar wave equation in terms of spherical Bessel functions and spherical harmonics, were developed by Clebsch, while Lorenz derived an exact solution to the problem based on the theory of elastic media. An identical set of equations based upon electromagnetic theory were later published by Mie in his much-cited 1908 paper. The corresponding solution for a cylindrical geometry, i.e. for the scattering of plane waves incident normally upon an infinite circular dielectric cylinder, is simpler, and predates the Mie solution by several years; it is generally attributed to Rayleigh [144]. The corresponding solutions for scattering from a cladded cylinder were given by Tang [162] and by Kerker

and Matijévic [88], and for a coated sphere by Aden and Kerker [5]. These solutions are treated in several standard texts on electromagnetic theory [159], optics [20] and light scattering [19, 87, 169]. Apart from study of the asymptotic cases (particularly that for the far-field) and especially the efficiencies for scattering, absorption and extinction for some selected values of the refractive index m and usually small values of the size parameter $x = 2\pi a/\lambda$, these solutions lay largely unexplored numerically by modern standards for the first half of the 20'th century. The expressions of interest in these solutions consist of summations over the possible electric and magnetic multipoles, each term composed of a coefficient multiplied by a Bessel function, and these need to be evaluated for each value of size parameter and refractive index of interest. As the summations require $\simeq mx$ terms for convergence, the computations of the required functions become laborious, even for small values of x and large step sizes, without the aid of electronic computing devices. The situation is well summarized by Van de Hulst [169], who also makes it clear that early workers did extremely well, considering their limited resources. A remarkable and relevant example of this is in the paper by Mevel [125] (1958) in which the extinction efficiency of a sphere (i.e. the extinction cross-section of a sphere divided by its geometrical cross-section) is correctly calculated for $x < 30$ with limited help from an electronic computer, and the contribution to the curve made by the various multipoles is investigated. This paper clarified the origin of the sharp peaks, known as the 'ripple structure', which appear when the extinction efficiency or the scattering efficiency of a spherical or cylindrical particle is plotted as a function of the size parameter. Van de Hulst [169] had attempted to explain this structure as being due to interference between surface waves and the forward-scattered light. Mevel showed that each fine-structure peak was due to a peak in a single partial wave in the Mie summation, peaks occurring in both the electric and magnetic multipole terms. Furthermore, it was found that more than one resonance of each type may occur in a given partial wave, and these were traced up to $x = 30$. Unfortunately this paper was not widely known until recently.

The application of high-speed digital computers to the electromagnetic boundary-value solutions of light-scattering problems has made this topic more easily acces-

sible. In this regard, it is worth mentioning the work of three sets of authors: the routines described by Dave [54] (1969) have had a lasting impact on light-scattering computations; more modern and efficient implementations of the Lorenz-Mie solution were described by Wiscombe [171], who also suggested how these may be implemented on vector processors; while Bohren and Huffman [19] have published carefully-written and well-documented 'standard' routines for several geometries. Probably the most important features of these routines are the fast and accurate methods for computing values for the Bessel functions of large order and complex argument. A related problem is that of determining the number of terms required for convergence of the partial-wave summations. Straightforward and reliable modern FORTRAN implementations of these ideas are listed by Bohren and Huffman for scattering from a homogeneous sphere and a normally-illuminated cylinder, as well as the numerically more complicated case of a layered sphere. These routines are recommended for their accessibility, reliability and wide distribution.

From the middle of the 1960's, and particularly in the 1970's, detailed computations of the scattering characteristics of individual spheres and cylinders became commonplace. In the same period the use of lasers as intense and spectrally pure sources for light-scattering experiments allowed precise tests of the numerical results. Thus in the mid-1970's, the ripple structure which had been noted in the calculated extinction efficiency of dielectric spheres was investigated more thoroughly for large values of the size parameter by P. Chýlek and co-workers [41, 45], while A. Ashkin *et al.* [12] observed the effects of these multipole resonances in the radiation pressure exerted on a small sphere by a laser beam. Chýlek [41] produced results similar to those of Mevel, and introduced the now common notation of labelling each peak by two mode numbers n and l, being respectively the number of the partial wave in which the peak has its origin and the number of the peak within that partial wave, and a letter a or b, indicating transverse electric or transverse magnetic partial waves respectively. In a given region of x, resonances occur in partial waves with $x < n < mx$, the broadest (highest l) modes having $n \simeq x$. Chýlek investigated [45] the ripple structure in the extinction efficiency of both absorbing and nonabsorbing spheres and found that computed absorption at resonance frequencies was much

greater than at non-resonant values, reinforcing the idea, suggested by Van de Hulst [169], that these peaks were associated with long path lengths around the surface of the particle. A similar effect was later studied by Pluchino [135, 136] using the Aden-Kerker solution for scattering from a coated sphere. He found that a very thin absorbing surface layer on a sphere could play a disproportionate role in increasing the absorption of the particle, and this was shown to be due to the surface nature of the Mie resonances. In Chýlek's 1975 paper, and in more detail in 1990 [42], he derived formulae for the separation in x between neighbouring resonances of the same l values but with n differing by 1. In its asymptotic (and most widely-used) form, this is given by

$$\Delta x = \frac{\arctan(m^2-1)^{\frac{1}{2}}}{(m^2-1)^{\frac{1}{2}}} \tag{2.1}$$

On extending the computations to larger values of x ($x > 100$) [45] it was found that the first-order resonances become increasingly narrow ($\Delta x/x \leq 10^{-7}$) for large values of x. Such resonances were observed in the radiation pressure force on dielectric spheres (liquid droplets) in a series of optical levitation experiments at Bell Telephone Laboratories [11, 12, 13]. Excellent agreement was found between the observed resonance spectrum and the calculations of Chýlek *et al.* [44, 49]. Second and third order modes, with half-widths $\Delta x/x \simeq 10^{-5}$ and 3×10^{-4} respectively were observed in the power required to stably levitate a single 4μm oil droplet, as the wavelength of the levitating laser was varied. Similarly, for a 6μm droplet, only those modes with $\Delta x/x > 10^{-5}$ were observed experimentally, being in this case the third and fourth order modes. Furthermore, Ashkin [11, 13] confirmed the surface-wave interpretation of the resonances by near-field photography of levitated droplets illuminated at resonant and non-resonant frequencies. It was noted that the observation of fine-structure resonances in radiation pressure force spectroscopy enabled both highly accurate measurements of particle properties such as size and evaporation and condensation rates and also constituted a most precise test of the Mie theory.

Ashkin and Dziedzic [13], and also Rosasco and Bennet (1978) [146], investigated the implications of these narrow resonances for optical absorption, scattering and

fluorescence by small particles. Following a survey of trends in the efficiency factors for absorption and scattering, Rosasco and Bennet investigated the resonant internal fields analytically, and pointing out that the internal field resonance structure might be expected to affect not only elastic scattering and absorption by the particle but also the inelastic scattering response of material in microparticle form. Ashkin and Dziedzic noted that these sharp resonances might be expected to influence the spectral dependence of Raman or fluorescent scattered light. Indeed, they speculated (1981) that at 'sufficiently high light intensities one can conceivably obtain lasing on the high-Q resonances of such active particles as dye-impregnated spheres'. Remarkably this effect, which is central to this thesis, had been observed [69] some 20 years earlier (1961) in substantially larger ($d = 1 - 2$mm) spherical samples of CaF_2:Sm^{++}. We shall mention this work again later in this review.

Further insight into the nature of the resonances was provided by Murphy *et al.* [126]. They showed that the calculated and observed peaks in the scattering characteristics corresponded to the excitation of the natural frequencies or eigenmodes of the particle. These are due to circumferentially-travelling waves being 'in phase' after one round trip inside the particle, leading to resonance-enhanced internal fields. They calculated dispersion curves for the phase velocities of surface waves in a sphere, and concluded that the modes are of the 'whispering-gallery' type, i.e. that they are analogous to the acoustic whispering-gallery modes first explained by Rayleigh [145].

Internal fields within illuminated spheres and cylinders are of interest in certain situations because they contribute towards a physical picture of Mie scattering processes and of the fine-structure resonances, as well as providing the 'source function' for inelastic light scattering processes in the particle. The off-resonant fields inside large illuminated spheres and cylinders can be understood in terms of geometrical optics: the curved illuminated surface of the particle acts as a converging lens, causing a peak in the internal electromagnetic fields near the shadow face [55, 57, 130]. The actual focus of this 'lens' falls in the near-field external to the particle for moderate refractive indexes, at a distance which depends on the index [16]. Resonant internal fields in illuminated homogeneous spheres were calculated by Chylek *et al.*

[48], and in normally-illuminated homogeneous cylinders by Owen *et al* [130]. The main features of the resonant fields were the same for both of these: substantial enhancement of the internal fields occurred at resonant frequencies, and this enhancement occurred near to the particle surface. Greater enhancement resulted from narrower resonances for a similar value of size parameter. The significance of the mode numbers n and l is made clear: there are $2n$ peaks in the angular dependence of the resonant field, and l peaks within the particle in the angle-averaged radial dependence. The enhanced fields are less closely confined to the particle surface for higher-order modes, the broadest modes (with $n \sim x$) having resonant fields extending inwards to approximately a/m. The external component of the resonant field outside the sphere or cylinder decreases exponentially away from the surface, particularly sharply for narrow modes. These features of the resonant fields support the physical picture of internal waves undergoing multiple internal reflections from the surface at grazing incidence and being in phase after a round trip. The widths of the modes, or cavity Q-values, are determined by losses through the microparticle walls.

To complete this section of the review on the classical features of morphology-dependent resonances (MDR's) in microparticles, we make brief mention of some analytical investigations of MDRs, some asymptotic approximations, and some studies of MDRs in novel geometries. Two fascinating theoretical works are those by Guimaraes and Nussenzveig [74], and by Agarwal and Dutta Gupta [6]. Guimaraes and Nussenzveig use the analogy between optics and mechanics to develop a complex angular momentum picture of the Mie resonances. In this picture, resonances correspond to quasi-bound states of light, coupled to the external field by tunneling through a centrifugal potential barrier. This interpretation has been investigated more thoroughly by Johnson [86]. Agarwal and Dutta Gupta study the situation where the particulate medium is strongly coupled to the cavity resonances, by allowing the atomic frequency of the medium to be close to a cavity resonance; this results in a splitting of resonances in the scattering characteristics, analogous to the vacuum-field Rabi splitting.

Approximations of locations and widths of resonances for spherical particles

based upon asymptotic expressions for the spherical Bessel functions have been made by several authors. Probert-Jones (1984) used the approximations for large x and n to derive expressions for the locations and widths from the expressions for the partial-wave coefficients a_n and b_n, and found that these gave excellent results for large particles and large orders l [138]. He also derived expressions for the separation of the corresponding TE and TM resonances and rederived the asymptotic formula of Chýlek for $\Delta x = x_{n,l} - x_{n-1,l}$, as well as obtaining several other useful asymptotic results. Schiller and Byer [149] begin their investigation into whispering-gallery modes in large (d = 3.8cm) fused-silica spheres by using expansions of the Bessel functions to express resonance frequencies of the low-l modes. Lam and collaborators [100] derive the same result, and a corresponding expression for the resonance widths. They back the expressions up with a detailed comparison of the results with the exact theory, showing good agreement for low l. Datsyuk [53] follows a rather intuitive approach based on Vainshtein's analytical solution for the whispering-gallery-mode frequencies. As well as formulae for resonance frequencies and widths, he derives a physically appealing but rather simplistic alternative to Chýlek's asymptotic formula for Δx. Psarobas and Leung [139] derive an expression similar to that of Schiller and Byer, but do so by starting with Maxwell's equations, and never relying explicitly on results from Mie theory.

In addition to the studies of whispering-gallery modes in homogeneous spheres and normally-illuminated infinite cylinders, several researchers have addressed more complex geometries. Resonances in the multiple scattering by two normally-illuminated parallel fibers have been discussed by Tsuei and Barber [165] and studied by Schlicht *el al* [150], who have also performed experiments on the related case of a fiber near to a plane mirror. (Here the fiber interacts with its image in the nearby mirror.) Both sets of workers found that the resonance spectrum was altered by the interaction with the nearby fiber, broader modes being affected at greater distances. The two-fiber calculations of Tsuei and Barber show the resonances being completely damped when the two fibers are in contact. Another interesting effect is that the observed and calculated scattering fluctuates as the two fibers approach one another, due to the coherent addition of the light scattered by the two fibers. Similar

effects have been investigated theoretically in microspheres by Fuller [66, 67]. He showed that the single-sphere resonances are broadened and split upon aggregation, leading to a new resonance spectrum for the composite particle. Fuller's 1991 paper [67] contains an interesting historical survey of interactive scattering by spheres and cylinders, and a discussion of methods. This paper also contains many numerical results for different configurations of two spheres.

Fuller [68] has recently (1993) used the methods of multiple (interactive) scattering to treat the problem of scattering by a coated sphere, an approach which promises new insight into the resonant modes of such a system. Coated sphere resonances had previously been studied by Hightower and Richardson [77], using the boundary-value solution of Aden and Kerker. They studied resonances in the core and coating regions for small ($a < 5\mu$m) hollow and coated spheres, and investigated the limiting cases of small core (for coating resonances) and large coating (for core resonances). As might be anticipated from the resonant modal field distributions in a homogeneous sphere, they find that the size or refractive index of the core region has relatively little effect upon the sphere resonances while the core is small; only when the core is sufficiently large to overlap the resonant fields near to the sphere surface are the modes significantly affected.

Several other researchers have investigated the effects of shape and refractive index variations in microspheres on the resonance spectrum. These have included studies of low-order shape deformations [10, 166], small amplitude thermal surface fluctuations [99] and the effect of inclusions and radially dependent refractive indexes [38, 122]. In general, these deviations from a homogeneous sphere have resulted in either a splitting or a broadening of resonances.

2.3 Fluorescence and Raman scattering from microparticles

From 1976 onwards a series of research papers reported the use of a classical model for fluorescence and Raman scattering from microparticles. The model, originally presented by Chew and co-workers for a homogeneous spherical particle [33], de-

scribes the inelastic scattering process as being due to the excitation of a collection of single classical dipoles distributed within the particle, driven by the illuminating wave to radiate at the shifted frequency. By using the boundary-value method and expansions in vector harmonics to solve for the internal and external fields from a single dipole arbitrarily positioned in the particle, the field scattered from a distribution of such dipoles can be computed by numerical superposition, and this superposition can be done coherently [34] or incoherently [90]. It is assumed that the induced dipole moment of an oscillator at the shifted frequency at a given point within the particle will be proportional to the internal electric field at the illuminating frequency at that point. The model was quickly extended to the case of a coated sphere [32]. The solutions for molecules embedded in infinite dielectric cylinders [31] were slightly more complex, because of the need to assume an outgoing spherical wave at large distances. This problem was more easily addressed for a coherently emitting line source of dipoles along the fiber. Numerical results for single dipoles and randomly distributed dipole arrays in microparticles for small values of the size parameter ($x < 10$) showed that the spectral and the angular distribution of fluorescence or Raman scattering might be expected to differ from those of bulk materials. The numerical nature of the procedure made it difficult to obtain results for large ($x > 20$) particles [89]. In this regard it is worth mentioning the rather different approaches taken recently by Schweiger [153] and by Videen [170]. Schweiger was motivated to find an approximate method of predicting Raman-scattered intensities from a microparticle (in the linear regime) and did this by assuming that the total scattered Raman intensity from a single particle would be proportional to the integrated internal field at the pump frequency. Videen derived expressions for the coherent light inelastically scattered from a fluorescent cylinder by integrating the induced polarization analytically over the cylinder.

Initial experimental results obtained for small ($x < 10$) [94] as well as somewhat larger ($x \sim 50$) [105] dye-doped latex particles showed the effects of the particle upon the angular distribution of the emitted radiation. Soon afterwards, sharp peaks were detected in the fluorescence and Raman spectra from dye-doped polystyrene microspheres and silica fibers in the size range $x = 20 - 100$, and these peaks were

recognized as corresponding to the natural resonant modes of the microparticle, the same modes as had been previously observed in the elastic scattering [17, 26, 79, 127, 131]. This discovery also led to a more thorough investigation of the properties of the resonance spectrum of microparticles. It was shown that fluorescence or Raman scattering at narrow resonance frequencies is more strongly enhanced than that at broader resonances. The homogeneously broadened fluorescence from e.g. a dye-coated silica fiber [128] or the broad Raman spectrum from an illuminated microsphere [164] spans several resonance frequencies, resulting in corresponding peaks in the fluorescence or Raman spectral profile. However, a monochromatic exciting beam may or may not be tuned to a resonant frequency. An input resonance would lead to enhanced internal fields in the particle at the pump frequency, and a greater excitation efficiency for the fluorescence. Such double-resonance fluorescence was observed from dye-coated fibers by Owen *et al.* [128] and in optically levitated microdroplets by Schweiger [153, 152] and was shown to be predicted by the model of Chew *et al.* [35].

More recently, the spectral peaks in the light spontaneously emitted from molecules embedded in microparticles have been the subject of further study due to new interest in the development of microlasers and the study of cavity quantum electrodynamic (QED) effects [21, 85, 173]. Chew computed the transition rates for atoms in spherical dielectric particles classically [29] and showed that enhancement of the transition rates (up to 1500 times the free-space value) is possible under certain conditions. Lai, Leung and Young [98] and Ching, Lai and Young [37] investigated such resonance effects by considering the modes of the 'universe' which can be treated as Hermitian, in contrast to the leaky modes of the cavity; they showed that Fermi's golden rule is inadequate under certain conditions, and predicted the largest QED enhancements of the decay rates for intermediate values of Q. They have also investigated the thermal spectrum and density of states [36] and indicated their importance in a microparticle cavity. Lin *et al.* [114] have made a direct observation of lifetime modification of spontaneous transitions in chelated europium ions in 10μm diameter droplets. They showed explicitly that emission corresponding to cavity resonances proceeded more quickly, and off-resonant emission more slowly, than in free space.

These modifications correspond to the altered density of final states in the cavity at resonance and non-resonance frequencies.

2.4 Nonlinear optics in microparticles and the whispering-gallery-mode laser.

In the past decade a variety of optical processes have been observed in liquid microdroplets. Of these, the observation and subsequent careful investigation of laser emission from dye-doped droplets is of particular relevance to this thesis. However the richness of the nonlinear optical processes in microparticles is such that it is inappropriate to consider a single effect in isolation. In particular, much of the research into stimulated Raman scattering from microdroplets has implications for the study of whispering-gallery mode microlasers: indeed, understanding of some aspects of these two processes has developed together. Consequently, we shall pay special attention to those papers dealing with these subjects. Thereafter, we shall briefly mention some of the other nonlinear optical processes which have been observed in microparticles.

The years 1984–1986 saw the publication of observations of nonlinear optical processes and laser emission from microdroplets. The first of these was the continuous-wave laser emission observed by R. K. Chang and colleagues at Yale University from dye-doped liquid droplets in the $a = 20 - 40\mu$m range falling freely in air and illuminated with an argon-ion laser [168]. Emissions from a stream of monodisperse droplets produced by a vibrating-orifice aerosol generator were found to exhibit a nonlinear response to pump power, which was interpreted as being evidence of laser action. The spectral profile of the emissions was found to contain sharp peaks, which for certain spectral regions were much stronger than the continuum fluorescence. The existence of these sharp peaks superimposed on a broadband fluorescence background was attributed to the high Q-value of the droplet cavity at morphology-dependent resonances, which had the effect of lowering the threshold for laser action at resonant wavelengths. It was noted that the spectral characteristics of the emissions were different in different wavelength regions, and this was attributed to the

different wavelength dependences of the absorption and gain of the Rhodamine 6G laser dye used in the experiments. The emissions were compared to those observed in the early 1960's from spherical samples of CaF_2:Sm^{++} [69]; these had been attributed to the optical analogue of the acoustic whispering-gallery modes.

The publication of Chang's work was quickly followed by reports of the study of dye-doped microdroplets illuminated with pulsed, frequency-doubled Nd:YAG laser beams. By photographing droplets using the internally-generated pulsed laser light, Qian and co-workers [143] showed that whispering-gallery-mode laser emission can occur for even substantially deformed liquid droplets. Work on a similar system by Lin *et al.* [117] showed that both TE and TM modes may be simultaneously observed above threshold under certain conditions. They also noted that laser modes tended to be observed in one or several clusters of ~ 6 modes; this was later shown [112] to be due to the excitation of more than one order of resonance.

Simultaneously, the Yale group observed other nonlinear optical processes in microdroplets. Interesting features were observed in the SRS signal from water, ethanol, CS_2 and CCl_4 droplets [157, 140, 141]. In general, the pump intensity required to initiate SRS in these droplets was substantially below that required for the bulk material. This was attributed to the focussing of the incident beam by the illuminated surface of the droplet, and to the fact that the droplet acts as a high-Q cavity at resonant frequencies. (More recently it has been realized that the difference in the density of available photon states at resonant and non-resonant frequencies may play a role in reducing the threshold under certain conditions: this is the cavity QED effect mentioned previously [37]). SRS was found to occur at resonant frequencies – as a result the SRS signal from a liquid droplet was found to consist of one or more peaks corresponding to high-Q MDRs which fall under the Raman gain profile of the medium. Broad Raman linewidths such as that of water may span many MDRs, and result in several peaks in the Raman signal. It should be emphasized that these peaks do not correspond to discrete transitions in the particulate medium; rather they are the result of the modulation of the Raman gain profile by the sharply varying Q of the droplet cavity. Consequently, the positions of such peaks in the SRS signal contain information about the droplet size.

The SRS signal from CCl_4 droplets exhibited multiorder SRS up to the fourteenth order for the ν_1 line (the totally symmetric mode at 459 cm^{-1}) when pumped with a frequency-doubled Nd:YAG laser [141]. The resultant spectrum showed Stokes peaks shifted by ν_1, $2\nu_1$,... up to $14\nu_1$, resulting from successive first-order SRS processes in which the $(n+1)$th wave is pumped by the SRS at the nth frequency shift; weaker ν_2 and ν_4 lines were also visible in the spectrum, and various multiorder combination lines were also visible. Thus, combination lines may appear after being succesively shifted through, e.g., ν_1 and ν_4. In contrast, the SRS signal from bulk CCl_4 displayed only up to $n = 2$ SRS, and the second Stokes intensity was $\sim 50\times$ weaker than the first. Again, these features were explained in terms of resonant feedback into the droplet microcavity. Assuming that all the observed Stokes lines correspond to droplet resonances, the nth-order circulating Stokes wave at frequency $\nu_{pump} - n\nu_1$ would result in a much larger internal field strength, and have a longer lifetime, than in the bulk liquid, allowing the subsequent-order SRS to build up at frequency $\nu_{pump} - (n+1)\nu_1$. Given the narrow Raman linewidth of CCl_4 ($\sim 10cm^{-1}$), a high density of MDRs is required to ensure that there is always sufficient feedback to pump subsequent-order processes: this issue was addressed by Hill and Benner [78], who found that the density of modes is at least as large as that required, for moderate values of the size parameter ($x \geq 100$).

Chen *et al.* [27] have reported the observation of fine structure in the angular distribution of SRS from single ethanol droplets. The resonant fields inside spherical droplets have n peaks between 0 and 180 degrees; if the SRS process is coherent, and if a single MDR is contributing to the SRS, this angular dependence should be visible in the transmitted light. Previous studies [133] of the angular dependence of SRS from microdroplets observed no fine structure, apparently due to several MDRs of different n contributing to the SRS, or to simultaneous observation of several orders of SRS, each supported by different MDRs. The observed angular fine structure can be used to identify the n of the MDR participating in the SRS by measuring the angular spacing of peaks in the external field. Such mode assignments were also achieved using an independent method by the research group headed by A. J. Campillo [110]. Their identification of the modes supporting non-

linear optical processes is based upon identifying modes simultaneously observed in the elastic scattering spectrum [63]. This is easier than identifying modes directly in the nonlinear optical spectrum, as the elastic-scattering modal widths are exactly calculable using the Mie theory. Elastic-scattering spectra were recorded by illuminating a droplet stream with a helium-neon laser and ramping the driving frequency of the aerosol generator, resulting in a controlled sweep of droplet size. Identification of modal features in the observed elastic scattering spectrum then provides a fiducial spectrum; other optical data acquired at specific points in the ramp cycle are thus easily analysed. Campillo's group have used this technique to analyse SRS, fluorescence and laser spectra from microdroplets [110, 115, 113, 62]. In the case of SRS, they found that the dominant peaks in the nonlinear spectrum were likely to be due to narrower modes (higher Q-values) than those dominating the corresponding elastic-scattering spectrum (which have Q-values $\sim 10^3 - 10^4$). Their method of performing mode assignments in inelastic scattering processes based upon a continuous wave elastic scattering spectrum assumes the absence of significant mode-pulling [111] by the SRS gain profile, or by the dye gain profile in the case of laser emission.

Another interesting aspect of their analysis is the importance of output coupling: in many cases, the effective Q of a particular mode will be limited by some physical property of the liquid droplet, e.g. absorption or surface roughness. Hill and Benner [78] suggested writing the effective Q as

$$\frac{1}{Q} = \frac{1}{Q_{ext}} + \frac{1}{Q_{abs}} \tag{2.2}$$

where Q_{abs} is the Q-value due to the particle medium, which may be expressed in terms of the absorption coefficient α as $Q_{abs} = 2\pi m/\lambda\alpha$ [115], and Q_{ext} is the external cavity Q representing the coupling to the external field. Seeing that the narrow resonances have very high theoretical Q_{ext} for large droplets ($Q_{ext} > 10^{20}$)[78] and all liquids have some absorption (e.g. $Q_{abs} \sim 10^8$ for ethanol) [115], the effective Q of narrow modes in droplets will be governed by absorption in the absence of any other deviation from ideal behaviour. Hence resonant emission at a narrow mode with $Q_{ext} >> Q_{abs}$ will be only weakly coupled to the external field, with coupling efficiency Q/Q_{ext}. Light trapped in such a mode will be absorbed far faster than

it will leak from the droplet. The situation is analogous to the theory of output coupling in conventional CW lasers [172, 156].

These two features of SRS spectra in microdroplets, viz. the appearance of narrower modes in the spectrum than those dominating the elastic scattering spectrum, and the importance of output coupling, are crucial for understanding laser spectra from dye-doped droplets. Some experimental evidence of this is to be found in the 1989/1990 papers by Biswas et al [18, 102]; the definitive work followed the 1992 mode identifications of Eversole *et al.* [62]. The absorption and fluorescence bands of Rh6G overlap to a certain degree, the absorption in the gain region decreasing towards longer wavelengths. In this case, the absorption of the dye is likely to be more significant than that of the solvent, if this is transparent. Hence the value for Q_{abs} in equation 2.2 will be dominated by the absorption of the dye and will increase toward longer wavelengths. As a result, narrow resonances may have $Q_{abs} << Q_{ext}$ on the shorter wavelength side of the spectrum and hence be only weakly coupled to the transmitted field. Thus one observes intrinsically higher-Q modes at longer wavelengths. Indeed, the shortest wavelength at which a given mode order (which appears spectrally as a series of almost-evenly spaced peaks) is observed in an experimental spectrum may be used to determine an approximate Q_{ext} for the mode order, by using knowledge of the bulk absorption of the dye solution, and assuming that modes disappear from the laser spectrum when Q/Q_{ext} decreases significantly below unity. These effects have been carefully studied in the fluorescent and laser emission from dye-doped droplets: the coupling efficiency has been decreased by decreasing Q_{abs} by the addition of small quantities of absorbing dye to the particle [47] and has been increased, for narrow modes, by decreasing Q_{ext} [8, 116]. This has been done by including small ($a < 1\mu$m) scattering centres (latex spheres) in the liquid droplets. These serve as Rayleigh scatter centres, scattering internally circulating light out of the droplet and thus artificially decreasing the Q_{ext} of narrow modes.

Spatial hole-burning has been investigated as a probable reason for the observation of many modes above threshold in a droplet laser [112]. Dye lasers are usually considered to be homogeneously broadened on a nanosecond time scale; consequently

one might naively expect to observe only a single mode above threshold. The mode reaching laser threshold first would grow fastest, saturating the gain, and could be expected to drive competing modes below threshold. However, due to the different field patterns of different modes, several modes with different n, l values can simultaneously exist above threshold, each having access to an independent gain source at some point in the droplet. This is because the field pattern of any given mode has a number of points at which the field is effectively zero; at such points, the gain of the medium is unaffected by the saturation due to the mode in question. Hence unsaturated regions remain at certain points within the droplet, and this gain is available for different modes, which have zeros in different places. This explanation is very close to that of spatial hole-burning in conventional Fabry-Perot cavities [156] and explains the observation of several modes of differing n (different angular distributions) for a single order, and of several orders l (differing radial distributions), above threshold. Typically, 3 or 4 orders of resonance, and 4-6 modes of each order, have been reported above threshold in microdroplets [112].

Some confusion exists in the literature over the output-versus-input intensity behaviour of dye-doped microdroplets, particularly for continuous-wave excitation. H.-B. Lin *et al.* have reported a threshold pump intensity of 10^4 W/cm^2 for 10^{-4}M Rh6G water droplets in the size range a = 20-30μm in the case of 20-nanosecond Q-switched pulses from a frequency-doubled Nd:YAG laser [117]. For continuous-wave (argon-ion laser) excitation of liquid droplets Tzeng and colleagues [168] have demonstrated threshold behaviour at a pump irradiance of 35W/cm^2 by studying the ratio of spectrally integrated emissions from the laser and fluorescent spectral regions from 10^{-3}-10^{-4}M Rh6G droplets, while Campillo and co-workers [23] have presented spectra showing a non-linear response to excitation intensity in a = 7.36μm droplets. On the other hand, K.-H. Lin and W.-F. Hsieh [118] have reported the lack of observable threshold behaviour in the integrated emissions from Rh6G methanol droplets of similar size excited with an argon-ion laser, and attributed this to the enhancement and inhibition of spontaneous emission in a microdroplet. However the apparent lack of a threshold may simply be a reflection of the very low pump intensity required to reach threshold - their data show only two pump intensity

readings between 0 and 250 W/cm^2. The rather different method of performing the measurements used by these workers is another possible reason for the disagreement.

The cavity QED effect described previously in relation to spontaneous emissions from excited atoms in microdroplets also has an effect on the stimulated emission cross-section. By equating stimulated gain to cavity losses in a lasing Rh6G ethanol droplet, Campillo *et al.* [23] were able to calculate a minimum Q-value for which modes should be able to reach threshold, for a given dye concentration, assuming total inversion of the dye population . However, substantially lower-Q resonances were observed above threshold experimentally, and this was interpreted as being due to the enhancement of the stimulated emission cross-sections of the excited dye molecules at resonant wavelengths, as predicted by theory [37].

Several other stimulated scattering and nonlinear-optical processes have been observed in microparticles. The most important of these are mentioned here, with brief comments where neccessary.

Stimulated Raman scattering and lasing have been observed in micrometer-sized cylindrical liquid jets, displaying many features similar to those observed in spherical liquid droplets [134]. The laser characteristics of coated spheres have been investigated by illuminating a suspended glass sphere coated with an evaporating dye-doped solvent with a pulsed Nd:YAG laser [60]. The resulting effects were difficult to analyse quantitatively because of the effects of heating and bleaching of the dye by the laser light, because of the lack of knowledge about the precise location of the solid core within the droplet, because of the constantly increasing dye concentration as the solvent layer evaporated and because of the difficulty of assigning observed peaks to specific resonant modes. Certainly, however, in the extremes of thin and thick liquid shells laser emission was observed from both modes which did and those which did not penetrate the glass core. Whispering-gallery-mode laser emission has also been observed from dye-doped polystyrene microspheres [95], as well as from optically and electrically pumped semiconductor 'thumbtack' or microdisk lasers [108, 123]. Two-photon pumped lasing was reported from highly concentrated Coumarin and Rhodamine solutions in liquid droplet form [96]. Electrostrictive shape distortion by cw argon-ion laser irradiation and by 400ns pulsed irradiation [166, 175] were

studied using a framing camera and by observing their effect upon the fluorescence resonance spectrum. Non-linear elastic scattering of a train of mode-locked picosecond pulses from an Nd:YAG laser by a liquid droplet [82] was initially attributed to electrostrictive acoustic-mode excitation of the droplet although this was later shown to be too small an effect to account for the observations [97], which may be due to stimulated Brillouin scattering or to the presence of nanometer-sized gas bubbles in the droplets. Coherent Raman mixing, coherent anti-Stokes Raman scattering [142] and stimulated anti-Stokes Raman scattering [104] have been observed in droplets illuminated with one or more laser beams. Competition between stimulated Brillouin scattering (SBS) and SRS has been studied in liquid droplets using a single-mode and a multimode Nd:YAG laser beam [176]: using a pump beam which was tightly focussed onto the centre of an ethanol droplet to avoid the pump being coupled to a droplet resonance, it was found that for single-mode excitation, the observed SRS is pumped by an internally-generated SBS wave. This is partly because the SBS is an MDR-enhanced process; it thus has an appropriate distribution around the droplet rim to efficiently amplify Raman scattering at a resonant wavelength. Third harmonic generation and third-order sum-frequency generation observed [3] in microdroplets have led to a re-examination of phase velocities of MDR's and their implications for phase-matching requirements in droplets [103]. Somewhat more information about these processes and further references are in the 1990 and 1992 review articles by Chang [24, 25].

2.5 Applications of optical whispering-gallery modes

We shall now briefly describe some applications of morphology-dependent resonances and of nonlinear optics in microparticles. Most of these relate to particle characterization: light scattering has long been studied for its usefulness in conveying information about the size of the scatterers. However, ultra-high resolution size measurements and the possibility of chemical characterization by the nonlinear Raman method are truly novel features of particle characterization using MDRs [15, 58, 107]. The possibility of using the narrow resonance structure in the elastic scattering from

microdroplets to characterize the particles was realized virtually as soon as this was experimentally observed. The method was soon applied to droplets in optical levitation experiments [49], to unclad optical fibers [129] and to fluorescence spectra from individual dye-doped polystyrene spheres [51, 80]. The spectral observation of MDRs was also used to deduce the taper of the outer diameter of fine fibers [14], as well as to study evaporation and condensation rates [167] and laser-induced shape distortions [166] of dye-doped liquid droplets flowing in a stream. An interesting variation based on the different wavelength shifts of the TE and TM modes in a coated sphere as the coating thickness changes was used by Folan [64] to investigate absorption of water vapour by polystyrene microparticles.

Absolute size measurements were performed by assigning observed peaks to specific resonant modes calculated using the appropriate boundary-value solution. Various methods of assignment were used, from visually fitting observed and computed elastic-scattering spectra [49] to fully automated computer routines suitable for fluorescent or Raman spectra [80]. Some of these fits were performed using the refractive index as well as the size of the particle as a free parameter [49], in others the refractive index was assumed to be accurately known as a function of wavelength [51], or was determined independently using the angular scattering pattern at a given wavelength [129]. In most cases, the average size of the cylinder or sphere was measured to an accuracy of a few parts in 10^5. While some fits were performed to more than one order of resonance, nonetheless the mode assignment procedure becomes more difficult, and the resultant size estimates less certain, for increasing particle size, as the density of theoretically available modes increases. This is particularly true for inelastic scattering spectra, where observed peaks may be due to modes which are intrinsically extremely narrow ($Q \sim 10^8$) compared to those normally observed in elastic-scattering spectra. The exact mechanism determining the effective Q of the narrowest available modes, and thus those modes which will dominate nonlinear processes, has been the subject of some study [99]; without prior knowledge of a specific experimental situation it may be impossible to estimate which modes are most likely to be contributing to observed nonlinear processes. In such cases, some idea of the particle size may nonetheless be easily gained from the spacing of the

observed modes by using the Chýlek formula (equation 2.1) to estimate the mode spacing. The estimated size $a = \lambda^2 \Delta x / 2\pi \Delta\lambda$ then follows from the definition of the size parameter, to an accuracy of a few percent. This method can be used following observation of only a few resonant modes in e.g. SRS spectra from water or fuel droplets. Golombok and Pye [72] have extended this method by using spectral analysis to determine the characteristic mode spacings in a spectrum recorded from several simultaneously-illuminated droplets in e.g. a fuel spray.

Such SRS spectra may be simultaneously analysed to give information about the chemical species concentrations in the scatterer. A similar technique may be applied using spontaneous Raman scattering [137, 151, 163]; however, due to the small sample volume at least several seconds of integration time is required to obtain a respectable signal-to-noise ratio from a single particle or droplet. In contrast, an SRS spectrum from a single liquid droplet may be obtained using a single 15ns pump pulse. Serpengüzel *et al.* [154] have shown that it is possible to gain molecular concentration information by studying the ratio of SRS signals of salts dissolved in water; results are expected to be reliable while the SRS gain is unsaturated.

Applications to fuel sprays have been investigated by Acker, Serpengüzel and co-workers, and by Golombok and Pye. Serpengüzel *et al.* [155] used fluorescence, lasing and SRS from droplets to image a two-dimensional cross-section of a fuel spray. The wavelength shifts of these processes is used to distinguish different constituents of the spray. In particular, good discrimination is achieved between the liquid and vapour phases. Acker *et al.* [4] dealt with more quantitative issues in a similar system, investigating the cavity Q value and density of modes in liquid droplets under the extreme conditions found in internal combustion engines, and the relative SRS signals from fuel mixtures. Both of the above sets of researchers find that SRS is emitted primarily from the larger droplets in a polydisperse spray. Concentration measurements of fuel mixtures in injected fuel sprays were also the subject of a study by Golombok and Pye [71, 73]. They suggested an internal referencing system for SRS signals from a fuel spray, based upon the observation of multimode SRS spectra in droplets. They thereby deduced differential evaporation in a two-component spray injected into ambient air, under different pressures.

Further potential applications of MDRs in microdroplets are their use to form the basis for a spectral hole-burning memory and the use of microdisk lasers in integrated optoelectronic devices. Microparticle-based spectral hole-burning has been demonstrated [9] in a collection of dye-doped polystyrene spheres of random sizes. A medium formed by such a collection will have a white fluorescent spectrum due to the large number of available resonances in particles of different sizes. Illuminating the sample with a bright and spectrally narrow light source will cause enhanced resonant fields in those particles which resonate at the illuminating frequency, and these fields can be sufficiently strong to bleach the dye molecules in those particles. Subsequent excitation of the broadband fluorescence of the medium reveals a spectral hole in the integrated fluorescence from the collection of particles; those particles bleached due to their being resonant with the bright monochromatic source no longer contribute to the fluorescence. This effect may have application in the development of a superdense data storage medium [65].

The microdisk semiconductor whispering-gallery-mode lasers being developed by McCall and colleagues [108, 123] at AT&T Bell Laboratories are perceived as being possible competitors to vertical-cavity surface-emitting lasers for use in integrated optoelectronic devices [109]. These small (diameter several microns) devices can lase in the 'silica window' region, $\lambda = 1.3 - 1.6\mu$m, when electrically or optically pumped. The InGaAsP lasers were grown by metallo-organic vapour phase epitaxy. Light propagating around the disk's perimeter in whispering-gallery modes leaks slowly out in the plane of the disk. The lasers can be made so as to lase in a single mode.

Chapter 3

Electromagnetic scattering from a normally-illuminated layered dielectric fiber

3.1 Introduction

This chapter deals with some of the features of high-frequency electromagnetic scattering from a normally-illuminated dielectric fiber comprising two concentric circular cylinders of differing refractive index. The first section is concerned with the derivation of the requisite equations by expansion of the incident, internal and scattered fields in terms of Bessel functions and by the use of Maxwell's equations to apply the appropriate boundary conditions at the refractive index discontinuities. The next section describes the incorporation of the derived solutions into FORTRAN routines to compute the scattering characteristics of the fiber. Routines to compute numerical values for the internal and nearby external electromagnetic fields have been developed, and results from these programs are presented in the third part of the chapter. Several features of the scattering characteristics are investigated and compared with known results from the simpler case of the homogeneous cylinder. Numerical results presented have largely been chosen to illustrate those features of the electromagnetic scattering process which are significant for the experiments to

be described later in this thesis.

3.2 Theory

In this section we present the solution to the scattering of a plane-polarized electromagnetic wave incident normally upon a dielectric concentric cylinder [88, 162]. The solution derived here is for a fiber consisting of a homogeneous, circular core covered by a concentric, circular cladding of different refractive index. However, as pointed out by Kerker [88], the solution may easily be extended to any number of discrete layers on the fiber. The fiber has outer radius b and inner radius a, and the corresponding refractive indexes m_1 and m_2, while the refractive index of the continuous medium is assumed to be that of free space. The fiber axis lies on the z-axis of the coordinate system, and the incident wave travels along the $\phi = 0$ axis. The two orthogonal polarization states of the electromagnetic field of the incident wave are:

1. the electric vector is parallel to the cylinder axis (transverse magnetic or TM case, $\underline{E} = E_z\hat{z}$), and
2. the electric vector is perpendicular to the cylinder axis (TE case).

The two cases are treated separately below.

3.2.1 Electric vector parallel to cylinder axis

The expansion of the incident plane wave polarized in the $\hat{z}$ direction and travelling along the $\phi = 0$ axis is given in terms of the Bessel function [1] in the cylindrical coordinate system by [19]

$$\underline{E}_{inc} = \hat{z}E_0 \sum_{n=-\infty}^{\infty} i^n J_n(k\rho) \exp\left[i(n\phi - \omega t)\right] \tag{3.1}$$

while the wave scattered from the normally-illuminated cladded dielectric cylinder centred on the $\hat{z}$-axis may be expressed as

$$\underline{E}_{scatt} = \hat{z}E_0 \sum_{n=-\infty}^{\infty} i^n(-b_n^{ext}) H_n^{(1)}(k\rho) \exp\left[i(n\phi - \omega t)\right] \tag{3.2}$$

where the Hankel function $H_n^{(1)} = J_n + iY_n$ has been chosen for its asymptotic behaviour [1] which, when coupled with the assumed time-dependence, represents an outgoing cylindrical wave at large distances from the normally– illuminated fiber. The coefficient b_n^{ext} remains to be determined by the boundary conditions. The field outside the fiber is given by the sum of the incident and the scattered waves,

$$\underline{E}_{ext} = \underline{E}_{inc} + \underline{E}_{scatt} \tag{3.3}$$

The electric field inside the fiber cladding ($a < \rho < b$) may be written

$$\underline{E}_1 = \hat{z}E_0 \sum_{n=-\infty}^{\infty} i^n \left[b_n^{out1} J_n(m_1 k\rho) + b_n^{out2} H_n^{(1)}(m_1 k\rho)\right] \exp\left[i(n\phi - \omega t)\right] \tag{3.4}$$

and the field for $\rho < a$ in the fiber core is

$$\underline{E}_2 = \hat{z}E_0 \sum_{n=-\infty}^{\infty} i^n b_n^{in} J_n(m_2 k\rho) \exp\left[i(n\phi - \omega t)\right] \tag{3.5}$$

where b_n^{in}, b_n^{out1} and b_n^{out2} are additional coefficients to be determined from the boundary conditions. Only the function J_n is used in equation 3.5 as it alone of the Bessel functions is regular at the origin.

The fact that $\underline{E} = \hat{z}E_z$ for the incident wave implies that this is so for the internal and scattered waves as well. In this case there is only a tangential component to the electric fields, which must therefore be continuous at the boundaries $\rho = a$ and $\rho = b$. This yields the following pair of equations:

$$J_n(kb) - b_n^{ext} H_n^{(1)}(kb) = b_n^{out1} J_n(m_1 kb) + b_n^{out2} H_n^{(1)}(m_1 kb) \tag{3.6}$$

$$b_n^{in} J_n(m_2 ka) = b_n^{out1} J_n(m_1 ka) + b_n^{out2} H_n^{(1)}(m_1 ka) \tag{3.7}$$

Now, Maxwell's equations for periodic fields give us

$$\nabla \times \underline{E} = ik\underline{H}$$

We are interested in the tangential component of $\underline{H}$

$$\underline{H}_{tang} = H_\phi = \frac{i}{\mu\omega} \frac{dE_z}{d\rho}$$

which yields

$$H_\phi^{inc} = \frac{E_0}{\mu_0 \omega} \sum_{n=-\infty}^{\infty} i^{n+1} k J_n'(k\rho) \exp\left[i(n\phi - \omega t)\right] \tag{3.8}$$

and

$$H_\phi^{scatt} = \frac{E_0}{\mu_0 \omega} \sum_{n=-\infty}^{\infty} i^{n+1} k(-b_n^{ext}) H_n^{(1)'}(k\rho) \exp\left[i(n\phi - \omega t)\right] \tag{3.9}$$

for the external magnetic fields. The fields inside the fiber are

$$H_{\phi 2} = \frac{E_0}{\mu_2 \omega} \sum_{n=-\infty}^{\infty} i^{n+1} k m_2 b_n^{in} J_n'(m_2 k\rho) \exp\left[i(n\phi - \omega t)\right] \tag{3.10}$$

for the core region, and

$$H_{\phi 1} = \frac{E_0}{\mu_1 \omega} \sum_{n=-\infty}^{\infty} i^{n+1} m_1 k \left[b_n^{out1} J_n'(m_1 k\rho) + b_n^{out2} H_n^{(1)'}(m_1 k\rho)\right] \exp\left[i(n\phi - \omega t)\right] \tag{3.11}$$

for the cladding of the fiber. Matching the H_{tang} at the boundaries now yields

$$J_n'(kb) - b_n^{ext} H_n^{(1)'}(kb) = m_1 \left(b_n^{out1} J_n'(m_1 kb) + b_n^{out2} H_n^{(1)'}(m_1 kb)\right) \tag{3.12}$$

$$m_2 b_n^{in} J_n'(m_2 ka) = m_1 \left(b_n^{out1} J_n'(m_1 ka) + b_n^{out2} H_n^{(1)'}(m_1 ka)\right) \tag{3.13}$$

where we have assumed that $\mu_2 = \mu_1 = \mu$.

Defining $x_1 = kb$ and $x_2 = ka$, equations 5-6 and 11-12 may be expressed as the matrix equation

$$\begin{pmatrix} H_n^{(1)}(x_1) & J_n(m_1 x_1) & H_n^{(1)}(m_1 x_1) & 0 \\ H_n^{(1)'}(x_1) & m_1 J_n'(m_1 x_1) & m_1 H_n^{(1)'}(m_1 x_1) & 0 \\ 0 & J_n(m_1 x_2) & H_n^{(1)}(m_1 x_2) & -J_n(m_2 x_2) \\ 0 & m_1 J_n'(m_1 x_2) & m_1 H_n^{(1)'}(m_1 x_2) & -m_2 J_n'(m_2 x_2) \end{pmatrix} \begin{pmatrix} b_n^{ext} \\ b_n^{out1} \\ b_n^{out2} \\ b_n^{in} \end{pmatrix} = \begin{pmatrix} J_n(x_1) \\ J_n'(x_1) \\ 0 \\ 0 \end{pmatrix} \tag{3.14}$$

which can be solved for the external and internal field coefficients by the application of Kramer's rule. This completes the solution of the scattering problem, as we now have expressions for the electric fields at all points in space. It is worth noting that this result is easily extended to an n-layered cylinder [87].

3.2.2 Magnetic vector parallel to cylinder axis

In this case the electric vectors have both radial and azimuthal components. The incident wave with polarization perpendicular to the fiber axis may be expanded as

$$\underline{E}_{inc} = E_0 \sum_{n=-\infty}^{\infty} i^n \left[\frac{nJ_n(k\rho)}{k\rho}\hat{\rho} + iJ_n'(k\rho)\hat{\phi}\right] \exp[i(n\phi - \omega t)] \tag{3.15}$$

and this sets the form for the internal and scattered fields as well. The expressions for these are

$$\underline{E}_{scatt} = E_0 \sum_{n=-\infty}^{\infty} i^n(-a_n^{ext}) \left[\frac{n}{k\rho}H_n^{(1)}(k\rho)\hat{\rho} + iH_n^{(1)'}(k\rho)\hat{\phi}\right] \exp[i(n\phi - \omega t)] \tag{3.16}$$

$$\begin{aligned}\underline{E}_1 \;=\; & E_0 \sum_{n=-\infty}^{\infty} i^n \left(\frac{n}{m_1 k\rho}\left[a_n^{out1}J_n(m_1k\rho) + a_n^{out2}H_n^{(1)}(m_1k\rho)\right]\hat{\rho}\right. \\ & \left. + i\left[a_n^{out1}J_n'(m_1k\rho) + a_n^{out2}H_n^{(1)'}(m_1k\rho)\right]\hat{\phi}\right) \exp[i(n\phi - \omega t)]\end{aligned} \tag{3.17}$$

$$\underline{E}_2 = E_0 \sum_{n=-\infty}^{\infty} i^n a_n^{in} \left(\frac{n}{m_2 k\rho}J_n(m_2k\rho)\hat{\rho} + iJ_n'(m_2k\rho)\hat{\phi}\right) \exp[i(n\phi - \omega t)] \tag{3.18}$$

where a_n^{ext}, a_n^{out1}, a_n^{out2} and a_n^{int} are the coefficients which are to be determined. By using the definition of the magnetic field

$$\underline{H} = \frac{-i}{\mu\omega}\nabla \times \underline{E} \tag{3.19}$$

and the fact that the Bessel functions $Z_n(\rho)$ are the solutions to Bessel's equation

$$\rho\frac{d}{d\rho}\left(\rho\frac{d}{d\rho}Z_n\right) + (\rho^2 - n^2)Z_n = 0$$

one may obtain the following expressions for the magnetic fields:

$$\underline{H}_{inc} = -\frac{k}{\mu_0\omega}\hat{z} \sum_{n=-\infty}^{\infty} E_0 i^n J_n(k\rho) \exp[i(n\phi - \omega t] \tag{3.20}$$

$$\underline{H}_{scatt} = +\frac{k}{\mu_0\omega}\hat{z} \sum_{n=-\infty}^{\infty} E_0 i^n a_n^{ext} H_n^{(1)}(k\rho) \exp[i(n\phi - \omega t)] \tag{3.21}$$

$$\underline{H}_1 = -\frac{k}{\mu_1\omega}\hat{z}\sum_{n=-\infty}^{\infty} E_0 i^n m_1 \left[a_n^{out1} J_n(m_1 k\rho) + a_n^{out2} H_n^{(1)}(m_1 k\rho)\right] \exp[i(n\phi - \omega t)] \tag{3.22}$$

and

$$\underline{H}_2 = -\frac{k}{\mu_2\omega}\hat{z}\sum_{n=-\infty}^{\infty} E_0 i^n a_n^{in} m_2 J_n(m_2 k\rho) \exp[i(n\phi - \omega t)] \tag{3.23}$$

Again, defining $x_1 = kb$, $x_2 = ka$ and equating the tangential components of $\underline{E}$ and $\underline{H}$ at the cylinder boundaries one arrives at the matrix equation

$$\begin{pmatrix} H_n^{(1)}(x_1) & m_1 J_n(m_1 x_1) & m_1 H_n^{(1)}(m_1 x_1) & 0 \\ H_n^{(1)\prime}(x_1) & J_n'(m_1 x_1) & H_n^{(1)\prime}(m_1 x_1) & 0 \\ 0 & J_n'(m_1 x_2) & H_n^{(1)\prime}(m_1 x_2) & -J_n'(m_2 x_2) \\ 0 & m_1 J_n(m_1 x_2) & m_1 H_n^{(1)}(m_1 x_2) & -m_2 J_n(m_2 x_2) \end{pmatrix} \begin{pmatrix} a_n^{ext} \\ a_n^{out1} \\ a_n^{out2} \\ a_n^{in} \end{pmatrix} = \begin{pmatrix} J_n(x_1) \\ J_n'(x_1) \\ 0 \\ 0 \end{pmatrix} \tag{3.24}$$

which again may be solved by the use of Kramer's rule.

Expressions for the far-field scattering characteristics, i.e. the angular scattering pattern and the efficiencies of the cylinder for extinction, scattering and absorption are easily derived by the use of the asymptotic approximations to the Bessel functions for large argument once the scattering coefficients have been computed [169]. Evaluating the scattered electric fields equations 3.2 and 3.16 in the asymptotic limit of

$$H_n^{(1)}(z) \to \sqrt{\frac{2}{\pi z}} \exp i(z - \frac{n\pi}{2} - \frac{\pi}{4})$$

gives

$$\underline{E}_{scatt} \to \hat{z} E_0 \sqrt{\frac{2}{\pi k\rho}} \exp[i(k\rho - \frac{\pi}{4})] \left[b_0^{ext} + 2\sum_{n=1}^{\infty} b_n^{ext} \cos n\phi\right] \tag{3.25}$$

$$\underline{E}_{scatt} \to \hat{\phi} E_0 \sqrt{\frac{2}{\pi k\rho}} \exp[i(k\rho - \frac{\pi}{4})] \left[a_0^{ext} + 2\sum_{n=1}^{\infty} a_n^{ext} \cos n\phi\right] \tag{3.26}$$

It will frequently be convenient in numerical investigation of the scattering properties of the cylinder to study the extinction efficiency Q_{ext}, which is the extinction cross-section of the particle divided by its geometrical cross-section. For a non-absorbing particle, this is also equal to the scattering efficiency of the particle. The

expressions for the extinction efficiencies are given here in their most common form [169] for easy reference:

Case 1: Transverse magnetic

$$Q_{ext} = \frac{2}{x} \sum_{n=-\infty}^{\infty} Re(b_n) \tag{3.27}$$

Case 2: Transverse electric

$$Q_{ext} = \frac{2}{x} \sum_{n=-\infty}^{\infty} Re(a_n) \tag{3.28}$$

3.3 Implementation in FORTRAN routines

Modern high-speed computers have to a certain extent trivialised the numerical computation of the scattering properties of circularly-symmetric fine particles. Considerable effort has been put into developing fast, accurate and reliable scattering routines, particularly for the well-known Lorenz-Mie theory describing the scattering of a plane wave by a homogeneous dielectric sphere. At the same time, analytical investigation of the Mie scattering expressions and the modelling of some of the scattering processes in terms of geometrical and physical optics have increased the understanding of some of the numerical results which come out of 'black box' scattering programs, and these may be extended to apply to related scattering geometries such as the infinite homogeneous cylinder and the coated sphere. Nonetheless, the wide range of particle size parameters which are of interest (often up to three orders of magnitude in x) and the large number of terms needed for convergence in the scattering summations ($n \geq x$), when coupled with the limited word length on computers and the potential instability of the recurrence relations commonly used to compute the neccesary special functions, can cause uncertainty in the results of all but the most carefully-designed scattering programs [19, 171]. To our knowledge, the implementation of the above solutions for the normally-illuminated concentric-cylinder scattering problem has never been described in a practical form useful for large values of x and complex refractive indexes m. In view of this it is deemed

worthwhile describing the routines used in the present research, what limitations are placed upon their use, and what checks have been applied to the results.

The primary objectives of the routines to be described here are to compute the internal and external field coefficients resulting from the application of the boundary conditions for given values of the parameters x_1, x_2, m_2 and m_1, and then to sum these in the appropriate fashion in order to arrive at the physically meaningful quantities, which may be the far-field scattering functions and extinction efficiencies, or values for the electric or magnetic field intensities at specific points in the internal or external near-field region.

3.3.1 Convergence of the summations

It will be noted that all the necessary expressions consist of summations over the range of indexes $-\infty < n < \infty$; however, it is easily shown that contributions from terms with negative indexes are either equal to the corresponding positive-index term, or else the two are equal in magnitude but opposite in sign, cancelling. In practice, therefore, only the scattering coefficients with positive indexes need to be computed: in addition, the summations converge, and terms with $n \geq nmax$ may be neglected in the summation. The value of $nmax$ needs to be chosen carefully; it is well-known that $n \geq x$ is usually a sufficient condition for a convergent sum in the case of the homogeneous cylinder. However, some of the features of interest in the present work occur in partial waves with $x_1 < n < m_1 x_1$, and may easily be missed by an injudicious choice of $nmax$ [80]. On the other hand, the functions $J_n(\mathcal{Z})$ and $Y_n(\mathcal{Z})$ become very small and very large respectively as $n > \mathcal{Z}$, and will eventually cause overflow and underflow problems on any computer. The problem will be exacerbated if $x_2 << x_1$, particularly if m_2 is small, as the computation of $J_n(m_2 x_2)$ will then need to be carried out to $n > x_1 >> m_2 x_2$, in order to calculate the coefficients as they have been expressed. This numerical problem may be circumvented by separating the contributions to the field coefficients from the inner and outer cylinders, and neglecting contributions to the coefficients from the inner cylinder when these become much smaller than those from the outer cylinder. A similar approach was used by Bohren and Huffman in their routine for the scattering

from a coated sphere [19]. The expressions are most easily derived by expanding the determinants in the Kramer's-rule solution of equations 3.24 and 3.14 in terms of cofactors of the last row and column. (From here on we use a_n and b_n to refer to a_n^{ext} and b_n^{ext}.) The resulting expressions for the external field coefficients for the problem considered here are

$$a_n = \frac{J_n(x_1)\left[J_n'(m_1x_1) + A_nH_n^{(1)'}(m_1x_1)\right] - m_1J_n'(x_1)\left[J_n(m_1x_1) + A_nH_n^{(1)}(m_1x_1)\right]}{H_n(x_1)\left[J_n'(m_1x_1) + A_nH_n^{(1)'}(m_1x_1)\right] - m_1H_n'(x_1)\left[J_n(m_1x_1) + A_nH_n^{(1)}(m_1x_1)\right]} \tag{3.29}$$

and

$$b_n = \frac{m_1J_n(x_1)\left[J_n'(m_1x_1) + B_nH_n^{(1)'}(m_1x_1)\right] - J_n'(x_1)\left[J_n(m_1x_1) + B_nH_n^{(1)}(m_1x_1)\right]}{m_1H_n(x_1)\left[J_n'(m_1x_1) + B_nH_n^{(1)'}(m_1x_1)\right] - H_n'(x_1)\left[J_n(m_1x_1) + B_nH_n^{(1)}(m_1x_1)\right]} \tag{3.30}$$

where

$$A_n = \frac{m_2J_n'(m_1x_2)J_n(m_2x_2) - m_1J_n(m_1x_2)J_n'(m_2x_2)}{m_1H_n^{(1)}(m_1x_2)J_n'(m_2x_2) - m_2H_n^{(1)'}(m_1x_2)J_n(m_2x_2)} \tag{3.31}$$

and

$$B_n = \frac{m_2J_n(m_1x_2)J_n'(m_2x_2) - m_1J_n(m_2x_2)J_n'(m_1x_2)}{m_1H_n^{(1)'}(m_1x_2)J_n(m_2x_2) - m_2J_n'(m_2x_2)H_n^{(1)}(m_1x_2)} \tag{3.32}$$

are the contributions to the scattering coefficients from the inner cylinder, which are neglected when they become sufficiently small. Study of the expressions for the coefficients for the cladding region of the cylinder reveals that the second of these, i.e. the a_n^{out2} and b_n^{out2} associated with the term involving $H_n^{(1)}(m_1k\rho)$ converge as fast as the A_n and B_n above. The other cladding coefficient may be treated as the external field coefficients above, giving

$$a_n^{out1} = \frac{H_n^{(1)}(x_1)J_n'(x_1) - H_n^{(1)'}(x_1)J_n(x_1)}{H_n^{(1)}(x_1)\left[J_n'(m_1x_1) + A_nH_n^{(1)'}(m_1x_1)\right] - m_1H_n^{(1)'}(x_1)\left[J_n(m_1x_1) + A_nH_n^{(1)}(m_1x_1)\right]} \tag{3.33}$$

and

$$b_n^{out1} = \frac{H_n^{(1)}(x_1)J_n'(x_1) - H_n^{(1)'}(x_1)J_n(x_1)}{m_1H_n^{(1)}(x_1)\left[J_n'(m_1x_1) + B_nH_n^{(1)'}(m_1x_1)\right] - H_n^{(1)'}(x_1)\left[J_n(m_1x_1) + B_nH_n^{(1)}(m_1x_1)\right]} \tag{3.34}$$

with the A_n and B_n as defined above. The coefficients for the core region do not present a problem, as convergence for $n \geq m_2x_2$ is ensured by the factors $J_n(m_2k\rho)$ and $J_n'(m_2k\rho)$ in equations 3.18 and 3.5.

Convergence of the summations for the calculation of the far-field scattering characteristics depends upon the decrease in the scattering coefficients a_n and b_n as $n > x_1$. It is known (see Wiscombe [171]) that the value of the Bessel function $J_n(\mathcal{Z})$ is diminished and that for $Y_n(\mathcal{Z})$ increased by several orders of magnitude when

$$n > \mathcal{Z} + 4\mathcal{Z}^{0.333} + 2 \tag{3.35}$$

over a wide range of values of $\mathcal{Z}$. On the other hand, some of the high-Q resonances being investigated in this study occur in partial waves with n in the region $x < n < mx$, and resonant features of the internal and scattered fields may be missed for certain combinations of m and x if equation 3.35 is used to determine $nmax$ by putting $\mathcal{Z} = x_1$. (Equation 3.35 then does not have any dependence on m.) Therefore we have put $nmax$ equal to the largest of the numbers m_1x_1, m_2x_2 and the n resulting from the use of equation 3.35 with $\mathcal{Z} = x_1$. This convergence condition errs on the 'safe' side, i.e. convergence is assured, but dynamic range problems may be encountered in the computation of the required functions $J_n(x_1)$ and $Y_n(x_1)$, particularly if m is large. All programs were compiled so as to terminate on overflow/underflow errors.

Calculating numerical values for the electric fields within the cylinder cladding requires a different convergence criterion, as the decrease in the factor $J_n(mk\rho)$ will determine the number of terms needed to ensure convergence of the summation. Therefore the condition 3.35 is used with $\mathcal{Z} = m_1k\rho$ (in the cylinder cladding) or $\mathcal{Z} = m_2k\rho$ (for points in the cylinder core). It will be noted that the coefficients b_n^{out2} and a_n^{out2} decrease rapidly in magnitude for $n > m_2x_2 \approx m_1x_2$, which means that they will usually be down by orders of magnitude before the imaginary component of $H_n^{(1)}(m_1k\rho)$ (i.e. $iY_n(m_1k\rho)$) reaches the exponentially increasing regime, as $\rho > x_2$ in the cladding region.

Different criteria again are required for computation of the near-field patterns external to the cylinder. The external electric field is given by $\underline{E}_{ext} = \underline{E}_{inc} + \underline{E}_{scatt}$. The highest order needed in computing $\underline{E}_{scatt}$ is determined by the cylinder size and refractive index, and a similar criterion to that used in the far-field calculations

is applicable. For computation of $\underline{E}_{inc}$, however, the required value of $\mathcal{Z}$ to be substituted into equation 3.35 is $\mathcal{Z} = k\rho$, where ρ is the distance from the origin of the coordinate system. Thus an increasing number of terms is required to compute the incident field as one moves away from the scatterer.

We cannot claim that the routines developed here are foolproof or generally applicable; we have used them over a wide range of a, b values and over a smaller range of complex m_1, m_2 values. However, we have used the convergence criteria above more as guidelines than as firm rules, and have found conditions under which they are not sufficient, particularly for large fibers. Appropriate convergence criteria are easily found for isolated cases. Hence we have adopted a cautious attitude towards the results of the routines.

3.3.2 Computation of values for the Bessel functions

The primary remaining problem in computing numerical values for the given solutions is that of computing values for the necessary Bessel functions, which in the general case may have complex arguments, and which need to be computed for all positive orders up to $n = nmax$. These computations also consume the major part of the computing time for almost any application of the scattering routines. The values for the Bessel functions used in the routines described here were computed by the use of the recurrence relations for the cylindrical Bessel functions of the first and second kinds, viz.

$$C_{\nu-1}(\mathcal{Z}) + C_{\nu+1}(\mathcal{Z}) = \frac{2\nu}{\mathcal{Z}} C_\nu(\mathcal{Z}) \tag{3.36}$$

A point of concern in the repeated application of the recurrence relation (3.36) is the numerical instability of the relation for the computation of $J_n(\mathcal{Z})$ when used in the direction of increasing order, a problem which has been pointed out by many authors. The routine *Bessel.for* which is called by the scattering programs relies heavily upon that given by Bohren and Huffman [19] and due to Bohren and Timbrell. Values for $J_n(\mathcal{Z})$ are computed by the now-standard technique of downward recurrence and renormalization, apparently first proposed by Miller [1]. The downward recurrence to compute the intermediate function $F_m(\mathcal{Z})$ is initiated with the values $F_m(\mathcal{Z}) =$

0, $F_{m-1}(\mathcal{Z}) = 10^{-200}$, and $F_{m-2}(\mathcal{Z})$, $F_{m-3}(\mathcal{Z})...F_0(\mathcal{Z})$ are then computed by the repeated use of 3.36. The values of $F_n(\mathcal{Z})$ are then related to the Bessel functions $J_n(\mathcal{Z})$ for $n < m - \delta_n$ by

$$J_n(\mathcal{Z}) = F_n(\mathcal{Z})/\alpha \tag{3.37}$$

where α is a constant to be determined. The value of δ_n needs to sufficiently large that equation 3.37 is true for the maximum required order of J_n. The value for δ_n is determined by iteration; starting with $nmax + \delta_n = \mathcal{Z} + 4\mathcal{Z}^{\frac{1}{3}} + 2$ and increasing δ_n until successive values of $F_{nmax}(\mathcal{Z})$ differ by less than 1 part in 10^{12}. The iteration is necessary as there is no fixed relationship between the argument of the Bessel functions, which may be m_2x_2, m_1x_1, or x_1, and the maximum order of the Bessel functions required. The renormalization of the $J_n(\mathcal{Z})$ is performed with the aid of the relation

$$J_0(\mathcal{Z}) + 2\sum_{n=1}^{\infty} J_{2n}(\mathcal{Z}) = 1 \tag{3.38}$$

as used by Bohren and Huffman for the homogeneous cylinder. (Care is required in the use of equation 3.38 to ensure that the summation is not terminated while significant values of $J_n(\mathcal{Z})$ remain uncounted. This sometimes requires that the value of *nmax* used in the routine *Bessel.for* is somewhat greater than that finally required in the partial-wave expansion, where convergence may be determined by a Bessel function with a smaller argument.) The values for $Y_n(\mathcal{Z})$ are computed by the stable upward recurrence, the recurrence being initiated with the values Y_0 and Y_1 computed by

$$Y_0 = \frac{2}{\pi}\left[(log(\frac{\mathcal{Z}}{2} + \gamma) - 2\sum_{m=1}^{\infty}\frac{(-1)^m J_{2m}(\mathcal{Z})}{m}\right] \tag{3.39}$$

and the use of the Wronskian $Y_0(\mathcal{Z})J_1(\mathcal{Z}) - Y_1(\mathcal{Z})J_0(\mathcal{Z}) = 2/\pi\mathcal{Z}$.

3.3.3 Checks of the validity and limitations of the routines

Some effort has been put into checking the range of validity of the above routines, and the accuracy of the numerical results obtained. Results from the Bessel function routine have been compared to tabulated values [1] for a wide range of real arguments and orders. Numerical results from the far-field programs, which also constitute a

check on the computation of the scattering coefficients and a further check on the Bessel functions, have been compared to published values [61] of Q_{ext} for both polarizations for the case of an air-filled ($m_2 = 1.00$) fine ($x_1 < 6.$) fiber for several values of a/b and m_1. In all cases, there was agreement to the published number of decimal places. Furthermore, results for much larger values of the size parameter ($x \simeq 400$) have been obtained from the programs by putting $m_2 = m_1$, and the results then compared to those obtained by the use of a standard published code [19] from a normally-illuminated homogeneous, circular cylinder. In all cases, excellent agreement was obtained.

The routines for computing the internal- and near-field external functions were checked in a similar manner. Computations using $m_2 = m_1$ were compared to published results for the internal and external field distributions for a homogeneous cylinder. Specifically, figures 1, 2 and 3 in reference [130] were reproduced, as were figures 1 and 6 in reference [16]. To our knowledge, no near field or internal intensity functions have been published for the layered cylinder, even for small values of the size parameter. However, we have checked that the numerical solutions do indeed satisfy the required boundary conditions at the refractive index discontinuities for a variety of values of a/b, x_1, m_2 and m_1. Most computations have been performed for the physically interesting case of a glass capillary fiber ($m_1 = 1.458$ or 1.5, corresponding to a fused-silica or Crown glass) filled with a gaseous or liquid core ($m_2 = 1.00 - 1.7$). For parameters in the above ranges, computations can be safely performed up to values of the size parameter $x_1 \simeq 700$, corresponding to a fiber of radius $a \simeq 65\mu m$ illuminated with orange light. For $x_1 = 700$, well over a thousand terms are included in the summations and computations are exceedingly slow. For $x_1 > 700$, we encountered dynamic-range problems using double-precision (Real*8, Complex*16) arithmetic on the UCT VAX 6230 where these computations were performed. A more restrictive condition may need to be applied to the computation of the external near-fields, as these require the computation of Bessel functions at distances from the origin implying arguments $> x_1$. Dynamic-range problems such as those described could probably be overcome by more careful attention to convergence criteria.

3.4 Some numerical results

In this section we present some numerical results which demonstrate some of the features of the scattering from the layered fiber. We investigate first the far-field extinction efficiency, which illustrates some of the general features of the scattering for a range of values of the size parameter. After explaining these general features, some internal and near- external field patterns are investigated at specific frequencies corresponding to cases relevant to our experiments. We shall pay particular attention to the nature of morphology-dependent resonances in the cladded-fiber geometry, as these are relevant to the whispering-gallery-mode laser to be described later in this thesis. Although our computer programmes define the refractive index as a complex number, allowing for absorption or gain by the particulate medium, the numerical results presented here are all for real refractive indexes. The effects of absorption on the scattering characteristics and on the morphology-dependent resonances are well documented [47, 169], and will be dealt with explicitly where relevant to our experiments.

Several well-known [169] features of the extinction efficiency are demonstrated in figure 3.1 showing the computed Q_{ext} for a homogeneous circular dielectric fiber of refractive index $m = 1.5$. These are:

1. The efficiency tends to zero as x approaches zero,

2. The efficiency tends to two as $x \rightarrow \infty$

3. There is a low-frequency fluctuation on the curves ('the interference structure')

4. There is a high-frequency structure on the curve ('the ripple structure').

(1) above is consistent with the theory of scattering by small particles (Rayleigh scattering), while (2) represents the so-called 'extinction anomaly'-that the total extinction cross-section of a particle is twice the projected geometrical cross-section. The interference structure, which is found in the extinction efficiencies of spheres as well as that of fibers, was first explained by the Dutch astronomer van de Hulst, while the ripple structure, known alternatively as the 'whispering-gallery mode' or

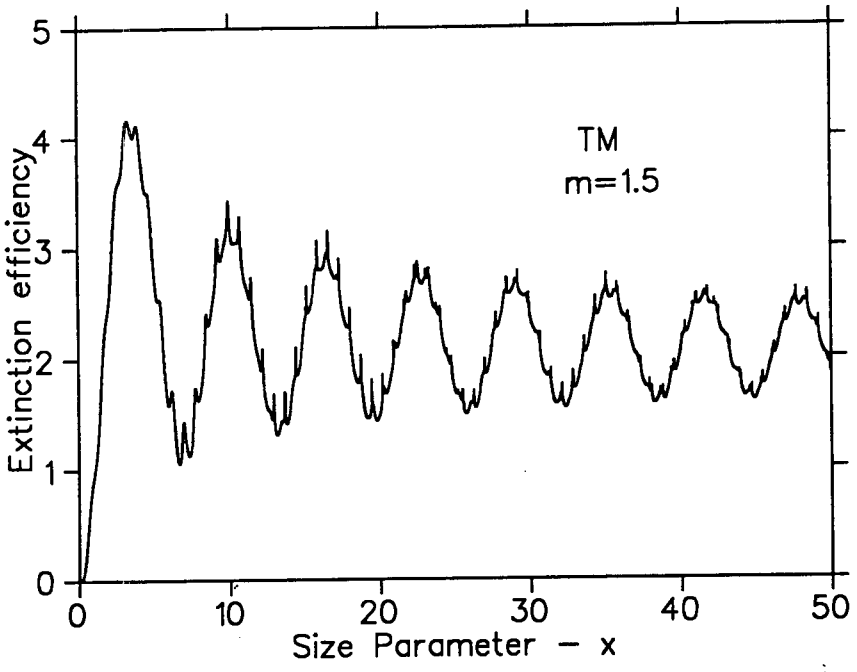

Figure 3.1: Computed extinction efficiency of a normally-illuminated homogenous cylinder with refractive index $m = 1.5$, for TM illumination.

the 'morphology-dependent resonance' structure, has been the subject of intensive investigation over the past decade.

3.4.1 The interference structure and anomalous diffraction theory

H. C. van de Hulst explained the low-frequency oscillations observed in the calculated extinction efficiency of spheres and homogeneous cylinders as being due to interference between the refracted and diffracted rays [169]. In the forward direction, the refracted rays are phase-shifted with respect to those which do not transit the scatterer, and the two may interfere constructively or destructively, depending upon the phase shift which is a function of the size and refractive index of the homogeneous scatterer. If the refractive index of the scatterer is close to that of the continuous medium, then rays incident near-centrally upon the scatterer will suffer very little angular deviation while transiting the object: in addition the effect of reflection upon the scattering characteristics will be small. The low-frequency features of the extinction efficiency may then be understood in terms of homologous scattering diagrams, in which the parameters of importance are no longer the size

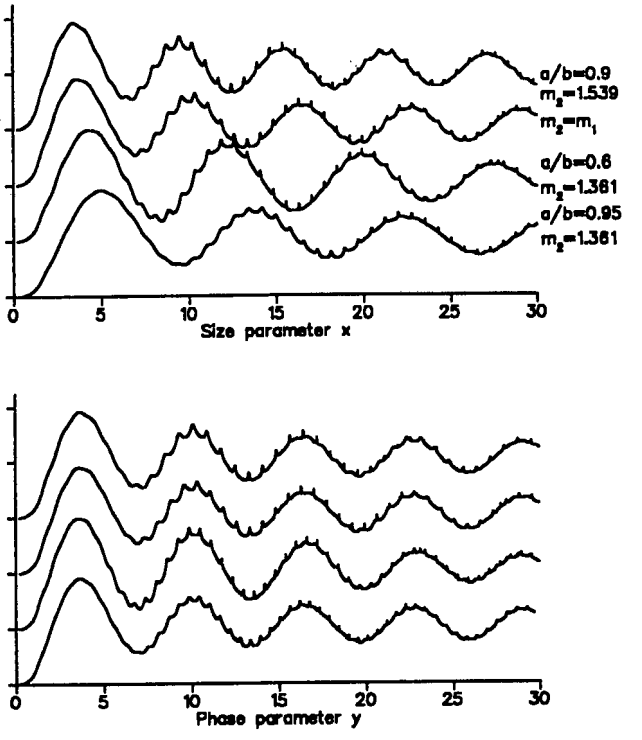

Figure 3.2: Upper plot: Computed TE extinction efficiencies of several liquid filled glass ($m_1 = 1.5$) capillaries, with parameters as indicated. Lower plot: The same curves plotted as a function of the phase parameter y. In both cases, the curves are offset for clarity.

parameter x and the refractive index m seperately, but the phase parameter y, given by

$$y = 2x(m-1) \tag{3.40}$$

for the homogeneous sphere or fiber, and the extinction efficiencies for different values of the refractive index have the same period when plotted as a function of y.

Figure 3.2 (upper plot) shows the extinction efficiencies of several liquid-filled glass ($m_1 = 1.5$) capillaries with parameters a/b and m_2 as indicated. In analogy with equation 3.40, we now define the phase parameter for a concentric-cylinder geometry as

$$y = 2x\left[(m_2-1)\frac{a}{b} + (m_1-1)\frac{b-a}{b}\right] \tag{3.41}$$

and the same curves, now plotted as a function of y, are shown in figure 3.2 (lower plot). It will be noted that the period of the interference structure is now the same

in all cases. This suggests that the anomalous-diffraction approximation may be a useful aid to determining the main features of the scattering characteristics of the normally-illuminated concentric-cylinder, in a similar fashion to that investigated by Stephens [158] for the obliquely-illuminated homogeneous cylinder and by Chylek and co–workers [46, 50] for a variety of homogeneous scatterers. Such an approximation is strictly valid only for the case $m \rightarrow 1$, but, as has been shown by van de Hulst [169] and by several other authors [46, 50, 158], the results are often useful for considerably higher values of m. Assuming that $m \rightarrow 1$, all rays falling upon the cylinder are refracted without any angular deviation, their passage through the scatterer affecting only the phase of the ray. With reference to figure 3.3, the rays with impact parameter such that $\cos\tau > a/b$ will pass only through the cladding region, and will experience a phase shift

$$\psi_1 = \frac{2\pi}{\lambda}(m_1 - 1)u \tag{3.42}$$

where $u = 2b\sin\tau$, while those rays with $\cos\tau < a/b$ will have

$$\psi_2 = \frac{2\pi}{\lambda}[(m_1 - 1)(u - v) + (m_2 - 1)v] \tag{3.43}$$

where $v = 2a\sin\tau'$ and $\tau' = \arccos(b\cos\tau/a)$

In the plane behind the fiber and normal to the direction of propagation of the incident wave, the field outside the geometrical shadow region is set equal to 1: the field in the shadow is then $e^{-i\psi}$, which represents the sum of the incident and scattered waves. The forward-scattered amplitude is thus found by integrating over the projected area A to be given by

$$S(0) = \frac{k^2}{2\pi}\int\int_A [1 - e^{-i\psi(t)}]dtdl \tag{3.44}$$

where l is the length of the fiber, and the extinction efficiency is given by

$$Q_{ext} = \frac{4\pi}{k^2 A} Re(S(0))$$

Substitution of the phase shifts 3.42 and 3.43 yields

$$Q_{ext} = \frac{k}{x}\left[2\int_a^b (1 - e^{-i\psi_1})dt + 2\int_0^a (1 - e^{-i\psi_2})dt\right] \tag{3.45}$$

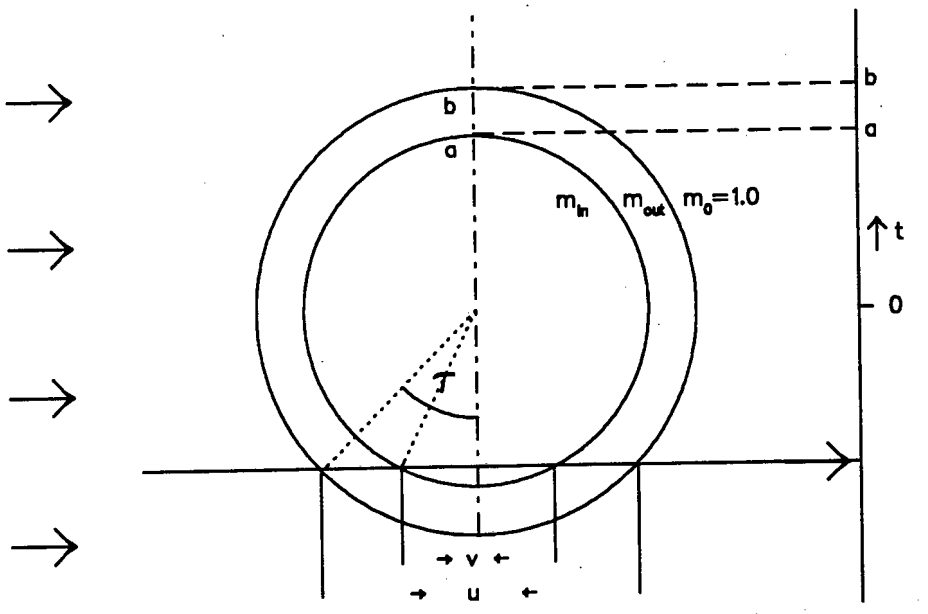

Figure 3.3: Schematic diagram showing the paths through a cladded cylinder as a function of the impact angle τ. The illuminating plane wave is incident from the left of the figure, while the anomalous-diffraction calculation is performed in the plane on the right.

and these integrals must be performed numerically.

Some comparisons of results obtained by the use of equation 3.45 with the corresponding results from the exact solution are presented in figures 3.4 and 3.5. Figure 3.4 shows the extinction efficiency of some normally-illuminated air-filled ($m_2 = 1.00$) glass ($m_1 = 1.5$) capillaries of differing a/b, for comparison with the results published by Evans *et al.* [61] over a more limited range of x. In all cases, the basic period of the interference structure is accurately predicted by the anomalous diffraction approximation. However, the exact solutions, particularly for $a/b = 0.5$, do not display a simple interference structure; smaller additional peaks not predicted by eqn. 3.45 appear superimposed on the curves. These may be due to reflection of light from the internal surface of the capillary, not taken into account in equation 3.45, or they may be due to substantial refraction of the transmitted light out of the forward direction due to the relatively large refractive index [121]. Figure 3.5 shows a glass capillary with $a/b = 0.7$ for two different values of m_2, corresponding to cores composed of ethanol and benzyl alcohol. Again, the basic

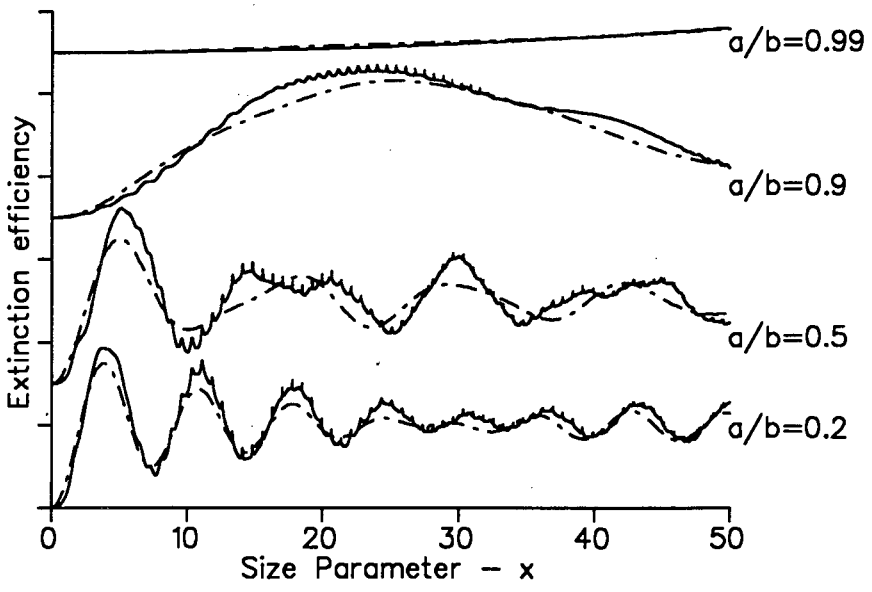

Figure 3.4: TE extinction efficiencies for air-filled normally-illuminated glass ($m_1 = 1.5$) capillaries of differing a/b computed using the exact theory (solid lines) and the anomalous-diffraction approximation (dotted lines)

period of the interference structure is accurately predicted by the use of eqn 3.45 in all cases. In conclusion, the interference structure in the computed extinction efficiency of a normally-illuminated concentric-cylinder may be understood in terms of anomalous-diffraction theory, even for relatively large values of the refractive index. Calculations using the anomalous-diffraction theory are extremely fast compared to those using the exact solution, particularly for large values of the size parameter. When there is a large discontinuity in the refractive index at the core-cladding interface, additional peaks appear in the exact solution, which are not predicted by the anomalous-diffraction theory.

3.4.2 The off-resonant internal and nearby external electromagnetic fields

The general features of the internal and nearby external electromagnetic fields associated with normal illumination of a capillary or cladded fiber are easily demonstrated by the numerical evaluation of equations 3.1- 3.5 and 3.15- 3.18 for some practical values of the parameters a, b, m_2, m_1 and λ. The results presented here are for

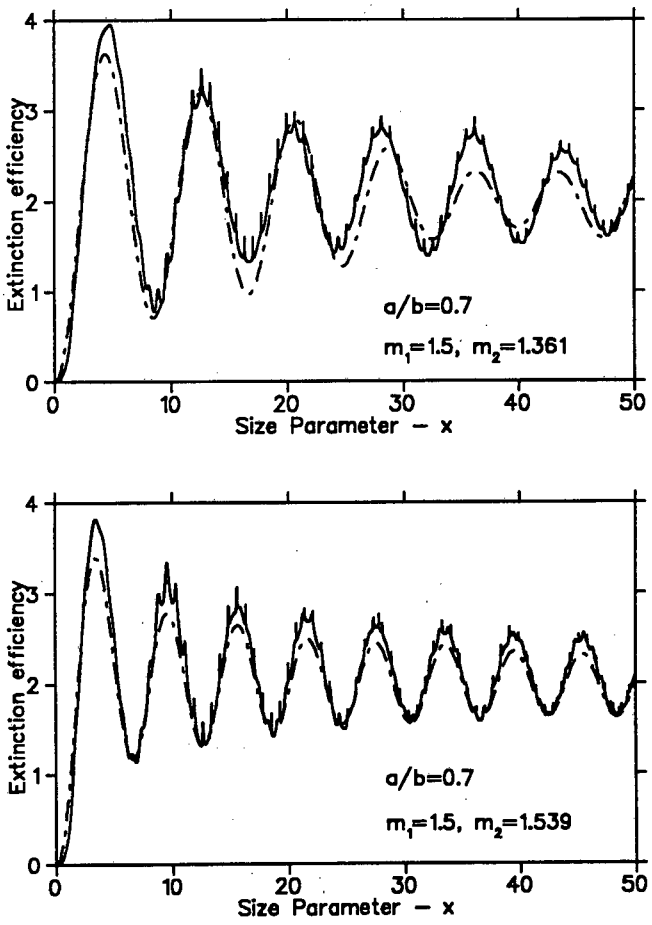

Figure 3.5: Comparison of anomalous diffraction approximation (broken lines) with exact theory for extinction efficiency of a glass ($m_1 = 1.5$) capillary with $a/b = 0.7$ filled with ethanol (upper plot) and benzyl alcohol

TM illumination; the results for TE illumination are, however, similar. We briefly review the features of the fields due to a homogeneous fiber [16, 130] by presenting figures 3.6 and 3.7, being surface plots of the internal and near-external field intensity $\underline{E}.\underline{E}^*$ associated with a fiber of radius $b = 50\mu m$ and real refractive index $m = 1.5$, illuminated with light of wavelength $\lambda = 600$nm. The dimensions of the plots are $\pm b$ and $\pm 4b$ for the internal and external field plots respectively, and the external field in the former and the internal field in the latter have been artificially set to zero in the computations. The illuminating plane wave is incident from the upper left of the diagram. The illuminated surface of the fiber focusses the transmitted light, causing a higher intensity near the shadow face of the fiber. This light is brought to a focus outside the fiber on the shadow side at a distance of about $1.5b$ from the centre of the fiber. A shadow of approximately the width of the fiber is cast by the fiber in the near field. The ray-like nature of the scattering is evident in the plots.

We now demonstrate the effect upon the fields of introducing a core region of different refractive index. Maintaining the external size of the fiber at $b = 50\mu$m and the refractive index at 1.5, we postulate a core region centred in the fiber, with a radius of $a = 20\mu$m. Introducing a highly refractive solvent (di-iodomethane - $m_2 = 1.738$) into the core causes the core region to act as an additional focussing lens within the fiber (figure 3.8). Light which transits the core region of the fiber is now brought to a focus in the cladding region, causing a increase in the local field intensity in the fiber cladding. The maximum value of $\underline{E}.\underline{E}^*$ in the cladding region is now $33.7I_0$. (A similar plot for parameters directly relevant to the experiments to be described in chapter 5 is shown in figure 5.13.) A larger core region filled with a similar solvent causes a similar effect, but the focal point of the core lens no longer falls within the fiber cladding. Instead, the external field exhibits a second peak, which is nearer to the surface of the fiber than the peak corresponding to that observed in the field from a homogeneous fiber. A similar fiber filled with air (figures 3.9 and 3.10) shows a rather different field pattern. In this case, rays which pass through the fiber core are defocussed by their passage, and are diverted out of the forward direction over a range of angles. This effect is clearly seen in both the

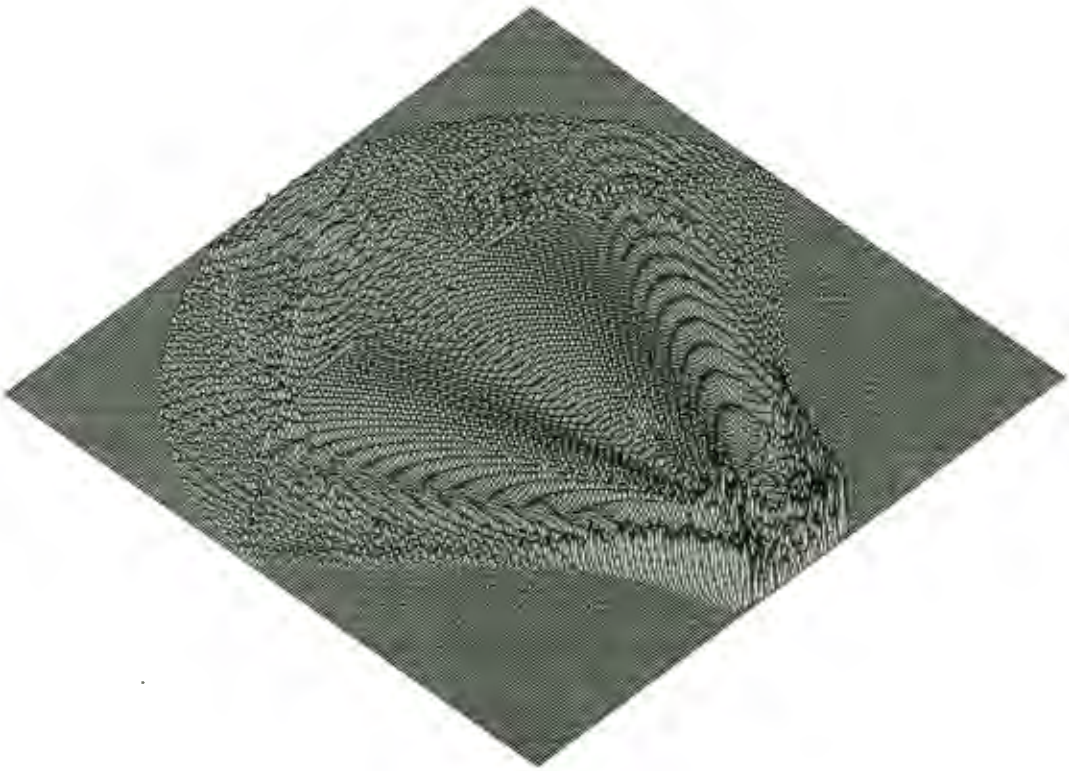

Figure 3.6: Computed TM source function within a normally-illuminated homogeneous glass ($m = 1.5$) cylinder. The illuminating plane wave is incident from the upper left of the diagram, while the dimensions of the plot are $\pm b$ in both directions in the plane of the illuminating wave. The external field has been artificially set to zero in the calculation. Light is focussed by the curved illuminated surface of the cylinder, causing a larger intensity near to the shadow face, of magnitude about $10\times$ the incident field intensity.

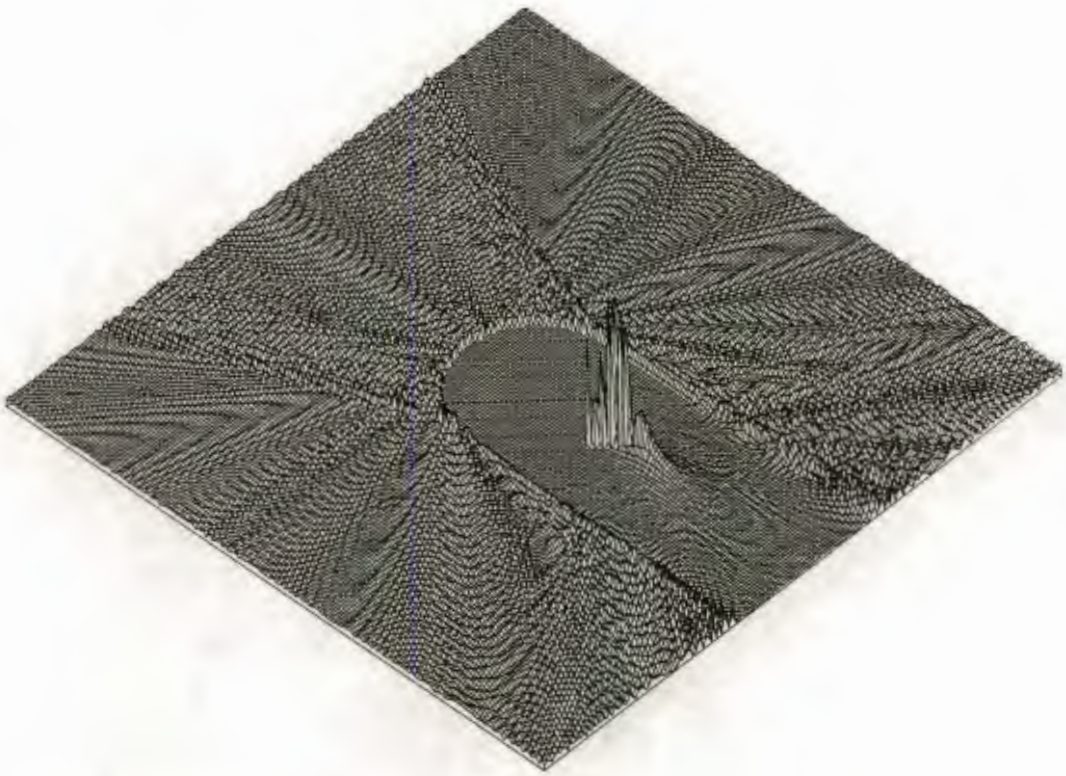

Figure 3.7: Computed TM electric field intensity $\underline{E}.\underline{E}^*$ outside a normally-illuminated homogeneous glass cylinder. The dimensions of the plot are $\pm 4b$ in both directions. The shadow cast by the cylinder, and the bright spot caused by the cylindrical lens are both demonstrated in the plot. The maximum intensity is 45.3× the incident field strength. The field inside the cylinder has artificially set to zero in the computation.

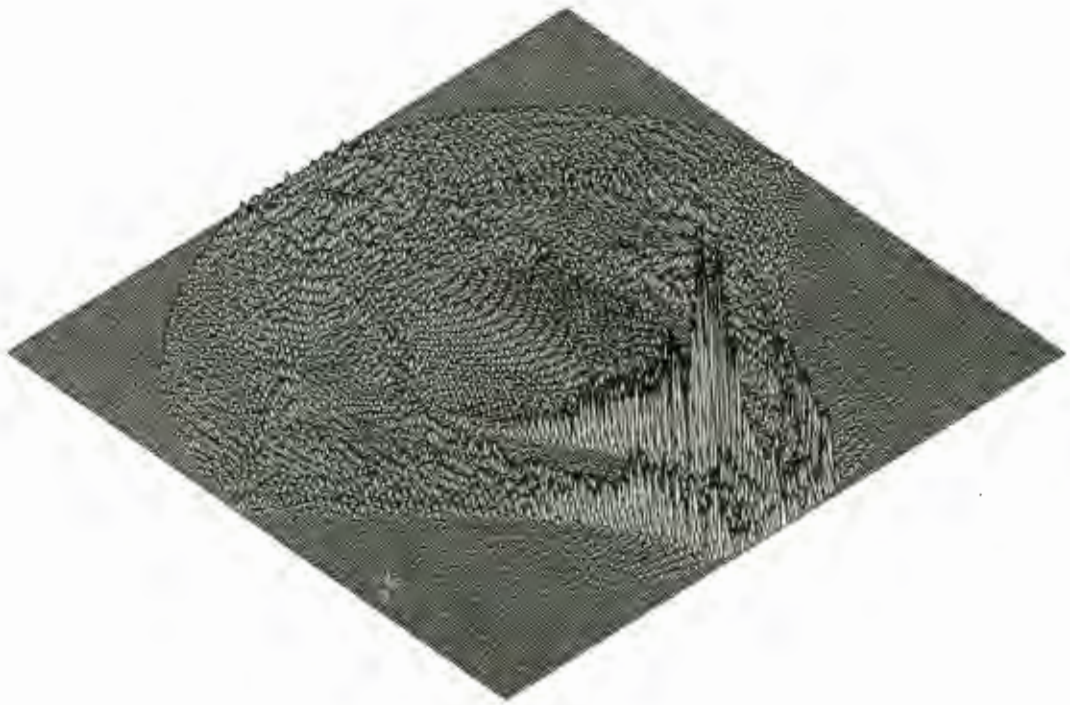

Figure 3.8: Internal source function inside a capillary fiber with $a = 20\mu$m, $b = 50\mu$m, $m_1 = 1.5$ and $m_2 = 1.738$, for TM illumination. The highly refractive core region casts a shadow within the fiber cladding, and causes a new focal spot within the cladding region. The maximum value of the source function is $33.7I_0$.

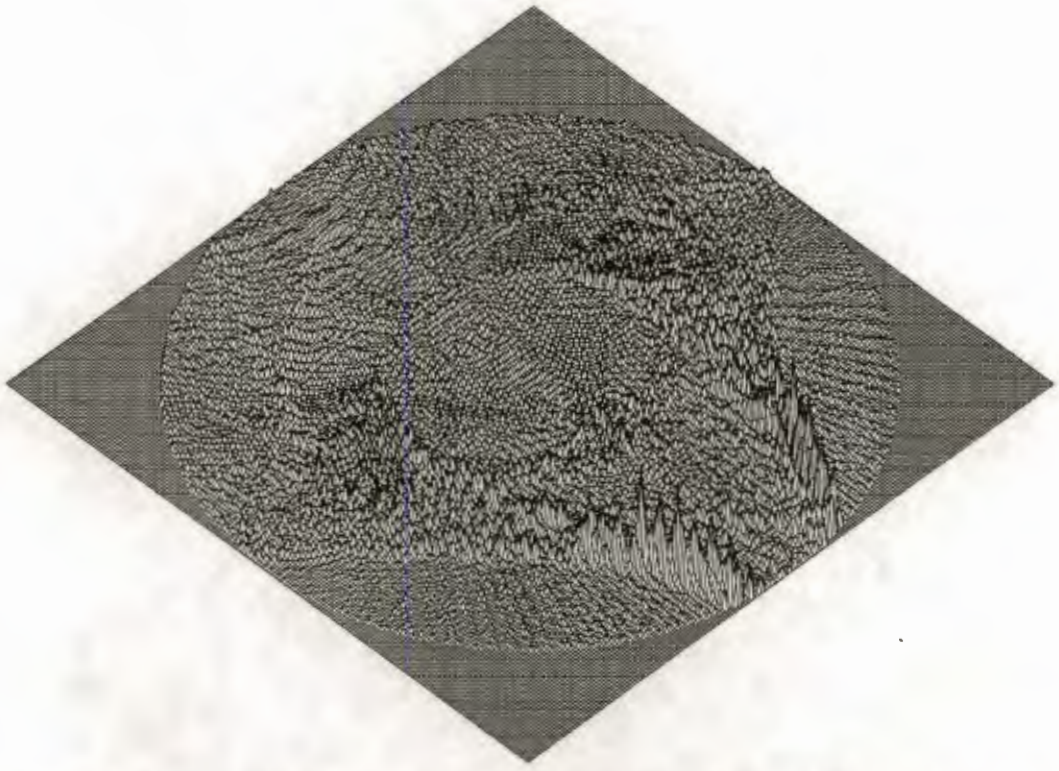

Figure 3.9: Internal field for the same fiber as that shown in the previous figure but with air in the core region. This serves to defocus the light passing through it, which has a clearly observable effect on both the internal and the external fields. The maximum value of the source function within the fiber is now $15.3I_0$.

internal and the external field plots when these are compared with those previously presented for the homogeneous fiber.

In order to demonstrate some of these features experimentally, we have studied the external fields produced by the normal illumination of some commercially available capillary fibers with an unfocussed laser beam. This was done by mounting the fibers horizontally in a dye-doped solution of water in a cuvette. The dye used in the experiments (Oxazine 170) was readily excited by the red ($\lambda = 632.8$nm) radiation from a polarized 10mW HeNe laser beam, which was used to illuminate the fibers from below. The intensity of the fluorescence at $\lambda > 632.8$nm observed from the dye-doped water at any point may be assumed to be proportional to the intensity at that point of the pump field at 632.8nm (i.e. to the scattered near-field.) Thus the observed fluorescence intensity is used to map the scattered near-field. A

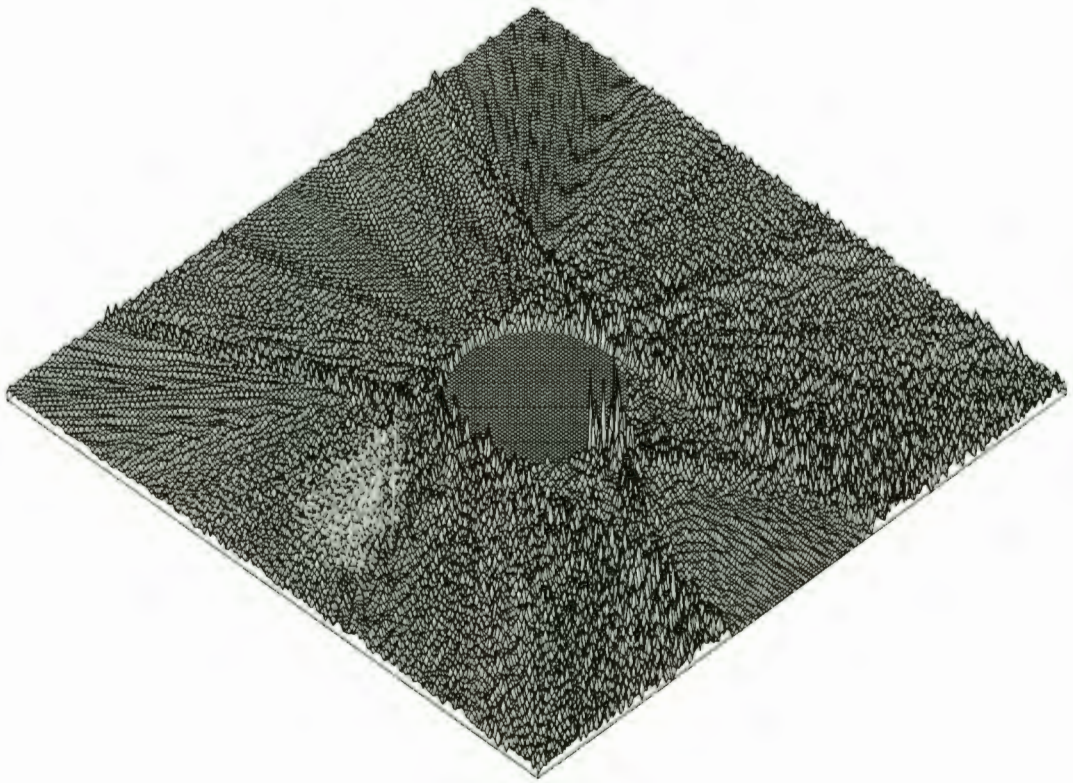

Figure 3.10: External field corresponding to the air-filled capillary. The peak in the near-field source function has a magnitude $7I_0$.

similar technique employed by Benincasa *et al.* [16] to map the near-field patterns of homogeneous spheres and cylinders in air used I_2 vapour as a fluorescent medium. A microscope was used to image ($\times 17$) the fiber and the fluorescence onto the colour film of a 35mm camera. Corresponding calculations were performed using the wavelength of the HeNe beam in water ($\lambda = 474.7$nm) and the refractive indexes of the fiber and solvents relative to that of water. The glass capillary fibers used in the experiments were some of those obtained commercially from Polymicro Technologies, and used in other experiments to be described. The parameters of the fibers were $m_1 = 1.458$, $2a = 50 \pm 3\mu m$ (both from the manufacturers specifications) and $2b = 126 \pm 3\mu m$ (measured with an optical microscope). The core materials used in the prints shown here were air ($m_2 = 1.00$) and di-iodomethane ($m_2 = 1.738$). The results are shown opposite. The fiber axis is perpendicular to the plane of the paper, i.e. the fiber projects out of the page. The HeNe beam is incident from the bottom of the photograph. The fiber appears as a dark circle near the bottom of the pictures. Above the fibers, the focussing effect of the the scatterers and the shadow region are clearly observed. The focal point of the transmitted light occurs a relatively long way from the fiber because of the small refractive index mismatch at the fiber surface. The results of the corresponding computations are shown as contour plots on the right. The agreement between the experimental and theoretical results is excellent. One effect of changing the core material is immediately obvious in both the experimental and the theoretical plots: the additional focussing or defocussing of the transmitted light by the higher or lower refractive index core material respectively. This causes a bright or dark spot to occur in the external field near to the shadow face of the fiber; this spot is highly visible in the plots. The maximum intensities in the theoretical plots are $11.3\times$ the incident field for the air-filled case, which occurs at about $2b$ from the origin, close to the axis in the forward direction, and $34.5\times$ the incident field for the di-iodomethane filled capillary, occurring on the fiber axis and virtually on the fiber surface in the forward direction. This very large peak is the brightest feature in the experimentally-observed near-field region.

Another difference between the two theoretical plots is observable in the 'ray-like' effect formed by the contours. The ray-like features formed near to the forward

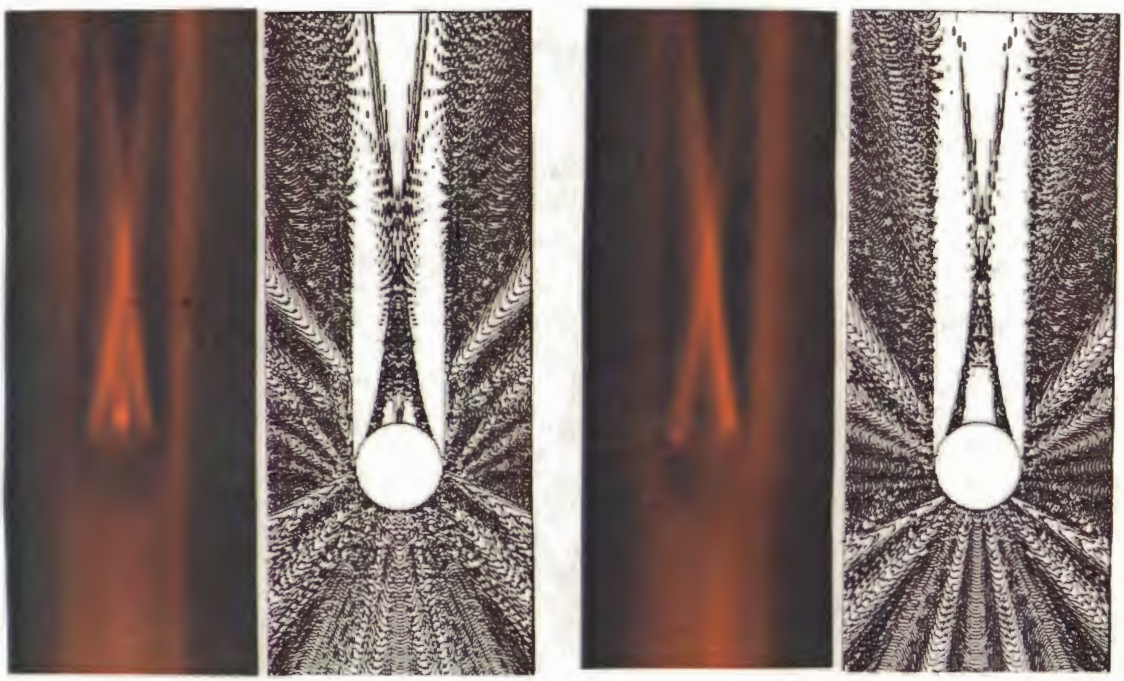

Figure 3.11: Photographed near-field scattering pattern from a capillary fiber suspended in water doped with a fluorescing dye (oxazine 170) and filled with di-iodomethane ($m_2 = 1.738$) (left photo) and with air (right photo). Contour plots of the corresponding computed near fields are shown to the right of each photo. The fibers are normal to the plane of the page, and are visible as a dark circle near the foot of the photographs. The main differences between the two cases are the focus just outside the shadow face of the di-iodomethane-core fiber visible in both the experimental and the theoretical plots (on the right) and its absence from the air-core case, and the apparent origin of the ray-like structures in the near-forward scattering, which point well within the fiber for the air-filled case.

direction for the high-index case (lower plot) appear to originate from the high-intensity peak at the shadow face on the fiber axis. The features in the corresponding position on the air-filled plot, however,point well within the fiber. The directionality of these features is caused by that light which has transitted the core region of the fiber: for $m_2 = 1.738$, this light has been brought to a focus near to the cylinder surface, and thereafter continues outward; for $m_2 = 1.00$, however, this light is refracted into wider angles before reaching the shadow face of the fiber.

3.4.3 Morphology-dependent resonances in the normally-illuminated layered cylinder

Morphology-dependent resonances in the scattering functions of homogeneous microparticles correspond to the excitation of the natural resonant frequencies of the cavity defined by the refractive index discontinuity at the microparticle surface. They occur if the refractive index within the cavity is greater than that outside, and if the cavity is sufficiently large. In the capillary fiber being investigated here there are potentially two such cavities, each of which may possess a distinct resonance spectrum. The first cavity is defined by the external surface of the fiber, and if the core size is substantially less than the total size of the fiber, this external surface can result in MDRs entirely analogous to those which have been observed in the elastic and inelastic scattering from homogeneous spherical and cylindrical scatterers of the same size. A second cavity may be formed within the fiber core if the core refractive index is greater than that of the cladding. The enhanced fields associated with resonances in such a cavity will be almost entirely confined within the core region of the fiber. Such resonances may be barely visible in the elastically scattered light. However, they can result in substantial enhancement of fluorescence and lower the threshold for laser emission from a dye-doped liquid flowing in the capillary. We shall refer to resonances in the two cavities as 'cladding' and 'core' resonances respectively, although, as we shall show, the resonances of the two cavities are coupled together under certain conditions.

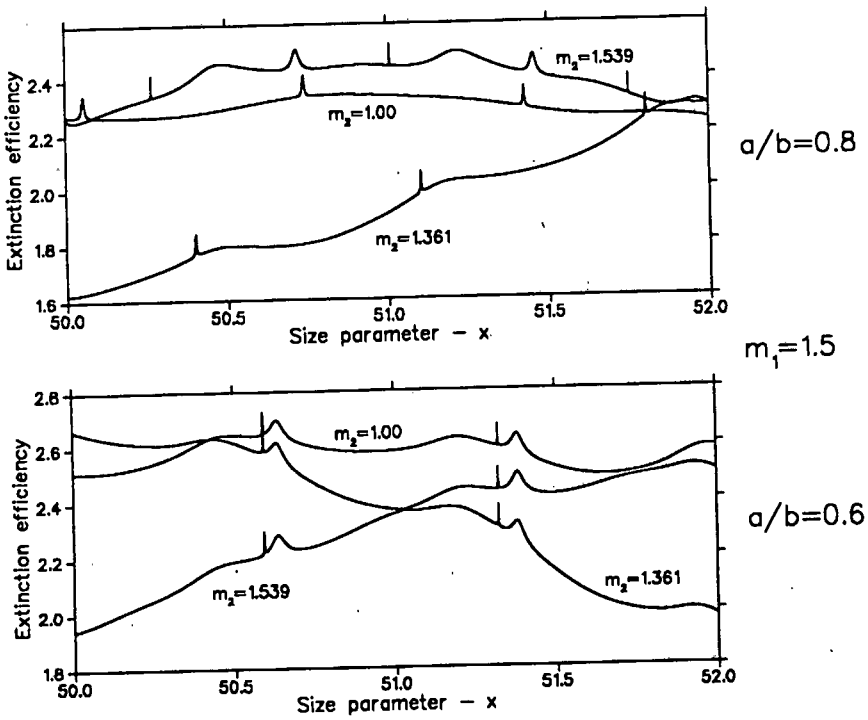

Figure 3.12: Computed TM extinction efficiencies for two glass capillaries ($m_1 = 1.5$) with $a/b = 0.6$ and $a/b = 0.8$, filled with air, ethanol ($m_2 = 1.361$) and benzyl alcohol ($m_2 = 1.539$)

3.4.3.1 Resonances associated with reflections at the external surface (cladding resonances)

Before investigating some of the features of MDR's in the concentric-cylinder it is again instructive to study the extinction efficiency for some assumed geometries. The cladding MDR's are visible as the 'ripple structure' in figure 3.2; we now investigate the ripple structure over a smaller region of x in more detail, again confining our attention to the case of a glass ($m_1 = 1.5$) capillary filled with air, ethanol and benzyl alcohol. Figure 3.12 a-f shows these three cases for two different values of the parameter a/b: $a/b = 0.6$ (lower plot) and $a/b = 0.8$ (upper plot). As expected, the low-frequency interference structure is significantly altered by the changing refractive index, both for $a/b = 0.6$ and for $a/b = 0.8$. However, the location and widths of the MDR's are virtually unaffected by changing the core refractive index for the case $a/b = 0.6$, a strong indication that the additional light scattered at resonant

wavelengths never transits the central portion of the scatterer. In contrast, the density of modes, their positions and halfwidths are all significantly affected by increasing the refractive index of the core when $a/b = 0.8$. (Compare ripple structure in the lower and upper plots in figure 3.12) This is easily explained in terms of the known features of MDRs in homogeneous cylinders and spheres; the enhancement of the internal electromagnetic fields which is associated with the excitation of the natural resonances of the scatterer occurs close to the surface of the particle. For $a/b = 0.6$ the enhancement of the fields occurs only in the cladding or glass region of the fiber: the resonances are thus unaffected by changes in the core refractive index. A similar effect has been studied in the scattering by a layered spherical particle by Hightower and Richardson [77]. As a/b is increased, significant overlap of the enhanced near-surface fields with the central core region of the fiber occurs and the resonances become sensitive to changes in the core index. This is demonstrated by the angle-averaged internal field intensities associated with resonant conditions in the fiber. These may be studied by numerically averaging the internal electric source function $\underline{E}.\underline{E}^*$ over all possible angles in the scattering plane, and then plotting this as a function of the radial distance from the centre of the fiber. Similar plots have previously been presented for homogeneous cylinders and spheres [130, 48], where, among other things, it was demonstrated that the order of the resonance gives the number of peaks in the radial dependence of the mode. Plots are shown in figure 3.13 for both TE and TM resonances for the case $a/b = 0.8$, and for the TE case for $a/b = 0.6$, all for $m_1 = 1.5$, $m_2 = 1.539$. The incident plane wave is assumed to be of unit intensity. The occurrence of a discontinuity in the value of $\underline{E}.\underline{E}^*$ at a refractive index mismatch for the TE case, and its absence for the TM case, previously noted to occur at the surface of a homogeneous fiber [130], is seen here to occur at the internal boundary as well. The reason for this is that the electric field vector in the TM case has only a tangential component, which is then required to be continuous at the boundaries. For the TE case, the electric field has both a radial and a tangential component. Furthermore, it is observed that the enhanced fields associated with the resonance occur only in the cladding for $a/b = 0.6$, but that significant enhancement occurs in the core of the fiber for $a/b = 0.8$. Loosely

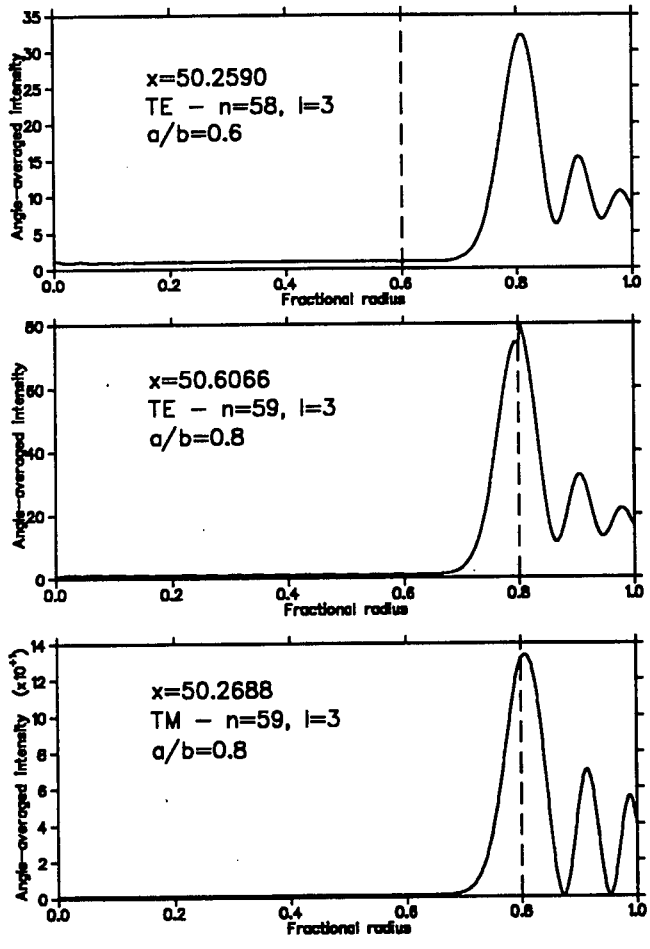

Figure 3.13: Computed angle-averaged internal field intensities corresponding to different resonant conditions for the fibers of the previous figure. The top curve shows a TE resonance for the case $a/b = 0.6$, $m_2 = 1.539$. The lower plots show intensities for TE and TM modes for the case $a/b = 0.8$,$m_2 = 1.539$. Note the appearance of a discontinuity in the plot for the TE resonance at the internal interface.

interpreting the value of the source function at any point as being proportional to the probability of 'finding' a photon at that point at any given time leads to the conclusion suggested above, namely that the additional light observed at resonant frequencies never enters into the core region for the case $a/b < 0.6$.

For an intermediate value of a/b, we now investigate the effect of changing the refractive index of the core upon the resonant internal field distribution. We have seen that, if the resonant fields overlap with the core region, the density, halfwidths and $x-$locations of the MDRs are affected by the core refractive index. We find that for $a/b \simeq 0.7$ such overlap occurs for high- but not for low refractive index core materials. This is particularly true for larger fibers. Figure 3.14 shows the angle-averaged source functions $\underline{E}.\underline{E}^*$ for two resonances of similar halfwidth $\frac{\Delta x}{x} \simeq 10^{-5}$ which occur near $x = 400$ for the case $a/b = 0.7$, $m_1 = 1.5$, and for $m_2 = 1.361$ and 1.539 respectively. The core/cladding interface is marked as a dotted vertical line on the plots. The overlap of the resonance-enhanced source function with the core is greatly increased by increasing the refractive index of the core material from that of ethanol ($m = 1.361$) to that of benzyl alcohol ($m = 1.539$) and the order of resonance having a comparable width is higher. Some insight may be gained by adopting the laws of geometrical optics (i.e. rectilinear propagation, reflection and refraction) if one visualises a high-Q resonance occurring by the repeated total internal reflection of a ray from the external surface of the fiber. If the angle of incidence upon the surface is large, many such reflections may occur, the ray being 'trapped' near to the fiber surface. Now consider the concentric-cylinder of interest in the present work. It is easily shown that a ray which has been reflected from the external surface at greater than the critical angle (i.e. totally internally reflected) will intercept the core/cladding boundary if the condition

$$\frac{a}{b} > \frac{1}{m_1} \tag{3.46}$$

is satisfied. Equation 3.46 gives the value $a/b > 0.67$ for $m_1 = 1.5$. However, if the core index is less than that of the cladding, a ray incident tangentially upon the internal interface will be totally 'externally' reflected, and will be unable to penetrate the core. Now there is the more stringent condition that the angle of

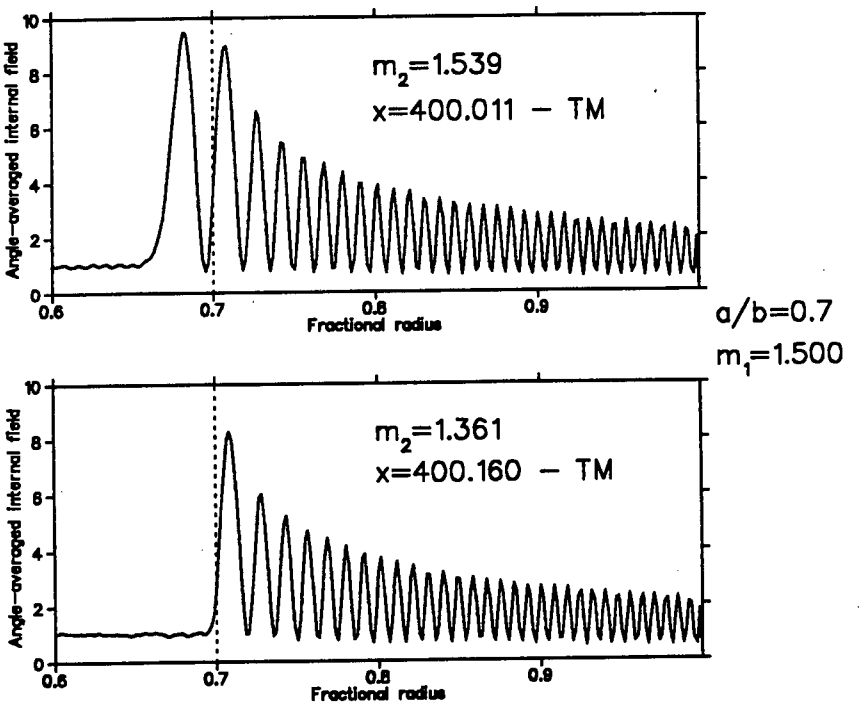

Figure 3.14: Angle-averaged TM source functions for two resonances in a glass capillary with $a/b = 0.7$, filled with ethanol and benzyl alcohol. Significantly greater overlap of the resonant fields with the core region occurs for the case when the core refractive index is greater than that of the cladding, and the mode order is higher. The two modes shown here have similar computed Q-values. The upper plot corresponds to the case when the two cavities are coupled together.

incidence of the ray upon the internal interface should be less than the critical angle for the core/cladding boundary, leading to the condition

$$\frac{a}{b} > \frac{1}{m_2} \tag{3.47}$$

or $a/b > 0.735$ for an ethanol-filled glass fiber. Investigations of the angle-averaged resonant field distributions inside a normally-illuminated concentric-cylinder for a wide range of size parameters and refractive indexes have shown that the equations 3.46 and 3.47 can provide a reliable estimate of the conditions under which significant resonant field enhancement will occur in the fiber core at a cladding resonance.

3.4.3.2 Core resonances in a cladded fiber

The cavity formed by the refractive index discontinuity at the core/cladding interface can provide optical feedback by total internal reflection if the core refractive index is greater than that of the cladding. If this refractive index mismatch and the fiber core diameter are sufficiently large, this can lead to resonances and associated enhancement of the electromagnetic fields within the fiber core. The frequencies at which such resonances occur are virtually independent of the cladding thickness provided that light leaving the core region tangentially to the internal interface cannot be totally internally reflected from the external surface, i.e. if $a/b < 1/m_1$. Whether or not these resonances will be observable in the elastically scattered light depends upon the relative size of the capillary core. For smaller cores, the contribution to the elastic-scattering cross-section from the fiber core may be negligable: under these conditions, core resonances may barely be observable in the elastic scattering. However, the enhanced fields in the core associated with the resonance may have a dramatic effect upon those processes responding directly to the internal field, e.g. fluorescence and Raman scattering. If the core diameter is not too much smaller than that of the whole fiber, core resonances may appear as a peak or a dip in the elastic scattering characteristics, of similar magnitude to those due to cladding resonances. As an example we present the computed extinction efficiencies for TM illumination of a $b = 60\mu m$ fused-silica capillary fiber with core radius $a = 25\mu m$ (figure 3.15). The refractive indexes used in the computations

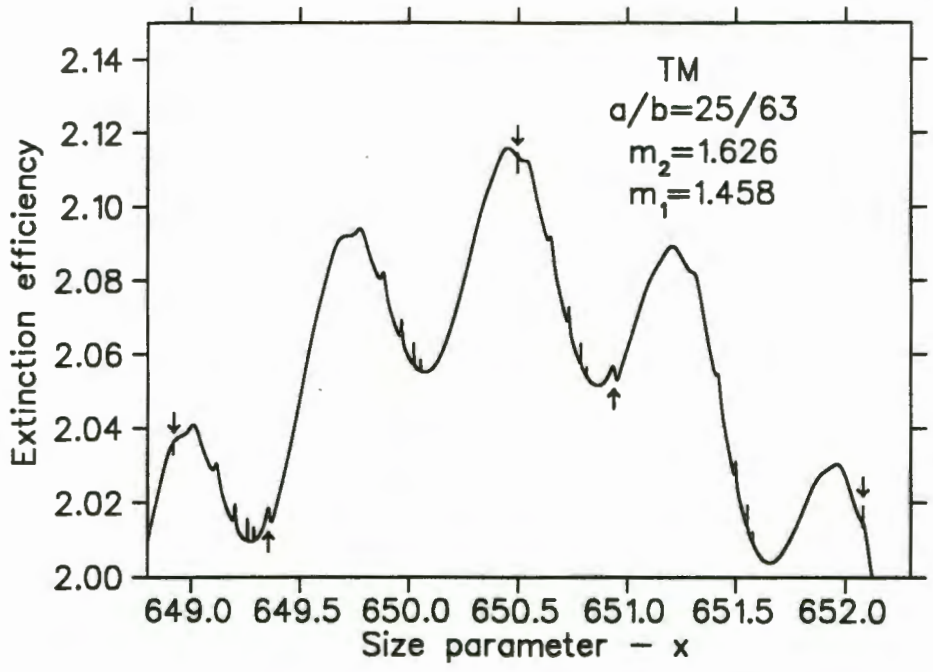

Figure 3.15: Computed TM extinction efficiency for a fused-silica capillary fiber ($m_1 = 1.458$) filled with quinoline ($m_2 = 1.626$). The core/coating ratio is 25/63. Peaks due to core resonances are indicated with arrows on the plot.

are $m_1 = 1.458$ and $m_2 = 1.626$. These parameters correspond approximately to some of the commercially-available fibers used in the experiments to be described filled with quinoline. The MDR's of the fiber appear as small peaks on the extinction efficiency curve, separated by $\Delta x \simeq 0.7$. The curve shows an additional set of regularly spaced peaks, indicated with arrows on the diagram, which are separated by more than twice this amount. These correspond to resonances occurring in the fiber core. The internal electromagnetic field intensity at one of these resonances is shown in figure 3.16. The resonance enhancement at the core/cladding interface dominates the source function plot. (An off-resonant plot of the source function for this fiber is shown in chapter 5, figure 5.13.) The angle-averaged field intensity plot (figure 3.17) shows that there are two peaks in the radial dependence of the mode, indicating a second-order core resonance. We find that the resonance occurs in the $n = 397$ partial wave, i.e. the core resonance has $n = 397, l = 2$. The enhanced fields are closely confined to the core/cladding interface, and this is related to the small relative refractive index mismatch providing the feedback. The maximum

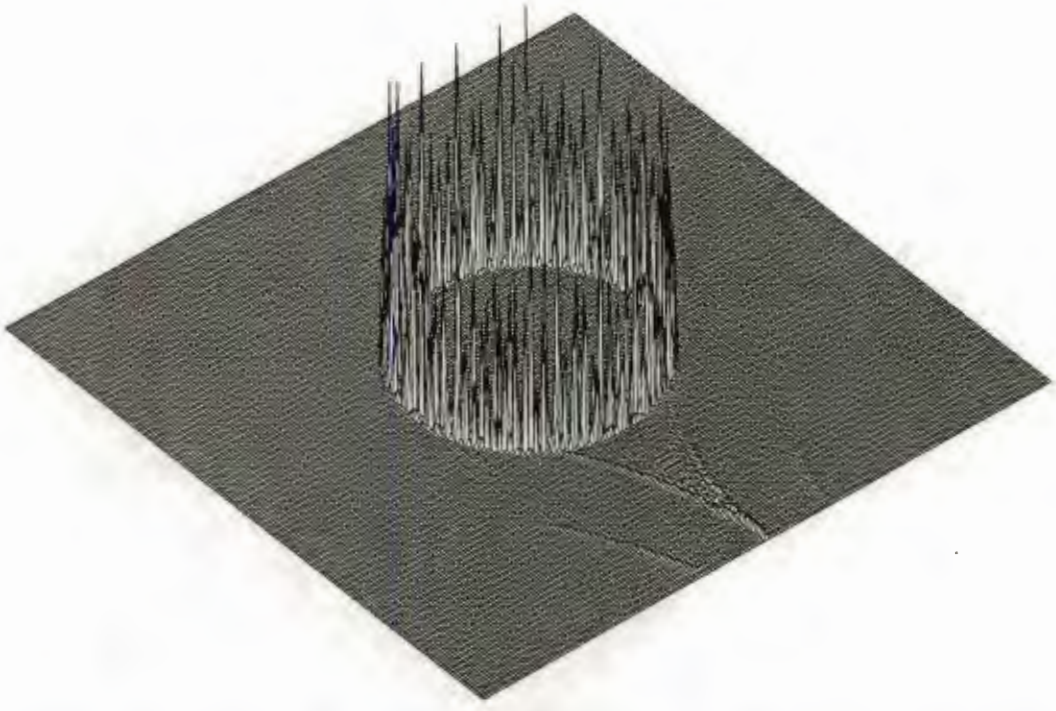

Figure 3.16: Source function inside the capillary fiber used to plot the previous figure at a frequency corresponding to one of the core resonances, at $x = 649.9163$. The dimensions of the plot are $\pm b$ in both directions, and the illuminating wave is again incident from the upper left of the figure. Resonance enhancement of the internal fields is seen to occur in the fiber core near to the core/cladding interface. The 200×200-point grid used to plot the figure is insufficient to resolve the finer details of the resonant field.

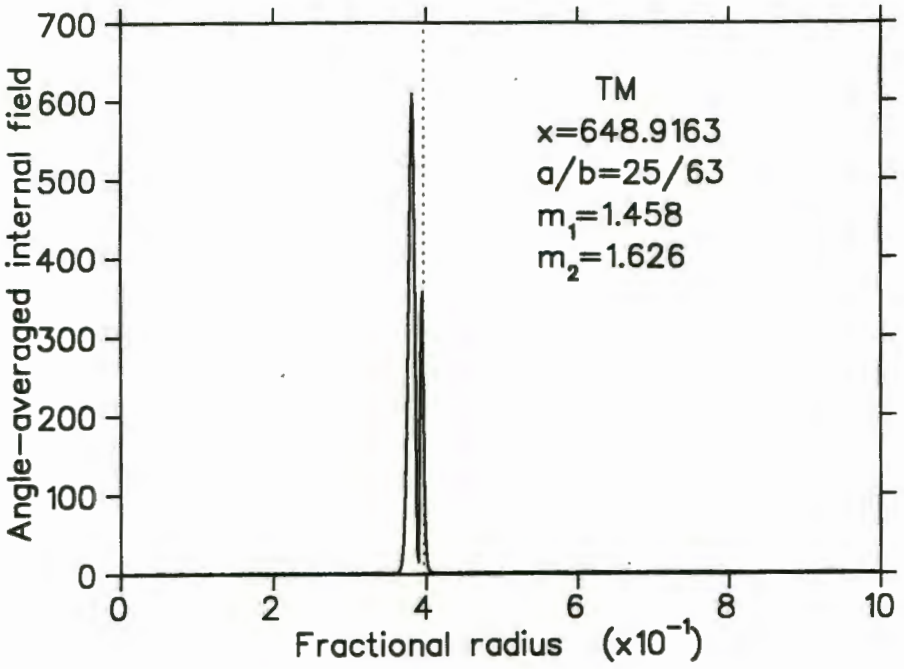

Figure 3.17: Angle-averaged field corresponding to the TM core resonance shown in the previous figure. This is a second-order core resonance, and occurs in the $n = 397$ partial wave. The dotted line indicates the core/cladding interface.

angle-averaged field occurring in the fiber core is about three orders of magnitude greater than the incident intensity. A plot for the cladding resonance at $x = 649.289$ is shown for comparison in figure 3.18.

Similar core resonances are found for smaller and larger core sizes. However, core resonances do not exist if the core radius $a > b/m_1$. In this case the cavities formed by the internal and external interfaces are coupled together; the additional feedback provided by the internal refractive index discontinuity serves to extend the cladding resonances into the core region, and both cavities resonate together (see e.g. figure 3.14). However, as $a << b/m_1$, the core resonances quickly approach the same locations and widths as those calculated for a homogeneous fiber of relative refractive index m_2/m_1 illuminated with light of wavelength λ/m_1. Consequently, the wavelengths at which the resonances occur are independent of the external diameter of the fiber. This is demonstrated in figure 3.19 where we have plotted the locations of the peaks observed in figure 3.15 (central line) as a function of the size parameter (bottom scale) and of the core size parameter $x_c = 2\pi a m_1/\lambda$ (upper scale). (This

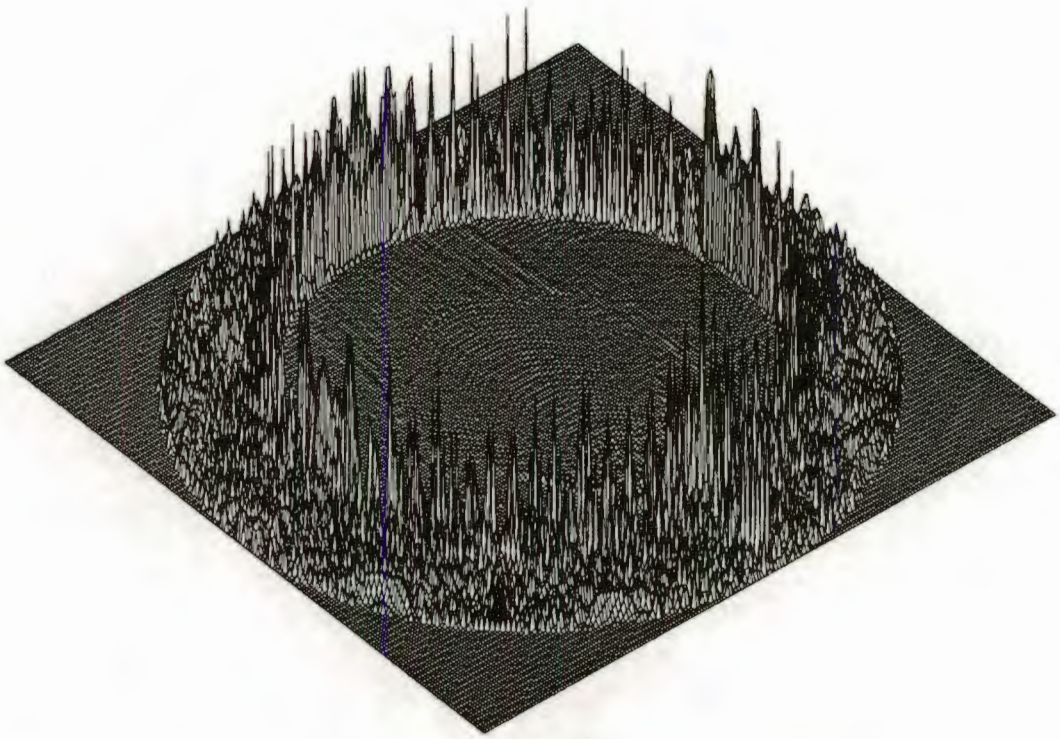

Figure 3.18: Corresponding source function plot for one of the cladding resonances (at $x = 649.289$) in the fiber of the previous figures.

definition of the core size parameter is appropriate because the light incident on the core region has wavelength λ/m_1 in the cladding region.) Also plotted are the resonance locations from a homogeneous $m = m_1$ fiber (bottom line, plotted using lower scale) and from a homogeneous $m = m_2/m_1$ fiber (plotted using upper scale). The resonance peaks of the composite fiber in figure 3.15 are seen to be traceable to resonances occurring either in the homogeneous $m = m_1$ fiber of the same size parameter or in the homogeneous $m = m_2/m_1$ fiber with size parameter equal to the core size parameter of the composite fiber. Closer investigation reveals that these are indeed the same resonances, i.e. they have the same n, l values. We can thus estimate the mode spacing of the core resonances in terms of the core size parameter using the Chýlek approximation [41] :

$$\Delta x_c = \frac{\arctan(m^2-1)^{\frac{1}{2}}}{(m^2-1)^{\frac{1}{2}}} \tag{3.48}$$

where m is the relative refractive index of the fiber core.

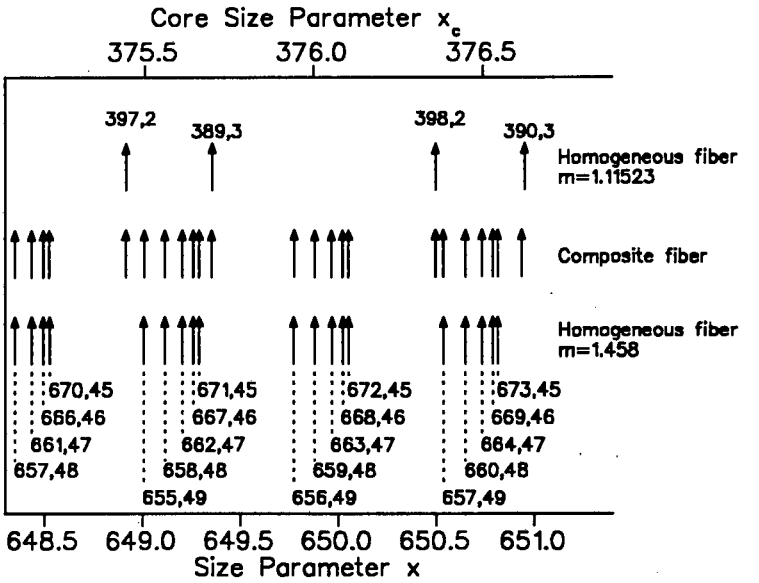

Figure 3.19: The locations of the resonant peaks appearing in the computed TM elastic-scattering spectrum of a cladded fiber (central row) when this is computed with a step size $\Delta x/x = 10^{-6}$, plotted as a function of the size parameter (bottom scale) and the core size parameter (top scale). The modal locations were computed for the parameters $m_1 = 1.458$, $m_2 = 1.626$ and $a/b = 25/63$. The upper and lower rows of modal locations, labelled with their n, l values, are those computed for homogeneous fibers with $m = 1.458$ (plotted on bottom scale) and $m = m_2/m_1 = 1.11523$ (plotted on upper scale). Peaks appearing in the composite-fiber scattering characteristics correspond to resonances computed independently for the core or for the cladding.

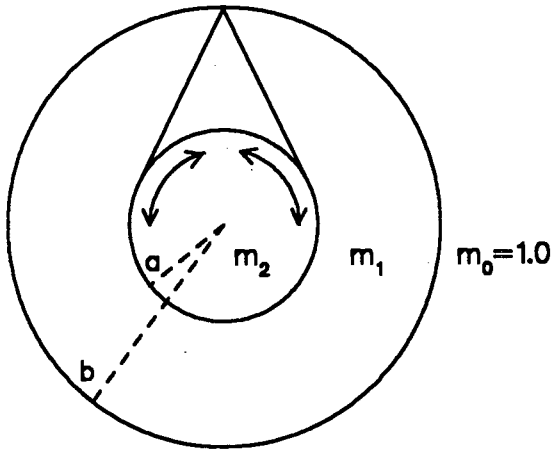

Figure 3.20: Schematic diagram of a resonant cladded fiber, showing how light leaking tangentially from the resonant core can couple back into the core region following reflection from the external surface of the cladding.

Interference enhancement of core resonances in a capillary fiber We have stated above that possible core resonances in a cladded fiber are independent of the cladding thickness, provided only that $b > m_1 a$. This is not strictly correct. Light trapped at a core resonance will leak slowly out of the core region at a rate determined by the corresponding homogeneous-fiber cavity Q-value. A fraction of this light will be reflected from the external surface of the fiber, back towards the core region. The fraction of light reflected depends on the refractive index, polarization and angle of incidence, and may be calculated using the Fresnel reflection coefficients [84]. A diagramatic representation of the situation is shown in figure 3.20. Depending upon the values of a, b, m_1, m_2 and λ, this light may be in phase or out of phase with the internally-propagating wave, leading to constructive or destructive interference in the resonant core field. The composite fiber Q-values may thus be greater than or less than those of the corresponding homogeneous-fiber resonance. The homogeneous fiber resonances of the same order occurring in successive partial waves are increasingly narrow, the associated internal field strengths increasing monotonically as a function of size parameter. The same resonances occuring in the core region of a capillary fiber have internal field strengths which fluctuate according to whether the feedback from the external surface interferes constructively or

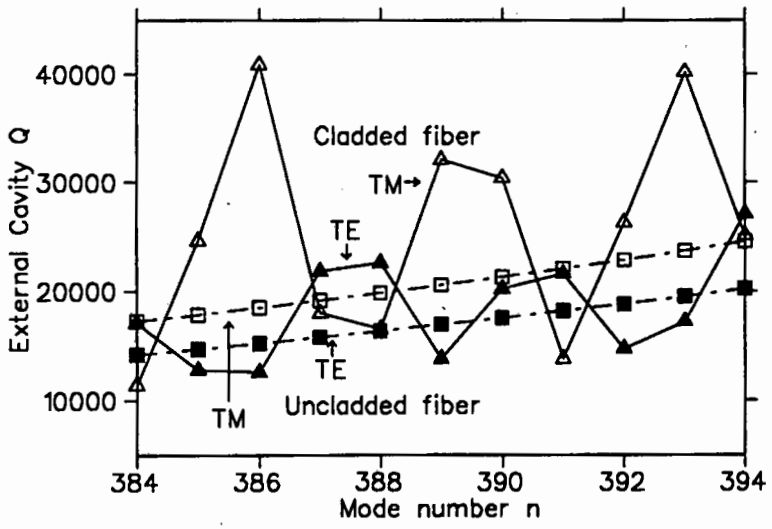

Figure 3.21: Computed values for Q_{ext} for third-order ($l = 3$) core resonances in a cladded fiber (solid lines) and for the same resonances in a homogeneous fiber of the same relative refractive index as the cladded-fiber core (broken lines) plotted as a function of the mode number n. Q-values for the cladded fiber fluctuate around the uncladded-fiber values, the TM modes (open symbols) varying more than the corresponding TE modes. Plotted symbols represent resonance Q-values: the lines are drawn only to aid the reader. The parameters used in the computations were $a/b = 25/60$, $m_2 = 1.626$ and $m_1 = 1.458$ (cladded fiber) and $m = m_2/m_1 = 1.11523$ (uncladded fiber).

destructively in the core region. From figure 3.20, the period of these fluctuations is given by

$$\Delta x = \frac{\pi}{m_1\sqrt{1-\frac{a^2}{b^2}} - m_2\frac{a}{b}\arccos(\frac{a}{b})} \tag{3.49}$$

The period of these fluctuations may be several times the characteristic mode spacing, or it may only be a fraction of this spacing leading to quasi-random fluctuations in the internal field strengths. This is demonstrated in figure 3.21, where we have plotted the Q-values for the third-order resonances occurring in a number of consecutive partial waves. The dotted line joins the monotonically-increasing points computed for the same resonances in the homogeneous-fiber ($m = m_2/m_1$) case. The Q-values for the cladded fiber fluctuate regularly around those for the homo-

geneous fiber as a consequence of the interference effect. The fluctuations are less significant for the TE modes: this is due to the fact that that the angle of incidence of the light on the external surface (figure 3.20) is near to the polarizing angle, hence only a small fraction is reflected for TE modes. Indeed, for certain combinations of the parameters the modulations disappear completely for the TE modes, while remaining strong for the TM modes.

This interference phenomenon affects not only the resonance Q-values, but also their positions. Resonance peaks are pulled away from their homogeneous-fiber locations towards the nearest interference maximum, in a manner analogous to the frequency-pulling of atomic resonances by an external cavity. However, this mode-pulling shifts peak positions by at most a halfwidth from their homogeneous-fiber values. It is thus only significant experimentally for comparitively broad ($Q < 10^5$) resonances. Although not mentioned in the text, the two effects of interference of the core and the coating, i.e. the mode pulling and the modulation of the resonance widths, appear to be visible in figure 8 of the paper by Hightower and Richardson on resonant scattering by a layered sphere [77]. The effect described here has some similarities with the interference enhancement of the internal fields described by Lock [120] for the case when two concentric cavities are coupled together.

Chapter 4

Model for inelastic light scattering from a layered fiber

4.1 Introduction

This thesis concerns the observation of laser emission at frequencies corresponding to cavity modes from a dye-doped solvent flowing in a capillary fiber in the supermicron size range. The modification of the inelastic light scattering characteristics of matter in the presence of a dielectric microparticle can be viewed [33] as being due to an induced polarization field which complements the usual electromagnetic field accompanying electric dipole transitions in atoms or molecules, and which is required to satisfy the boundary conditions at the particle surface. In this chapter this model is extended to give expressions for the external fields inelastically scattered from a single molecule arbitrarily positioned in a normally-illuminated cladded or capillary fiber. Results for a collection of scattering molecules distributed in such a fiber may then be obtained numerically by the incoherent superposition of results from single molecules [90]. These expressions will be useful for the study of fluorescent materials coated on the surface of a fiber [128], or of Raman or fluorescent scattering from a liquid or a gaseous sample flowing in a glass capillary (see e.g. references [81, 70]) and possibly of cladded rare-earth doped glass fibers under investigation for use as fiber-laser amplifiers [147]. We shall use the model to investigate how the modal field

patterns described in chapter 3 affect radiation emitted from a dye-doped solvent flowing in a capillary fiber. Numerical results will be presented demonstrating the spectral characteristics of fluorescence from such a fiber. Due to the computationally intensive nature of these calculations and the wide range of possible parameters to investigate, the results presented have been restricted to showing some of the spectral features directly relevant to this thesis: the predictions of the model regarding e.g. the angular dependence of the fluorescence investigated experimentally by Abromson *et al* [2] and of interest in the development of capillary zone electrophoresis will not be dealt with here.

4.2 Theory of inelastic optical scattering from a molecule in a radially stratified cylinder

We shall model inelastic light-scattering from a molecule embedded in a microparticle as a two-stage process [33]. In the first stage, the molecule is raised to the excited state by the local transmitted field at the incident frequency, the probability of excitation being proportional to the intensity of the transmitted field at the source point. The subsequent de-excitation is accompanied by the usual dipole field as well as by an induced polarization field which is the dielectric response of the particle medium to the dipole field, and which is required to satisfy the boundary conditions at the particle interfaces. The boundary conditions may be used to derive expressions for the external scattered fields. This model has previously been formulated for homogeneous and concentric spheres [33, 32] and for homogeneous cylinders [31]. We now derive expressions for the external fields due to an excited molecule in a layered cylinder. Although we shall later introduce assumptions which restrict the results to scattering in the plane of the normally-incident radiation, yet it is convenient to initially follow closely the more general formulation of Chew *et al* [31]. In what follows it is assumed that the emitting molecule lies within the core of the cylinder; we subsequently quote the corresponding results for the case when the molecule lies within the cladding region. The notation is largely the same as that used by Chew [31] and by Tai [161]: we follow these two works closely.

Assume as in chapter 3 that an infinite circular cladded cylinder lies centred on the z-axis. Denote the outer radius of the cylinder b and the inner radius a, and assign to the core of the cylinder (region 2) and the cladding (region 1) the refractive indices m_2 and m_1 and corresponding propagation constants k_2 and k_1 respectively. Assume that the continuous medium is a vacuum, and that $\mu_0 = \epsilon_0 = 1$. Let the incident plane wave at angular frequency ω_0 propagate along the x-axis with time dependence $\exp(-i\omega_0 t)$. Consider an inelastically scattering molecule at vector coordinate $\underline{r}'$ inside the cylinder core. Let ϕ be the scattering angle in the x-y plane and γ the angle from the (positive) z-axis. Assume that the transmitted field $\underline{E}_{trans}$ at the incident frequency ω_0 (which was referred to in chapter 3 as the internal electric field) excites the molecule to oscillate at the shifted frequency ω with dipole moment $\underline{P}$ given by $\underline{P} = \alpha' \underline{E}_{trans}(\underline{r}')$. The polarizability of the molecule α' is assumed to be isotropic, although this is not intrinsic to the model [124]. Extension of the model to more realistic polarization mechanisms is straightforward, but offers little additional insight. Expressions for the transmitted field $\underline{E}_{trans}$ are a part of the known boundary-value solution for elastic scattering from a normally-illuminated cladded cylinder (see chapter 3). To express the electric field at the shifted frequency in the core region, we use the principle of scattering superposition and write

$$\underline{E}_{core} = \underline{E}_{dip} + \underline{E}_{ind} \tag{4.1}$$

where $\underline{E}_{dip}$ is the dipole field in the absence of boundaries and $\underline{E}_{ind}$ is the induced polarization field due to the presence of the dielectric cylinder. The dipole field at the point $\underline{r}$ in the source-free region in the absence of boundaries due to the dipole source at $\underline{r}'$ may be expressed in terms of the free-space dyadic Green's function

$$\underline{E}_{dip}(\underline{r}) = 4\pi k^2 \tilde{G}_0(\underline{r}, \underline{r}').\underline{P} \tag{4.2}$$

where the dyadic Green's function is given by [161]

$$\tilde{G}_0(\underline{r}, \underline{r}') = \frac{i}{8\pi} \int_{-\infty}^{\infty} dh \sum_{e,o} \sum_{n=0}^{\infty} \frac{2-\delta_{n0}}{\eta^2} [\underline{M}^{(1)}_{\substack{e \\ o} n\eta}(h) \underline{M}'_{\substack{e \\ o} n\eta}(-h) + \underline{N}^{(1)}_{\substack{e \\ o} n\eta}(h) \underline{N}'_{\substack{e \\ o} n\eta}(-h)] \qquad r > r' \tag{4.3}$$

A prime on a vector cylindrical harmonic indicates its evaluation at the source point $\underline{r}'$. This form of the Green's function is appropriate for evaluation of the boundary

conditions at the cylinder surface and at the core/cladding interface while the source point lies within the core region. The vector cylindrical harmonics are given by:

$$\underline{M}_{\substack{e\\o}n\kappa}(h) = \left[\begin{pmatrix} -\sin n\phi \\ \cos n\phi \end{pmatrix} \frac{nZ_n(\kappa\rho)}{\rho}\hat{\rho} - \begin{pmatrix} \cos n\phi \\ \sin n\phi \end{pmatrix} \kappa Z_n'(\kappa\rho)\hat{\phi} \right] \exp(ihz) \quad (4.4)$$

$$\begin{aligned} \underline{N}_{\substack{e\\o}n\kappa}(h) \;=\; & \left[\begin{pmatrix} \cos n\phi \\ \sin n\phi \end{pmatrix} ih\kappa Z_n'(\kappa\rho)\hat{\rho} + \begin{pmatrix} -\sin n\phi \\ \cos n\phi \end{pmatrix} \frac{ihn}{\rho} Z_n(\kappa\rho)\hat{\phi} \right. \\ & \left. + \begin{pmatrix} \cos n\phi \\ \sin n\phi \end{pmatrix} \kappa^2 Z_n(\kappa\rho)\hat{z} \right] \frac{\exp(ihz)}{k_\kappa} \end{aligned} \quad (4.5)$$

where $h = -k\cos\gamma$, κ^2 is chosen to be one of

$$\eta^2 = k_2^2 - h^2$$

$$\tau^2 = k_1^2 - h^2$$

$$\zeta^2 = k^2 - h^2$$

in order to satisfy the Dirichlet boundary conditions at $\rho = a$ and $\rho = b$ and $Z_n(\kappa\rho)$ is the appropriate Bessel function, being $J_n(\kappa\rho)$ unless $H_n^{(1)}(\kappa\rho)$ is indicated by the use of a superscript (1) on the cylindrical harmonic function. The $\begin{matrix} e \\ o \end{matrix} n$ notation indicates the trigonometrical function to be used with the even,odd values of n.

Following Chew *et al*, we substitute 4.3 into 4.2 to get

$$\underline{E}_{dip} = \frac{ik^2}{2}\int_{-\infty}^{\infty} dh \sum_{e,o}\sum_{n=0}^{\infty} \frac{2-\delta_{n0}}{\eta^2}[\alpha_{\substack{e\\o}n}\underline{M}^{(1)}_{\substack{e\\o}n\eta}(h) + \beta_{\substack{e\\o}n}\underline{N}^{(1)}_{\substack{e\\o}n\eta}(h)] \quad (4.6)$$

where $\alpha_{\substack{e\\o}n} = \underline{P}.\underline{M}'_{\substack{e\\o}n\eta}(-h)$ and $\beta_{\substack{e\\o}n} = \underline{P}.\underline{N}'_{\substack{e\\o}n\eta}(-h)$ are the dipole expansion coefficients for a dipole located at the source point. Assume that the induced field at the shifted frequency in the cylinder core due to the presence of the cylinder may be expanded in a similar fashion with unknown coefficients

$$\underline{E}_{ind} = \frac{ik^2}{2}\int_{-\infty}^{\infty} dh \sum_{e,o}\sum_{n=0}^{\infty} \frac{2-\delta_{n0}}{\eta^2}[a_{\substack{e\\o}n}\underline{M}_{\substack{e\\o}n\eta} + b_{\substack{e\\o}n}\underline{N}_{\substack{e\\o}n\eta}] \quad (4.7)$$

where $a_{\substack{e\\o}n}$ and $b_{\substack{e\\o}n}$ are to be determined from the boundary conditions, and the functions J_n are the appropriate Bessel functions to be used in the vector harmonics.

(Note that equations 4.7 and 4.9 appear incorrectly in the paper by Chew *et al* [31].) The field in the cladding of the cylinder, region 1, may be written

$$\underline{E}_1 = \frac{ik^2}{2}\int_{-\infty}^{\infty} dh \sum_{e,o}\sum_{n=0}^{\infty}\frac{2-\delta_{n0}}{\tau^2} \quad [d^1_{\substack{e\\o}n}\underline{M}_{\substack{e\\o}n\tau} + d^2_{\substack{e\\o}n}\underline{M}^{(1)}_{\substack{e\\o}n\tau} + e^1_{\substack{e\\o}n}\underline{N}_{\substack{e\\o}n\tau} + e^2_{\substack{e\\o}n}\underline{N}^{(1)}_{\substack{e\\o}n\tau}] \tag{4.8}$$

where harmonic functions containing both J_n and $H_n^{(1)}$ are needed in the expansion, as region 1 contains no singular points.

In region 0, the externally scattered field is written

$$\underline{E}_0 = \frac{ik^2}{2}\int_{-\infty}^{\infty} dh \sum_{e,o}\sum_{n=0}^{\infty}\frac{2-\delta_{n0}}{\zeta^2}[A_{\substack{e\\o}n}\underline{M}^{(1)}_{\substack{e\\o}n\zeta} + B_{\substack{e\\o}n}\underline{N}^{(1)}_{\substack{e\\o}n\zeta}] \tag{4.9}$$

where $H_n^{(1)}$ has been chosen as the Bessel function in order to satisfy the radiation condition at infinity.

The magnetic fields in the three regions are obtained from the corresponding electric fields by the use of

$$\nabla \times \underline{E} = i\mu\underline{H}$$

Since $\nabla \times \underline{M}^{(1)}_{\substack{e\\o}n\zeta} = k\underline{N}^{(1)}_{\substack{e\\o}n\zeta}$ and $\nabla \times \underline{N}^{(1)}_{\substack{e\\o}n\zeta} = k\underline{M}^{(1)}_{\substack{e\\o}n\zeta}$ etc. we get

$$\underline{H}_{dip} = \frac{kk_2}{2/mu_2}\int_{-\infty}^{\infty} dh \sum_{e,o}\sum_{n=0}^{\infty}\frac{2-\delta_{n0}}{\eta^2}[\alpha_{\substack{e\\o}n}\underline{N}^{(1)}_{\substack{e\\o}n\eta}(h) + \beta_{\substack{e\\o}n}\underline{M}^{(1)}_{\substack{e\\o}n\eta}(h)] \tag{4.10}$$

$$\underline{H}_{ind} = \frac{kk_2}{2\mu_2}\int_{-\infty}^{\infty} dh \sum_{e,o}\sum_{n=0}^{\infty}\frac{2-\delta_{n0}}{\eta^2}[a_{\substack{e\\o}n}\underline{N}_{\substack{e\\o}n\eta} + b_{\substack{e\\o}n}\underline{M}_{\substack{e\\o}n\eta}] \tag{4.11}$$

$$\underline{H}_1 = \frac{kk_1}{2\mu_1}\int_{-\infty}^{\infty} dh \sum_{e,o}\sum_{n=0}^{\infty}\frac{2-\delta_{n0}}{\tau^2} \quad [d^1_{\substack{e\\o}n}\underline{N}_{\substack{e\\o}n\tau} + d^2_{\substack{e\\o}n}\underline{N}^{(1)}_{\substack{e\\o}n\tau} + e^1_{\substack{e\\o}n}\underline{M}_{\substack{e\\o}n\tau} + e^2_{\substack{e\\o}n}\underline{M}^{(1)}_{\substack{e\\o}n\tau}] \tag{4.12}$$

$$\underline{H}_0 = \frac{k^2}{2}\int_{-\infty}^{\infty} dh \sum_{e,o}\sum_{n=0}^{\infty}\frac{2-\delta_{n0}}{\zeta^2}[A_{\substack{e\\o}n}\underline{N}^{(1)}_{\substack{e\\o}n\zeta} + B_{\substack{e\\o}n}\underline{M}^{(1)}_{\substack{e\\o}n\zeta}] \tag{4.13}$$

for the magnetic fields in the three regions. To satisfy the boundary conditions, we need to match the tangential components of $\underline{E}$ and $\underline{H}$ at the radii $\rho = a$ and $\rho = b$. This leads to two sets of eight equations in the sixteen unknown coefficients, (given on page 76 in matrix form) which can then be solved to give expressions for the four external-field coefficients which are of interest here.

$$
\begin{pmatrix}
\frac{1}{\zeta}H_n^{(1)\prime}(\zeta b) & -\frac{ihn}{kb\zeta^2}H_n^{(1)}(\zeta b) & -\frac{1}{\tau}J_n'(\tau b) & -\frac{1}{\tau}H_n^{(1)\prime}(\tau b) & \frac{ihn}{k_1b\tau^2}J_n(\tau b) & \frac{ihn}{k_1b\tau^2}H_n^{(1)}(\tau b) & 0 & 0 \\
\frac{1}{\zeta^2}\frac{ihn}{b}H_n^{(1)}(\zeta b) & \frac{1}{\zeta}kH_n^{(1)\prime}(\zeta b) & -\frac{ihn}{\mu_1\tau^2b}J_n(\tau b) & -\frac{ihn}{\mu_1\tau^2b}H_n^{(1)}(\tau b) & -\frac{k_1}{\mu_1\tau}J_n'(\tau b) & -\frac{k_1}{\mu_1\tau}H_n^{(1)\prime}(\tau b) & 0 & 0 \\
0 & \frac{1}{k}H_n^{(1)}(\zeta b) & 0 & 0 & -\frac{1}{k_1}J_n(\tau b) & -\frac{1}{k_1}H_n^{(1)}(\tau b) & 0 & 0 \\
H_n^{(1)}(\zeta b) & 0 & -\frac{1}{\mu_1}J_n(\tau b) & -\frac{1}{\mu_1}H_n^{(1)}(\tau b) & 0 & 0 & 0 & 0 \\
0 & 0 & \frac{ihn}{\mu_1a\tau^2}J_n(\tau a) & \frac{ihn}{\mu_1a\tau^2}H_n^{(1)}(\tau a) & \frac{k_1}{\mu_1\tau}J_n'(\tau a) & \frac{k_1}{\mu_1\tau}H_n^{(1)\prime}(\tau a) & -\frac{ihn}{\mu_2a\eta^2}J_n(\eta a) & -\frac{k_2}{\mu_2\eta}J_n'(\eta a) \\
0 & 0 & \frac{1}{\tau}J_n'(\tau a) & \frac{1}{\tau}H_n^{(1)\prime}(\tau a) & -\frac{ihn}{k_1\tau^2a}J_n(\tau a) & -\frac{ihn}{k_1\tau^2a}H_n^{(1)}(\tau a) & -\frac{1}{\eta}J_n'(\eta a) & \frac{ihn}{k_2\eta^2a}J_n(\eta a) \\
0 & 0 & 0 & 0 & \frac{1}{k_1}J_n(\tau a) & \frac{1}{k_1}H_n^{(1)}(\tau a) & 0 & -\frac{1}{k_2}J_n(\eta a) \\
0 & 0 & \frac{1}{\mu_1}J_n(\tau a) & \frac{1}{\mu_1}H_n^{(1)}(\tau a) & 0 & 0 & -\frac{1}{\mu_2}J_n(\eta a) & 0
\end{pmatrix}
\begin{pmatrix}
A_{en} \\ B_{on} \\ d^1_{en} \\ d^2_{en} \\ e^1_{on} \\ e^2_{on} \\ a_{en} \\ b_{on}
\end{pmatrix}
$$

$$
= \begin{pmatrix}
0 \\ 0 \\ 0 \\ 0 \\
\frac{ihn}{\mu_2a\eta^2}\alpha_{en}H_n^{(1)}(\eta a) + \frac{k_2}{\mu_2\eta}\beta_{on}H_n^{(1)\prime}(\eta a) \\
\frac{1}{\eta}\alpha_{en}H_n^{(1)\prime}(\eta a) - \frac{ihn}{k_2a\eta^2}\beta_{on}H_n^{(1)}(\eta a) \\
\frac{\beta_{en}}{k_2}H_n^{(1)}(\eta a) \\
\frac{\alpha_{en}}{\mu_2}H_n^{(1)}(\eta a)
\end{pmatrix}
$$

$$
\begin{pmatrix}
\frac{1}{\zeta}H_n^{(1)\prime}(\zeta b) & +\frac{ihn}{kb\zeta^2}H_n^{(1)}(\zeta b) & -\frac{1}{\tau}J_n'(\tau b) & -\frac{1}{\tau}H_n^{(1)\prime}(\tau b) & -\frac{ihn}{k_1b\tau^2}J_n(\tau b) & -\frac{ihn}{k_1b\tau^2}H_n^{(1)}(\tau b) & 0 & 0 \\
-\frac{1}{\zeta^2}\frac{ihn}{b}H_n^{(1)}(\zeta b) & \frac{1}{\zeta}kH_n^{(1)\prime}(\zeta b) & \frac{ihn}{\mu_1\tau^2b}J_n(\tau b) & +\frac{ihn}{\mu_1\tau^2b}H_n^{(1)}(\tau b) & -\frac{k_1}{\mu_1\tau}J_n'(\tau b) & -\frac{k_1}{\mu_1\tau}H_n^{(1)\prime}(\tau b) & 0 & 0 \\
0 & \frac{1}{k}H_n^{(1)}(\zeta b) & 0 & 0 & -\frac{1}{k_1}J_n(\tau b) & -\frac{1}{k_1}H_n^{(1)}(\tau b) & 0 & 0 \\
H_n^{(1)}(\zeta b) & 0 & -\frac{1}{\mu_1}J_n(\tau b) & -\frac{1}{\mu_1}H_n^{(1)}(\tau b) & 0 & 0 & 0 & 0 \\
0 & 0 & \frac{ihn}{\mu_1a\tau^2}J_n(\tau a) & \frac{ihn}{\mu_1a\tau^2}H_n^{(1)}(\tau a) & -\frac{k_1}{\mu_1\tau}J_n'(\tau a) & -\frac{k_1}{\mu_1\tau}H_n^{(1)\prime}(\tau a) & -\frac{ihn}{\mu_2a\eta^2}J_n(\eta a) & \frac{k_2}{\mu_2\eta}J_n'(\eta a) \\
0 & 0 & \frac{1}{\tau}J_n'(\tau a) & \frac{1}{\tau}H_n^{(1)\prime}(\tau a) & \frac{ihn}{k_1\tau^2a}J_n(\tau a) & \frac{ihn}{k_1\tau^2a}H_n^{(1)}(\tau a) & -\frac{1}{\eta}J_n'(\eta a) & -\frac{ihn}{k_2\eta^2a}J_n(\eta a) \\
0 & 0 & 0 & 0 & \frac{1}{k_1}J_n(\tau a) & \frac{1}{k_1}H_n^{(1)}(\tau a) & 0 & -\frac{1}{k_2}J_n(\eta a) \\
0 & 0 & \frac{1}{\mu_1}J_n(\tau a) & \frac{1}{\mu_1}H_n^{(1)}(\tau a) & 0 & 0 & -\frac{1}{\mu_2}J_n(\eta a) & 0
\end{pmatrix}
\begin{pmatrix}
A_{on} \\ B_{en} \\ d^1_{on} \\ d^2_{on} \\ e^1_{en} \\ e^2_{en} \\ a_{on} \\ b_{en}
\end{pmatrix}
$$

$$
= \begin{pmatrix}
0 \\ 0 \\ 0 \\ 0 \\
\frac{ihn}{\mu_2a\eta^2}\alpha_{on}H_n^{(1)}(\eta a) - \frac{k_2}{\mu_2\eta}\beta_{en}H_n^{(1)\prime}(\eta a) \\
\frac{1}{\eta}\alpha_{on}H_n^{(1)\prime}(\eta a) + \frac{ihn}{k_2a\eta^2}\beta_{en}H_n^{(1)}(\eta a) \\
\frac{\beta_{en}}{k_2}H_n^{(1)}(\eta a) \\
\frac{\alpha_{en}}{\mu_2}H_n^{(1)}(\eta a)
\end{pmatrix}
$$

We now introduce the assumption that, instead of a single oscillating dipole, we have an infinite line source of coherently emitting dipoles, defined for all z by the coordinates (ρ', ϕ'), which is excited by the normally-incident wave. In this case, the scattered field must approach an outgoing cylindrical wave at large distances: effectively, only terms with $h = 0$ will be observed in the scattering plane. By the use of the appropriate asymptotic approximation, the scattered field equation 4.9 may then be reduced to

$$\underline{E}_0 \rightarrow \frac{2\pi k \exp(ik\rho)}{(2\pi i\rho)^{\frac{1}{2}}} \sum_{n=0}^{\infty} i^{-n}(2-\delta_{n0}) \quad \left[\left(A_{en}\hat{\phi} + iB_{en}\hat{z}\right)\cos n\phi + \left(A_{on}\hat{\phi} + iB_{on}\hat{z}\right)\sin n\phi\right] \qquad (4.14)$$

which is a particularly simple expression. A similar result may be obtained in the far field by the application of a saddle-point integration; the details are given in reference [161]. The boundary conditions simplify considerably when $h = 0$, with the A_n's and the B_n's uncoupling to give four sets of four equations each. The boundary conditions reduce to

$$\begin{pmatrix} \frac{1}{k}H_n^{(1)\prime}(kb) & -\frac{1}{k_1}J_n'(k_1b) & -\frac{1}{k_1}H_n^{(1)\prime}(k_1b) & \\ H_n^{(1)}(kb) & -\frac{1}{\mu_1}J_n(k_1b) & -\frac{1}{\mu_1}H_n^{(1)}(k_1b) & \\ & \frac{1}{k_1}J_n'(k_1a) & +\frac{1}{k_1}H_n^{(1)\prime}(k_1a) & -\frac{1}{k_2}J_n'(k_2a) \\ & \frac{1}{\mu_1}J_n(k_1a) & +\frac{1}{\mu_1}H_n^{(1)}(k_1a) & -\frac{1}{\mu_2}J_n(k_2a) \end{pmatrix} \begin{pmatrix} A_{\substack{e\\o}n} \\ d^1_{\substack{e\\o}n} \\ d^2_{\substack{e\\o}n} \\ a_{\substack{e\\o}n} \end{pmatrix} = \begin{pmatrix} 0 \\ 0 \\ \frac{\alpha_{\substack{e\\o}n}}{k_2}H_n^{(1)\prime}(k_2a) \\ \frac{\alpha_{\substack{e\\o}n}}{\mu_2}H_n^{(1)}(k_2a) \end{pmatrix} \qquad (4.15)$$

for the TE case and

$$\begin{pmatrix} H_n^{(1)\prime}(kb) & -\frac{1}{\mu_1}J_n'(k_1b) & -\frac{1}{\mu_1}H_n^{(1)\prime}(k_1b) & \\ \frac{1}{k}H_n^{(1)}(kb) & -\frac{1}{k_1}J_n(k_1b) & -\frac{1}{k_1}H_n^{(1)}(k_1b) & \\ & \frac{1}{\mu_1}J_n'(k_1a) & +\frac{1}{\mu_1}H_n^{(1)\prime}(k_1a) & -\frac{1}{\mu_2}J_n'(k_2a) \\ & \frac{1}{k_1}J_n(k_1a) & +\frac{1}{k_1}H_n^{(1)}(k_1a) & -\frac{1}{k_2}J_n(k_2a) \end{pmatrix} \begin{pmatrix} B_{\substack{e\\o}n} \\ e^1_{\substack{e\\o}n} \\ e^2_{\substack{e\\o}n} \\ b_{\substack{e\\o}n} \end{pmatrix} = \begin{pmatrix} 0 \\ 0 \\ \frac{\beta_{\substack{e\\o}n}}{\mu_2}H_n^{(1)\prime}(k_2a) \\ \frac{\beta_{\substack{e\\o}n}}{k_2}H_n^{(1)}(k_2a) \end{pmatrix} \qquad (4.16)$$

for the transverse magnetic case, and these may be solved for the four external-field coefficients $A_{\substack{e\\o}n}$ and $B_{\substack{e\\o}n}$ by the application of Kramer's rule. It is worth noting that the determinants of the matrices on the left of the equations 4.15 and 4.16 which constitute the denominators in the expressions for the fluorescence coefficients

are, to within a constant, identical to those obtained in the corresponding elastic-scattering problem. (Compare equations 4.15 and 4.16 to 3.14 and 3.24.) Thus the resonances which occur in the elastic-scattering coefficients and which correspond to the zero-crossings of the denominators of the scattering coefficients occur at the same values in the present solution as well. Upon substitution of $a = b$ and $m_1 = m_2$ and by the use of the Wronskian, these expressions for the boundary conditions may be further reduced and solved to give the corresponding expressions for the homogeneous cylinder fluorescence coefficients, as given by Chew *et al* .

When the excited dipole lies in the cladding region of the cylinder, different expressions result; firstly because the principle of scattering superposition must now be applied to this region rather than the core, and secondly because the expression for the free-space dyadic Green's function needs to be altered for evaluation of the dipole field at the inner boundary, where $r < r'$. The details are given in the book by Tai [161]. The boundary conditions are the same as those given in equations 4.15 and 4.16, but with the right-hand sides replaced by

$$\begin{pmatrix} \frac{1}{k_1}\alpha^{e}_{o n} H_n^{(1)\prime}(k_1 b) \\ \frac{\alpha^{e}_{o n}}{\mu_1} H_n^{(1)}(k_1 b) \\ -\frac{1}{k_1}\alpha^{(1)}_{e_{o n}} J_n'(k_1 a) \\ -\frac{\alpha^{(1)}_{e_{o n}}}{\mu_1} J_n(k_1 a) \end{pmatrix} \tag{4.17}$$

and

$$\begin{pmatrix} \frac{\beta^{e}_{o n}}{\mu_1} H_n^{(1)\prime}(k_1 b) \\ \frac{1}{k_1}\beta^{e}_{o n} H_n^{(1)}(k_1 b) \\ -\frac{\beta^{(1)}_{e_{o n}}}{\mu_1} J_n'(k_1 a) \\ -\frac{1}{k_1}\beta^{(1)}_{e_{o n}} J_n(k_1 a) \end{pmatrix} \tag{4.18}$$

respectively, where $\alpha^{(1)}_{e_{o n}} = \underline{P}.\underline{M}^{(1)}_{e_{o n r}}$ etc. By allowing the core radius to shrink to zero, these equations too may be solved and reduced to those for the homogeneous cylinder.

For incident light polarized either perpendicular to or parallel to the cylinder axis, the expression eqn 4.14 may be used to integrate the fluorescent intensity over all angles in the scattering plane to give the integrated fluorescence, a measure of

the (unnormalized) efficiency of the dipole in the cylinder for fluorescence. We want

$$\int_0^{2\pi} I(\phi)d\phi = \int_0^{2\pi} \underline{E_0}.\underline{E_0^*}d\phi.$$

This involves an integral over a double summation: however, due to the orthogonal properties of the trigonometrical functions, most of the terms give zero. We get, after some additional cancellation,

$$Q_{flu} \propto k^2 \sum_{n=0}^{\infty}(2-\delta_{n0})[|A_{en}|^2 + |A_{on}|^2] \quad \text{TE} \tag{4.19}$$

and

$$Q_{flu} \propto k^2 \sum_{n=0}^{\infty}(2-\delta_{n0})[|B_{en}|^2 + |B_{on}|^2] \quad \text{TM} \tag{4.20}$$

where $B_{o0} = A_{o0} = 0$. This is in a sense a rather artificial result, being based on the unrealizable assumption of an infinite line source of coherently emitting dipoles in the fiber. However it has the advantage of being quick to compute, and it demonstrates the main spectral features of the fluorescence in a general fashion.

4.3 Numerical results

The fluorescence spectra presented here result from the numerical evaluation of equations 4.19 and 4.20 for a large number of inelastically scattering molecules regularly distributed in the cylinder on a rectangular array in the plane perpendicular to the cylinder axis. Because of the assumption of a coherently emitting line source only molecules in the scattering plane ($z = 0$) need be considered. After calculation of the external field for each dipole source these are summed incoherently to represent the fluorescence from the cylinder. The number of dipoles used to calculate the fluorescence at a single wavelength ranged from 2500-10000, depending on the fiber size. This was not always sufficient to reflect every detail of the internal fields but does show the major trends, while keeping the computation time within reasonable limits. These results serve to demonstrate the effect of the modal field patterns described in chapter 3 on light emitted from molecules in a cladded fiber. Evaluation of e.g. equation 4.14 to give values for the fluorescent light scattered at a given angle is as easily achieved, but has no particular relevance to our investigation. The

numerical problems associated with performing the computations are largely those already encountered in the computations of chapter 3, and the methods used there are equally applicable to the present problem. Consequently no detailed explanation of the computations will be given here.

4.3.1 Resonant enhancement of emissions - homogeneous fiber

Initial results presented in this section will demonstrate the spectral features of fluorescence from a homogeneous cylinder using the Chew model; to our knowledge, this has never been investigated numerically. We denote the two polarizations of the incident and scattered light as TM (electric vector parallel to the cylinder axis) and TE (electric vector perpendicular to cylinder axis), corresponding to Chew's I_1 and I_2 respectively. It should be noted that some confusion has arisen in the literature concerning this terminology (compare e.g. Videen *et al* [170] and Owen *et al* [130]); the above choice reflects the historical origins of the terms in waveguide theory [159]. The free-space dipole fields are constant and vary as $\cos^2\theta$ in the scattering plane for these two polarizations respectively. The integrated intensities as functions of the size parameter for a normally-illuminated homogeneous cylinder uniformly filled with fluorescing molecules and with real refractive index $m = 1.5$ have been computed using equations 4.19 and 4.20 and are plotted in figure 4.1. In this and subsequent plots we have normalized the numerical results to those obtained from a single oscillating dipole in free space; consequently the observed deviations from unity are due solely to the presence of the dielectric interfaces. In order to aid the analysis of the curves, we assume initially that the incident and fluorescent wavelengths are identical. The integrated fluorescence intensity for TE illumination (computed numerically using equation 4.19) is on average half that for TM illumination, as a result of the deep minimum near 90° in the angular scattering pattern for TE polarization; however, this is also true for the free-space dipole, and so does not show up in the normalized curves. As $x \to 0$, the intensity of fluorescence per dipole for TE illumination decreases sharply, while that for TM illumination remains relatively constant. A similar effect has been previously noted in calculations of coherent fluorescence from a cylinder [170], and in the incoherent fluorescence at

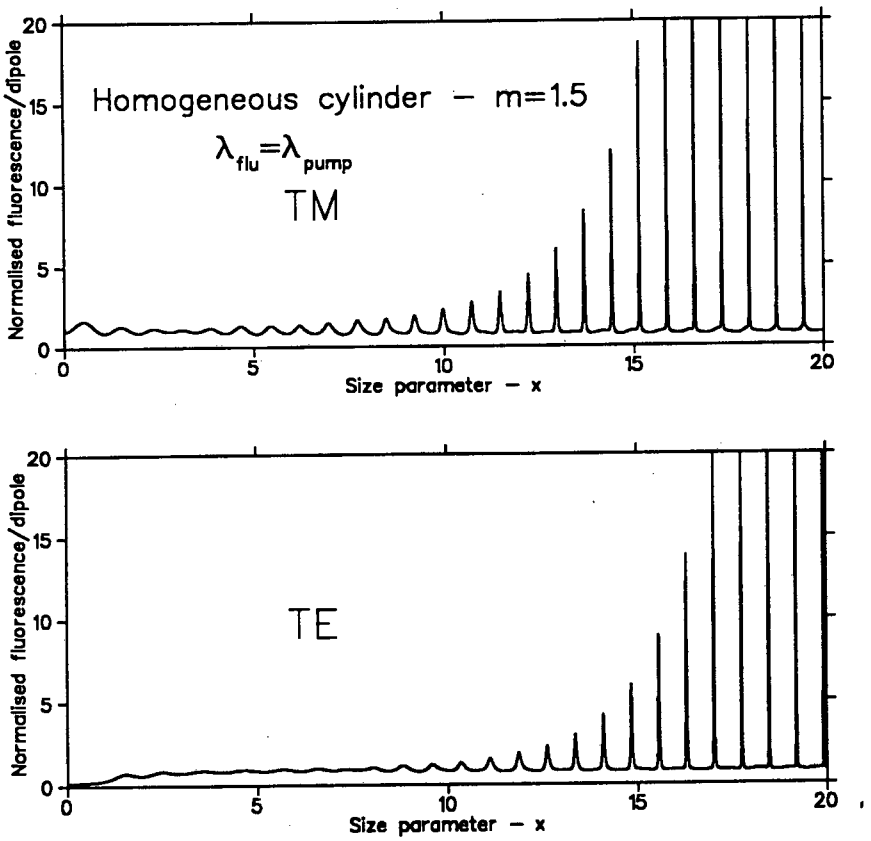

Figure 4.1: Normalized fluorescence/dipole computed for an array of dipoles distributed in an illuminated cylinder for the special case $\lambda_{flu} = \lambda_{pump}$, as a function of the size parameter. For small values of x, the TE fluorescence is substantially less than unity, while for the TM case, the curve oscillates around unity. For large values of the size parameter, the baseline of the curves remains just below one, while large sharp peaks appear at values corresponding to the MDR's.

specific angles [31] . The baseline integrated intensity per dipole remains near unity for larger values of the size parameter, implying a fluorescent signal proportional to the particle volume for a constant concentration of inelastic scatterers. This is in contrast to the coherent fluorescence from a cylinder [170], for which theory predicts the interference of the emissions from different locations in the particle, which can cause a constant or even a decreasing fluorescent signal with increasing size. One of the most striking features of the curves, and of particular interest in this study, is the appearance of sharp peaks in the integrated fluorescence at specific values of the size parameter. These first appear at $x \simeq 10$, and thereafter appear at regular intervals, becoming narrower and higher with increasing size parameter. The values at which these peaks occur correspond to the natural resonant frequencies of the optical cavity formed by the cylinder surface. The internal pump fields $\underline{E}_{trans}$ at these frequencies are greatly enhanced: the emission process is also enhanced at these same frequencies, as is revealed by a study of the fluorescence coefficients. The origin of this enhancement of the emission process is the increase in the transition rate when the emitted photon corresponds to a resonance [29, 30]. Investigation of the fluorescence from an individual molecule variously positioned in the fiber shows that the enhancement is observed only if the molecule is positioned near to the fiber surface; similarly in figure 4.1 the peaks observed in the integrated fluorescence from the fiber are due solely to the contribution from molecules near to the surface. As in the elastic scattering, each peak observed in the spectrum of the emitted light is associated with a resonance in a specific term in the partial wave expansion. The input and output resonances occur at the same values of x in figure 4.1 because we have assumed that the incident and fluorescent light have the same frequencies. Similar calculations are presented in figure 4.2; however, here we have assumed that $\lambda = 1.2\lambda_0$. Each resonance thus occurs twice in figure 4.2, as both an input and an output resonance; naturally, the enhancement in the resonances here is considerably less than in the double resonances of figure 4.1 [35]. The features in the figure are similar to those observed experimentally in the Raman spectrum of an evaporating spherical liquid droplet [153]. Of perhaps greater practical interest in the scattering from a cylinder is the variation in the inelastic scattering from a fiber of fixed size

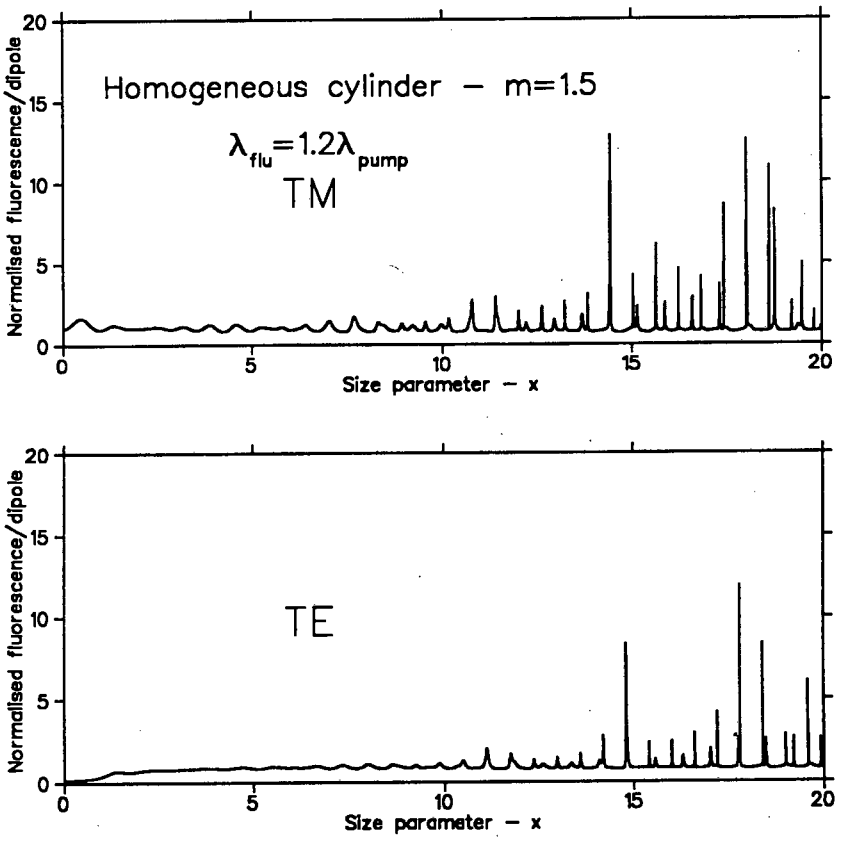

Figure 4.2: The same as the previous figure, but with $\lambda_{flu} = 1.2\lambda_{pump}$. Each resonant mode now causes two peaks in the curves, one an input and one an output resonance, while the peak enhancement of the fluorescence is significantly less than that at the double-resonances of the previous figure. An exception to this is the double resonance which appears for both polarizations just before $x = 15$.

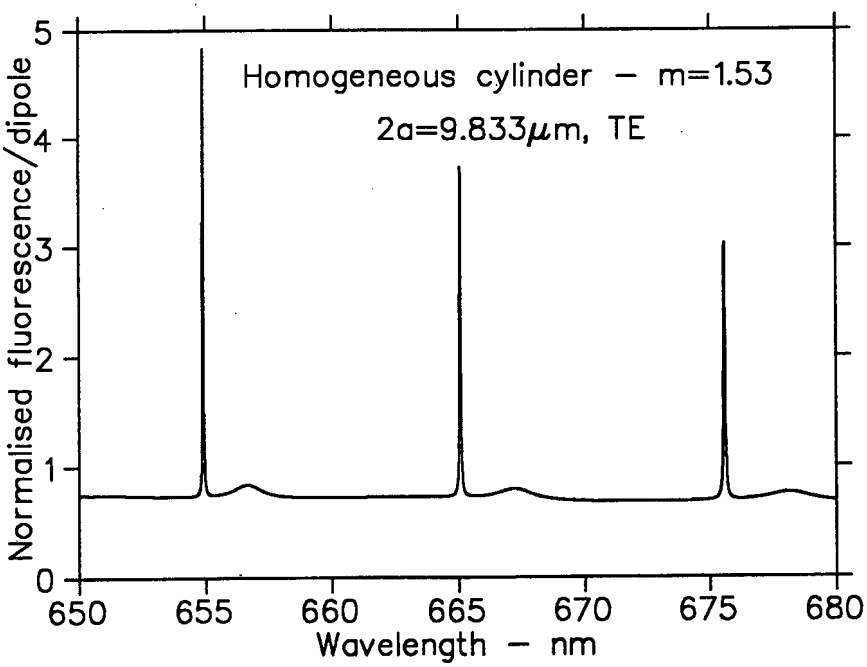

Figure 4.3: Computed fluorescence from a normally-illuminated glass capillary uniformly filled with fluorescing molecules, for comparison with the experimental results of Owen *et al* (see text). The observed peaks are due to the third- and fourth-order modes (as was observed experimentally), enhancement at the narrower modes being the greater.

while either the incident or the shifted wavelength is varied. This corresponds to the fluorescence and excitation spectra which have been observed from coated fibers [128]. An example of such variation is shown in figure 4.3, where we have plotted the computed integrated fluorescence observed from a fiber of diameter $2b = 9.833\mu$m and real refractive index $m = 1.53$ illuminated with light of wavelength $\lambda = 615$nm, corresponding to the fiber studied experimentally by Owen and co-workers (see reference [128], figure 2a). Two major differences between the experimental case and the computations presented in figure 4.3 are firstly that the experiments were performed with a thin layer of dye molecules coated onto the fiber surface whereas the computations have been performed for dipoles evenly distributed through the fiber, and secondly that the computations presented in figure 4.3 result from the approximations made in deriving equations 4.20 and 4.19, while the observed spectra were recorded by illuminating a finite length of fiber and collecting fluorescence

over a finite and well-defined angular range. The computed fluorescence is shown as a function of the wavelength in the range 650-680nm for TE polarization. It should be noted that the peaks visible in figure 4.3 originate in the third- and fourth-order resonances. The considerably greater enhancement due to the narrower, lower-order modes is not seen due to the finite step size used in the computations. These very narrow modes were not observed experimentally either, being broadened beyond recognition by fiber imperfections. Redoing the calculation with the pump frequency tuned to one of the narrow third-order resonances (i.e. simulating the input resonance studied experimentally, not shown in figure) causes a substantial increase in the fluorescence signal (a factor of more than twenty) particularly for the resonance wavelengths. The input resonance fluorescence enhancement arises through the increased values of α and β in equation 4.2. Because of the differences between the experiments and our computations, it is difficult to draw any conclusions from a comparison between this and the approximately three-fold enhancement observed by Owen and colleagues, other than to note that the authors state that the third-order modes were not fully supported in the experiments of Owen *et al* due to fiber imperfections.

4.3.2 Resonant enhancement in a fluorescing-core fiber

We now use the theory derived above to investigate the conditions under which resonant enhancement of emissions may be observed from a fluorescing-core cylinder. This is of interest in the study of inelastic light scattering from a liquid flowing in a capillary fiber. The morphology-dependent resonances in homogeneous cylinders occur as a result of repeated total internal reflection of light from the cylinder surface, which occurs for internal light at near to grazing incidence upon the surface, whether the light is due to an illuminating wave as in elastic scattering or originates within the fiber itself. Resonances occur at wavelengths such that the fields are in phase after one round trip inside the scatterer, interfering constructively. Resonant enhancement of the emissions from a fluorescing-core fiber will be observed if enhanced fields occur in the core region containing the inelastically-scattering molecules, whether these are resonances of the cladding or of the core. Core resonances may have only

a small effect on the elastic-scattering characteristics of the cylinder; however, as we will show, they can be the dominant feature of the inelastic scattering from a fluorescing-core cylinder. We will first demonstrate the conditions under which cladding resonances may enhance emissions from a fluorescing-core cylinder, and then give an example showing core resonances.

Cladding resonances will result in enhanced emissions from molecules in the core region if the cladding is relatively thin. In this case enhanced resonant fields at the pump frequency will extend into the core region containing the inelastically scattering molecules (see figure 3.13), and also the frequency-shifted radiation will be coupled into output resonances. A numerical example of this fluorescence is shown in figure 4.4, calculated for dye-doped benzyl alcohol ($m_2 = 1.539$) flowing in a glass ($m_1 = 1.5$) capillary of size parameter $x \simeq 50$ and with core/cladding ratios $a/b = 0.8$ and $a/b = 0.6$, and illuminated with light corresponding to size parameter $x = 57.54$, which does not correspond to an input resonance in either case. The enhanced fluorescence due to MDR's is completely absent from the lower curve corresponding to the smaller core diameter. Light originating in this smaller core is incident upon the external surface at too small an angle for total internal reflection, and is thus not coupled into the whispering-gallery modes. Consequently the increased density of photon states at resonance which results in the enhanced transition rates associated with MDR peaks is not accessible to a radiating molecule in the fiber core. The larger core diameter in figure 4.4 (upper plot) shows resonance-enhanced fluorescence, with the peak enhancement being a factor of about 5 for the third-order modes. Narrower modes not shown in the plot result in substantially greater enhancement. Resonant modal field patterns for several of these cases are given in figure 3.13.

For an intermediate value of a/b, resonance enhancement of fluorescence is greater if the core refractive index greater than that of the cladding, as may be anticipated from figure 3.14. Fluorescence spectra corresponding to the two cases illustrated in that figure are shown in figure 4.5. Substantial resonance enhancement of the fluorescence is observed from the fiber if the core material has a high refractive index (corresponding in this case to benzyl alcohol) whereas if ethanol is used as the

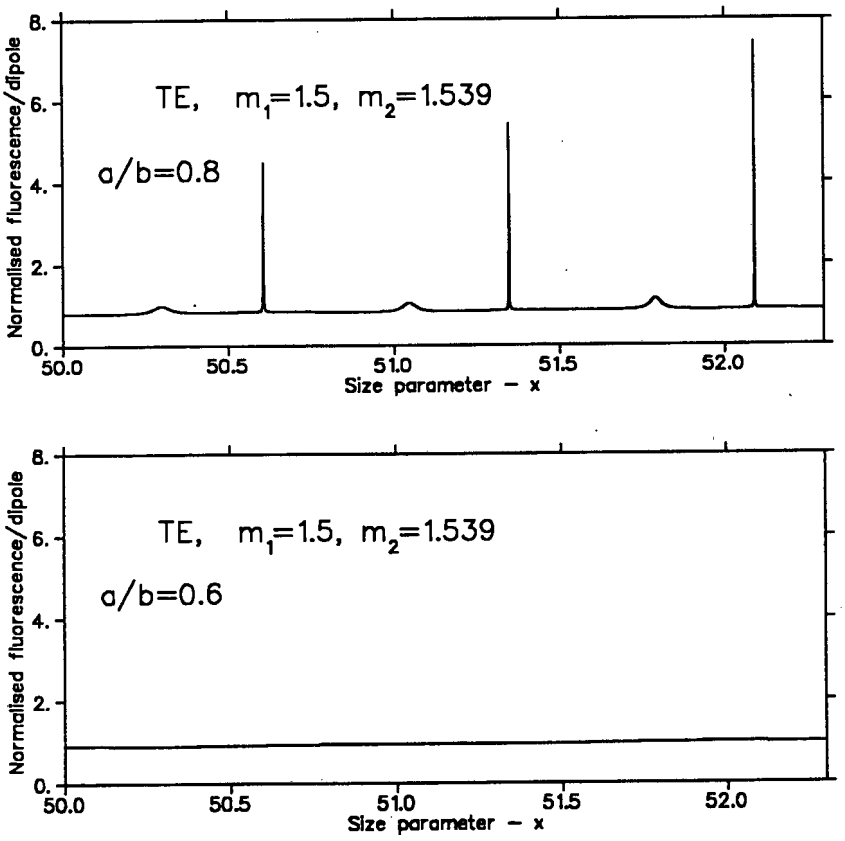

Figure 4.4: Computed TE fluorescence from dye doped benzyl alcohol flowing in a capillary fiber ($m_1 = 1.5$) of diameter ratio $a/b = 0.8$ (upper plot) and $a/b = 0.6$, as a function of the size parameter. The peaks in the upper plot correspond to third and fourth order modes; the resonances of the $a/b = 0.6$ fiber do not noticably affect the fluorescence from the fiber core.

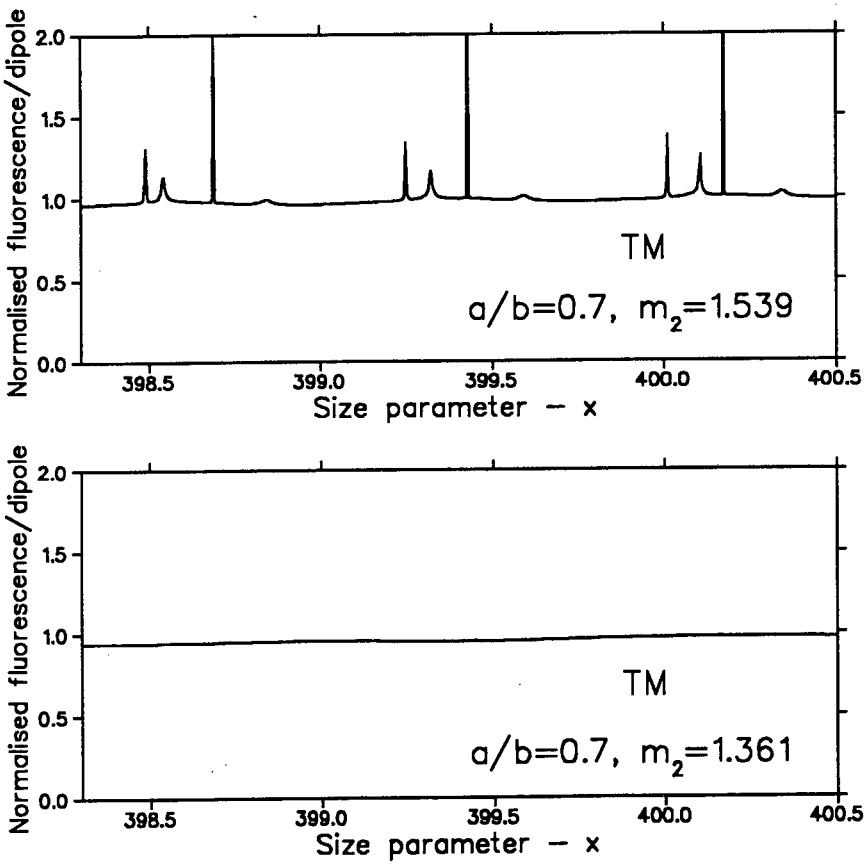

Figure 4.5: Fluorescence spectra for a fiber with parameters $a/b = 0.7$, $m_1 = 1.5$, and $m_2 = 1.539$ (upper curve) and $m_2 = 1.361$, corresponding to ethanol- and benzyl alcohol-core capillaries. Substantial resonant enhancement of fluorescence occurs for the benzyl alcohol core, while virtually none occurs for the ethanol-core fiber. It should be noted that the observed peaks do not correspond to resonances of the core alone, the cavities formed by the two interfaces being in this case strongly coupled together.

core material, no resonant peaks are observed.

Core resonances exist independently of the cladding for large fibers if $m_2 > m_1$, and if $a < b/m_1$ (see chapter 3). In this case the cladding resonances have no effect on the fluorescence from the fiber core, while the core resonances result in substantial resonance enhancement. We illustrate this with figure 4.6, being the computed fluorescence spectra for a fiber with parameters $a = 25\mu m$, $b = 63\mu m$, $m_2 = 1.626$ and $m_1 = 1.458$. The computed TM extinction efficiency for this fiber was given in figure 3.15: peaks due to both core and cladding resonances are visible in that curve. Modal field patterns corresponding to several of these resonances were shown in figures 3.16–3.18. The computed fluorescence spectra (figure 4.6) show regular series of resonant peaks, corresponding to the core resonances. The very narrow $l = 1$ modes are not visible in the plots, due to the finite step size used in the computation: the $l = 2$ peaks cause a greater than 2–fold enhancement of the fluorescence, and the $l = 3$ modes cause the smaller narrow peaks. The modulation of the resonance Q-values (due to the interference effect of page 68) is seen to cause a modulation of the strengths of the resonance peaks in the TM fluorescence (visible here for the $l = 3$ modes).

4.4 Conclusions

We have used the model of Chew *et al* for inelastic light scattering from molecules embedded in fine particles to study incoherent fluorescence from large homogeneous and layered fibers. Although this was not discussed in the original papers, the model incorporates the effects of the high-Q resonances which occur at specific values of the size parameter, and which have been extensively studied experimentally in both the elastic and the inelastic scattering. We have performed a numerical study of the effect of these resonances on the inelastic spectral scattering from a normally-illuminated homogeneous fiber. The model previously formulated for homogeneous fibers has been extended to allow for the presence of a layer of different refractive index on the fiber. The extended formulation of the model has been used to investigate the conditions under which resonances due to the cavities formed by the core and

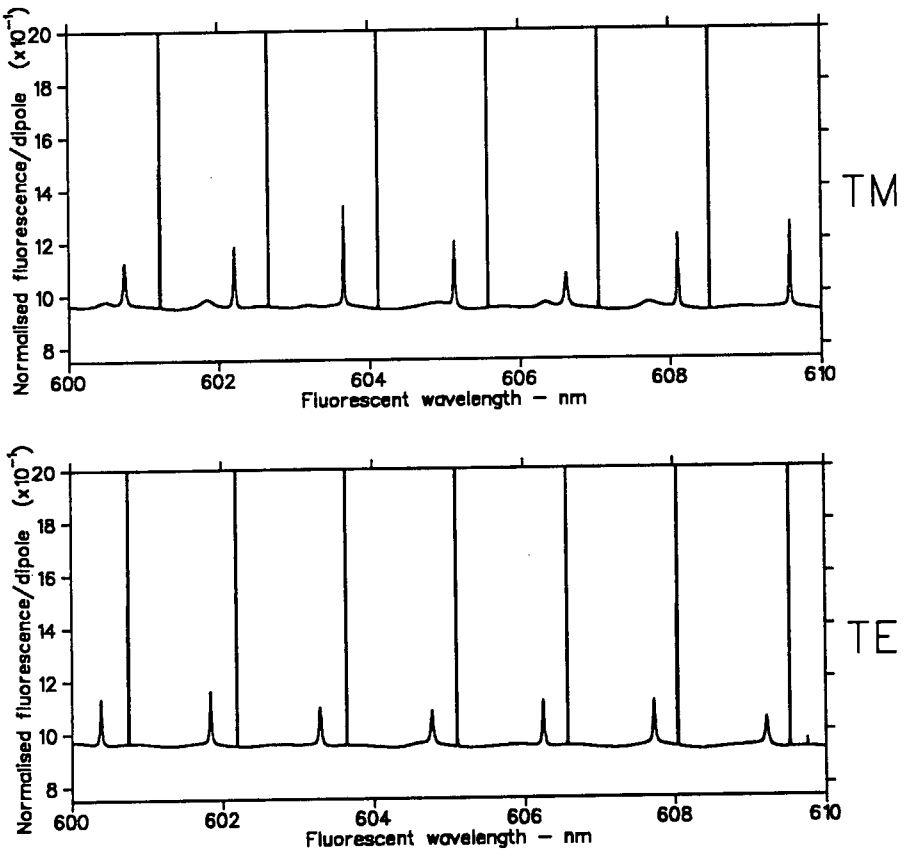

Figure 4.6: Computed fluorescence spectrum for dye-doped quinoline ($m_2 = 1.626$) flowing in a fused-silica ($m_1 = 1.458$) capillary of size $a = 25\mu$m and $b = 60\mu$m. The observed peaks are due to second and third order modes. The modulation of the fluorescent peak heights due to the interference effect is visible in the TM fluorescence.

cladding surfaces will be observed in the inelastic scattering from a fluorescing-core fiber. We find that the model predicts that optical emissions from the core of a capillary fiber should show peaks corresponding to morphology-dependent resonances when the resonant modal field patterns exhibit enhancement extending into the core region, whether these are resonances of the core or of the cladding, as might be intuitively expected. Under these circumstances emissions from excited dye molecules in the fiber core are coupled to the whispering-gallery-mode resonances. It can be anticipated that these conclusions will hold for stimulated as well as for spontaneous transitions in excited molecules.

Chapter 5

A capillary-fiber whispering-gallery-mode laser: experiments, results and discussion

5.1 Equipment

Our experiments were performed using a frequency-doubled beam from a single-longitudinal-mode Nd:YAG laser. This instrument is part of a SOPRA-Quantel coherent anti-Stokes Raman spectroscopy (CARS) laser table. The oscillator consists of a cavity of optical path length approximately 1.1m with two etalons and an Nd:YAG rod as the active laser material. The water-cooled Nd:YAG crystals in the oscillator and two amplifiers are pumped by flashlamps. The cavity is passively Q-switched using a BDN saturable absorber cell, resulting in a single 14ns pulse at the Nd:YAG wavelength 1064nm. This pulse is passed through the two amplifying rods before being frequency-doubled in a KDP crystal (with 30% efficiency). This results in a 14ns green ($\lambda = 532$nm) pulse of energy up to 100mJ. For the purposes of our experiments, the laser was run at one of two calibrated settings; 0.3mJ/pulse or 0.006mJ/pulse (this latter setting corresponds to the use of the Nd:YAG oscillator

only); intermediate and lower pump energies were obtained by the use of neutral density filters. The laser is designed to fire at 1, 5, or 10 Hz: our experiments were performed at repetition rates of 1 or 5 Hz. The 4×6mm green beam is polarized with electric vector horizontal when it leaves the laser table, this was rotated when required by the use of a $\lambda/2$ plate.

The green beam was focussed using a 300mm focussing lens and the fiber under study was placed some 260mm from the lens, on the spectrometer axis. This enabled the illumination of a relatively short ($<$ 1mm) length of fiber with a beam of nearly uniform cross-section, ensuring the validity of the plane-wave approximation to calculate the internal fields at the pump frequency. The length of fiber under study was glued into a hole in a brass reservoir which held the dye-doped solvent; another hole in the reservoir was connected to a pressurized nitrogen supply. The reservoir was then mounted vertically on a goniometer with the free end of the fiber pointing downwards, the goniometer allowed translation of the fiber along three mutually perpendicular axes, and rotation about two orthogonal axes in the optical plane. The pressurized nitrogen ensured a steady flow of the solvent through the fiber, the flow speed being of the order of several millimetres per second depending on the capillary core size.

Spectral characteristics of the laser emission from the fiber were studied using a 0.75m spectrometer and a 1024-channel optical multichannel analyzer (OMA) (EG&G PARC 1421 detector and 1461 controller). A schematic diagram of the experimental arrangement is shown in figure 5.1. The illuminated portion of the fiber was imaged 2:1 onto the entrance slit of the spectrometer. Light passing through the slit was dispersed using a concave holographic grating with 2100 lines/mm, and brought to a focus on the OMA. The spectrometer was calibrated using known atomic emission lines from Na, Hg and Ne lamps. The total spectral range covered for a given spectrometer setting was just less than 6nm - consequently, to record a complete spectrum from a lasing fiber which may cover up to 30nm under certain conditions requires recording data at several different wavelength settings and subsequently joining the spectra to one another. The output of the OMA was monitored in real time using an oscilloscope while data acquisition was performed under the

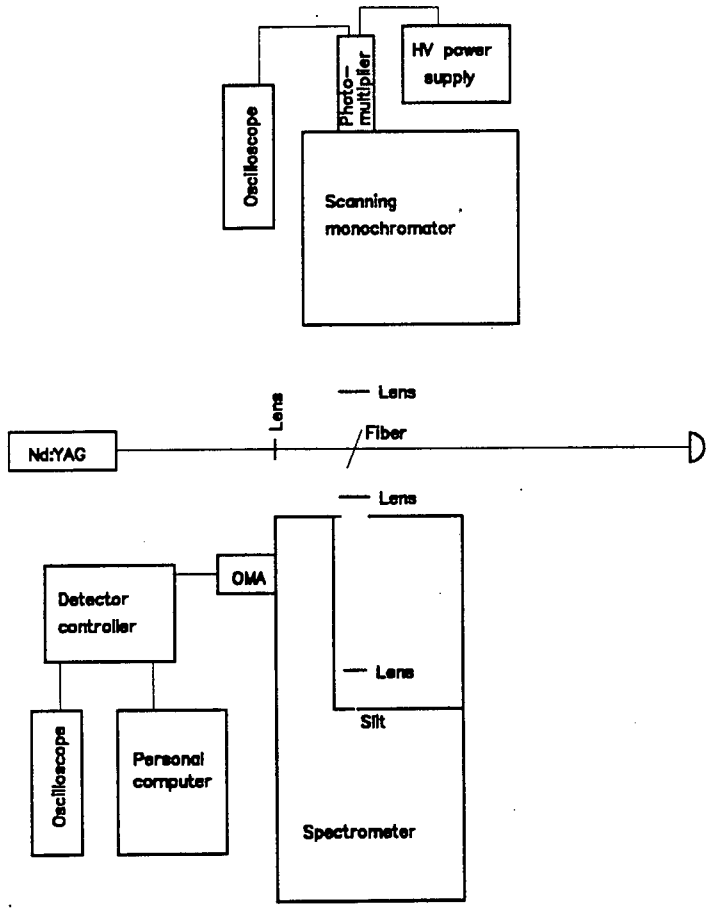

Figure 5.1: A schematic diagram of the experiments described in this chapter. The monochromator and photomultiplier were used to study the time-dependence of the laser emissions from the fiber.

control of a computer with an i-286 processor. The microcomputer was connected via a GPIB interface to the detector controller: this would send TTL pulses to the laser control unit to fire the flashlamp capacitor banks, and synchronously acquire data from the OMA. The detector integrated the signal for 16 milliseconds for each spectrum, during which time the laser would fire once. The observed spectrum thus corresponds to the time-integrated output of a single pulse from the fiber. The spectra were stored on the microcomputer hard disk for later transfer to a faster computer (386-based microcomputer, VAX 6000-330 or MicroVAX 3100-90). The monochromator (Heath EU700) and photomultiplier tube (RCA C7151 W – 2.7ns risetime) were used to study the time dependence of the laser emissions at different wavelengths.

Two sets of capillary fibers were studied in our experiments. Preliminary experiments into the feasibility of studying whispering-gallery-mode laser emission in a cylindrical geometry by using dye-doped solvent flowing in a capillary fiber were performed in 1990 using Crown glass capillaries pulled in our own laboratories. The refractive index of this material was measured at the helium-neon laser wavelength (632.8nm) by the immersion method to be 1.495. These fibers had thin walls, with the inner diameter/outer diameter ratio $a/b \sim 0.5 - 0.8$. However, due to variations in the pulling procedure they were not accurately reproducible, and were rather sharply tapered. The main experiments were performed using fused-silica capillaries of various sizes given in table 5.1, and purchased commercially from Polymicro Technologies, Phoenix, Arizona. Table 5.1 also shows the manufacturers tolerances on the inner diameter measurements for these fibers. The refractive index was given by the manufacturer as $n_D^{20} = 1.458$, in agreement with the accepted value for fused silica.

5.2 Preliminary experiments on lasing cylinders

Our initial experimental investigations into whispering-gallery-mode laser emission from dye-doped solvent flowing in a capillary fiber were performed using dye-doped solvent flowing in thin-walled fibers pulled in our laboratories. The intention was

Product #	Nominal core size $2a(\mu m)$	External size $2b(\mu m)$
TSP015/150	15 ± 3	125
TSP020/150	20 ± 3	124
TSP025/150	25 ± 3	117
TSP030/150	30 ± 3	128
TSP040/150	40 ± 3	130
TSP050/150	50 ± 3	128
TSP050/192	50 ± 3	166
TSP050/375	50 ± 3	333
TSP050/530	50 ± 3	490
TSP075/150	75 ± 3	125

Table 5.1: Manufacturers specified core sizes and measured external sizes for the capillary fibers used in the experiments. The product codes refer to the fibers covered with a protective coating, which was not applied in our case.

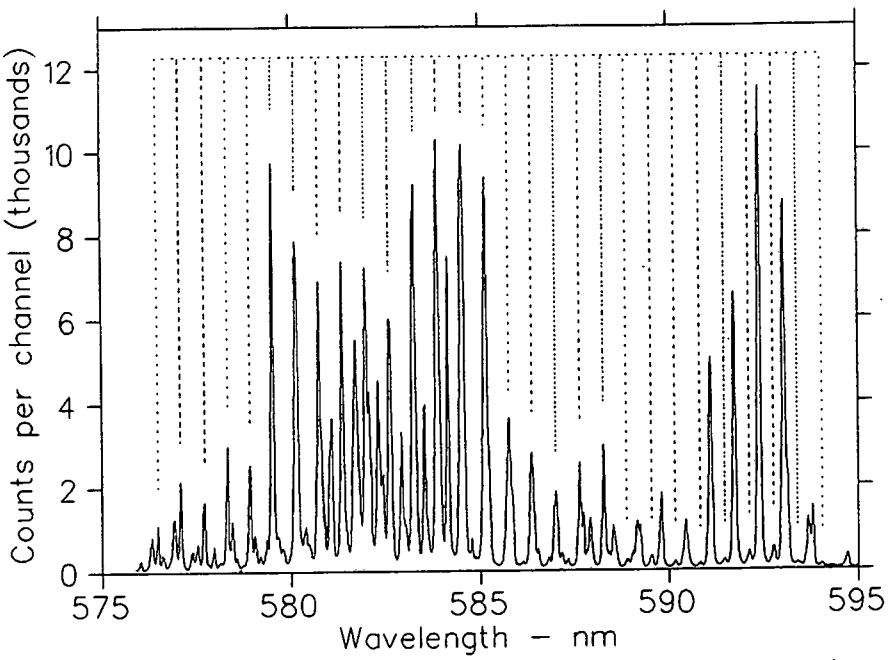

Figure 5.2: Laser spectrum observed from dye-doped benzyl alcohol flowing in a fiber of nominal parameters $a/b \simeq 0.71$,$b = 61\mu$m,.

to study the resonant modes formed in the composite-fiber cavity by reducing the capillary wall thickness until the laser dye in the core region of the fiber overlapped significantly with the resonance-enhanced internal fields near to the fiber surface. The experimental results obtained proved difficult to analyze conclusively due to the lack of reproducibility and substantial taper in the fiber size. Consequently we shall describe the experiments only briefly, and present only a few illustrative results.

The solvents used in the experiments were ethanol ($m = 1.361$) and benzyl alcohol ($m = 1.539$), and these were doped with the laser dye rhodamine 6G at a concentration of $10^{-4}M$. These two were also mixed together in different proportions to obtain a solvent of intermediate refractive index when required. An example of an observed laser spectrum is shown in figure 5.2, which was recorded from dye-doped benzyl alcohol flowing in a fiber with $b \simeq 61\mu$m and $a/b \simeq 0.7$. (These values were obtained by studying the fiber cross-section using an optical microscope after the experiment.) The mode spacing is in approximate agreement with the value computed using the boundary-value formalism: a precise comparison was not attempted, as this would require accurate information about the core and coating

radii. The entire spectrum was found to be polarized in the sense of the pump beam – in the spectrum shown this was TM polarization. Different peaks were observed when the polarization of the pump beam was rotated, corresponding to transverse electric (TE) modes. We have traced on the spectrum what appears to be a single order of resonances appearing over the whole laser spectral region. Additional peaks also appear irregularly in the region 575-580nm, a second smaller series of regular peaks occur from 580-585nm, and another set of peaks dominate the spectrum at the longer wavelength region 590-595nm. In retrospect, we can tentatively assign the series of large peaks at 590-595nm as a lower order of resonance: this would be at least qualitatively consistent with the theory of whispering-gallery-mode dye lasers [112], which we have subsequently verified for a cylindrical laser. However, given the taper and the possibility of a non-circular or non-concentric cross-section of the fiber, we cannot draw any definite conclusions from observed spectral features. It should be remembered that for such large values of the size parameter the density of available modes is high ($\sim 100/\text{nm}$).

The same fiber used to produce figure 5.2 failed to exibit laser emission at pump intensities sufficient to break the fiber when ethanol was used as the dye solvent. This is a demonstration of the features of coating resonances described in section 3.4.3.1 and summarized in equations 3.46 and 3.47. We showed there that calculated resonant internal fields display significant overlap with the core region for $a/b > 0.67$ if $m_2 > m_1 = 1.5$, but only for $a/b > 0.73$ if $m_2 = 1.361$. Clearly, for the spontaneous emission and the gain from the dye to be coupled to the high-Q cavity modes requires such overlap; this is demonstrated by the computed fluorescence curves in figure 4.5. We have investigated this effect by studying the pump intensity threshold required to observe laser emission from a given capillary as the solvent refractive index was varied by mixing dye-doped ethanol and benzyl alcohol together in differing proportions. The results of such measurements on a fiber of size $b \simeq 60\mu$m are shown in figure 5.3, and display a sharp increase in the pump energy required to initiate lasing as the solvent refractive index is decreased from that of benzyl alcohol toward that of ethanol. The increase is too sharp to be explained simply in terms of greater focussing of the pump field by the higher refractive-index core, or

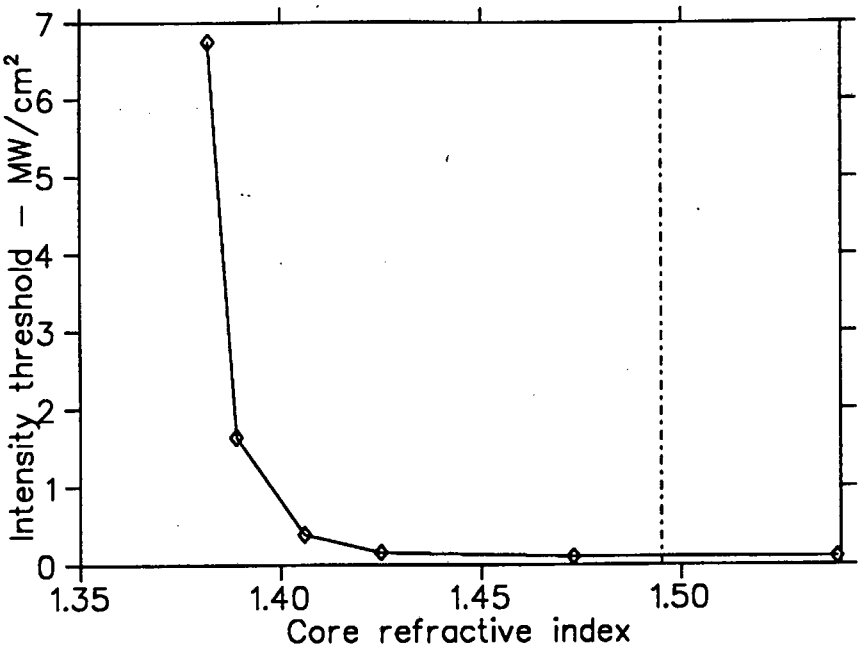

Figure 5.3: Observed pump intensity threshold required for laser emission from dye-doped solvent flowing in a capillary fiber with $a/b \simeq 0.7$ as the solvent refractive index is varied.

by a difference in the efficiency of the dye in the two solvents. Instead it reflects the transition from mode configurations which significantly penetrate the core region of the fiber to those which do not (see figure 3.14). Another point to note in figure 5.3 is that we do observe MDR laser emission from the fiber for $m_2 < m_1$ (the vertical dotted line on the diagram indicates the value of m_1). This is direct evidence that the observed peaks correspond to resonances of the composite cavity, as core resonances only exist for $m_2 > m_1$.

5.3 Core resonance laser emission

5.3.1 Introduction

By using a dye-doped solvent of high refractive index flowing in a thick-walled capillary fiber (see table 5.1) we have observed laser emission at wavelengths corresponding to the core resonances of the composite fiber [92]. The solvents used in the experiments were quinoline ($m = 1.626$) and benzyl alcohol ($m = 1.539$), and

these were doped with Rhodamine 6G. We have found this to be an ideal arrangement for studying some of the fundamental features of whispering-gallery-mode dye microlasers for the following reasons:

1. the cavity is stable and permanent, allowing the study of individual cavity resonances under different dye concentration and pump intensity conditions over an extended period of time. The cavity can be characterized independently using e.g. electron microscopy. The density of high-Q cavity modes is low, simplifying the identification of observed spectral features with resonant modes.

2. The excitation field or source function within the cavity is uniform compared to those in homogeneous spheres or cylinders. Consequently a uniform population inversion is expected to build up in the cavity below threshold, and we can analyse the resulting physical processes using a rate equation approach.

3. Cavity quantum electrodynamic effects are expected to be smaller than in spherical liquid droplets, because of the lower dimensionality of the cavity in the cylindrical case.

Most of our experiments were performed using quinoline as the dye solvent: this results in a relative refractive index for the cavity of $m \simeq 1.115$. It is frequently convenient to refer to the Q-values and mode spacings for a homogeneous fiber corresponding to our fiber core: as shown in section 3.4.3.2 these will be very similar to the core resonances in our composite fiber, the differences being due to the effects of the interference modulations described on page 68. The cavity Q-values of the resonant modes in our fiber cores when these are filled with quinoline are plotted in figure 5.4. These range from $\simeq 10^3$ up to $\simeq 10^{16}$ for the $2a = 75\mu$m fiber. These high-Q cavity modes may be easily brought above the threshold for laser emission by pumping the dye-doped fiber core, the internally circulating laser light leaking tangentially out of the core in all directions in the plane perpendicular to the fiber axis. Viewed from the outside using a microscope the laser emission appears to originate from two lines on the surface of the capillary fiber, corresponding to the

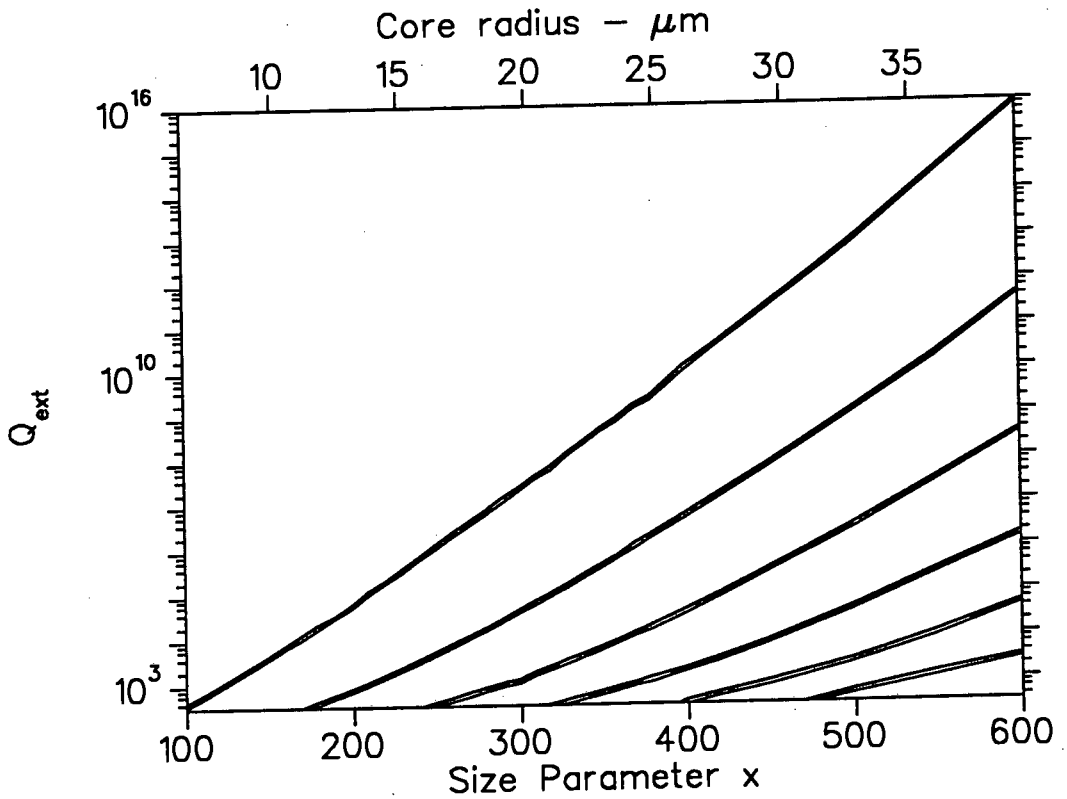

Figure 5.4: The computed Q_{ext} values for the whispering-gallery modes in the cavity formed by an $m = 1.115$ cylinder. The size parameter is plotted on the bottom axis, while the approximate corresponding core size of a capillary fiber (computed using $\lambda = 600$nm, $m_1 = 1.458$) is plotted on the top axis.

edges of the fiber core imaged through the curved glass wall of the capillary. The measured divergence of the laser emissions out of the laser plane is of the order of 20mrad. Various observed features of the laser emission are now described and analyzed.

5.3.2 Spectral profile

The wavelength regions in which laser emissions are observed depend on the absorption and gain profiles of the dye-doped solvent and on the external cavity Q-values of the resonant modes in the fiber under study. The absorption and emission profiles are determined primarily by the properties of the laser dye: these are well known [148]. The absorption profile of Rhodamine 6G has its maximum about 530nm; it is therefore efficiently pumped by a frequency-doubled Nd:YAG beam. The absorption cross-section decreases towards longer wavelengths, although there is still some small absorption even at $\lambda \geq 600$nm. The gain curve of the dye peaks around $560 - 570$nm, and thereafter decreases towards longer wavelengths, having a long tail extending well past 620nm. A simplified sketch of these properties based on that given by Svelto [160] is shown in figure 5.5. The quinoline used as a solvent in our experiments is strongly absorbing in the short-wavelength end of the visible, and slightly absorbing between 550 and 620nm, the absorption decreasing slowly towards longer wavelengths. We have measured the optical aborption of 10^{-4}M and 2×10^{-3}M solutions of Rh6G in quinoline in a cuvette at a number of wavelengths over a path length of several centimetres using a scanning monochromator and a tungsten lamp, and we have plotted these in figure 5.6 as $Q_{abs} = 2\pi m/\lambda\alpha$, where α is the measured absorption coefficient. Hill and Benner [78] and subsequent workers have expressed the effective Q-value of a resonant mode in a microparticle as

$$\frac{1}{Q} = \frac{1}{Q_{abs}} + \frac{1}{Q_{ext}} \tag{5.1}$$

The resonant Q-value is thus dominated by the smaller of Q_{abs} and Q_{ext}. Campillo and colleagues [112] have shown how this leads to a variation in the output coupling of the various mode orders with wavelength (see page 20). We can confirm the usefulness of these ideas in analysing our capillary-fiber laser by studying ob-

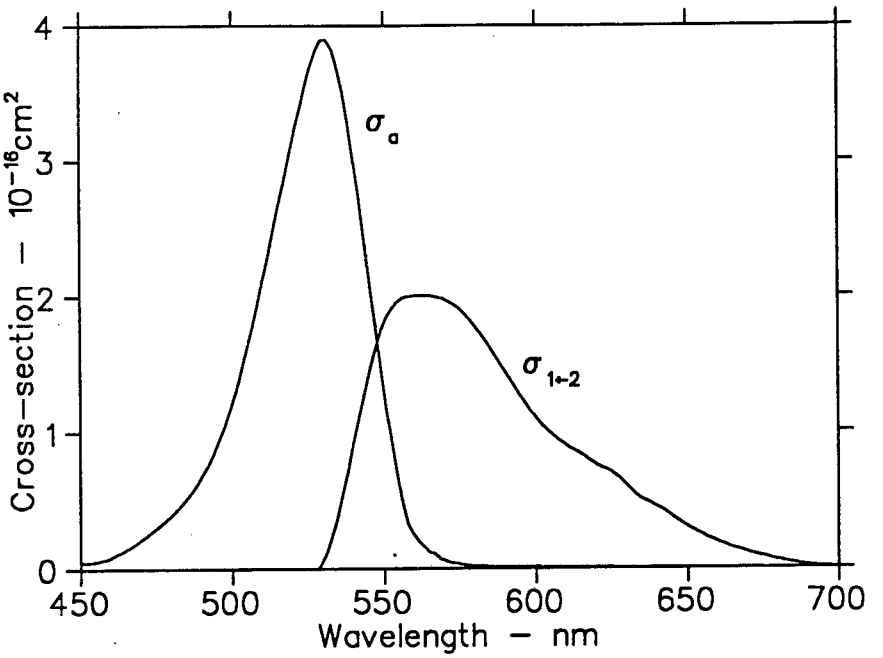

Figure 5.5: Wavelength dependence of the cross-sections for absorption and stimulated emission for the laser dye Rhodamine 6G used in the experiments.

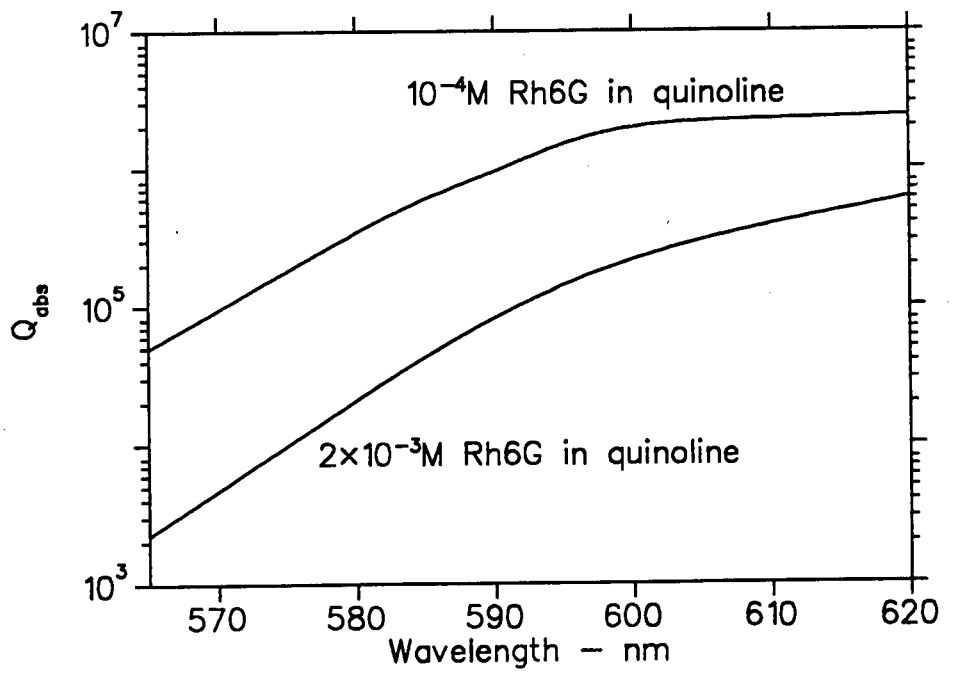

Figure 5.6: Measured values for Q_{abs} for 10^{-4}M and 2×10^{-3}M solutions of Rh6G in quinoline, under low-intensity illumination.

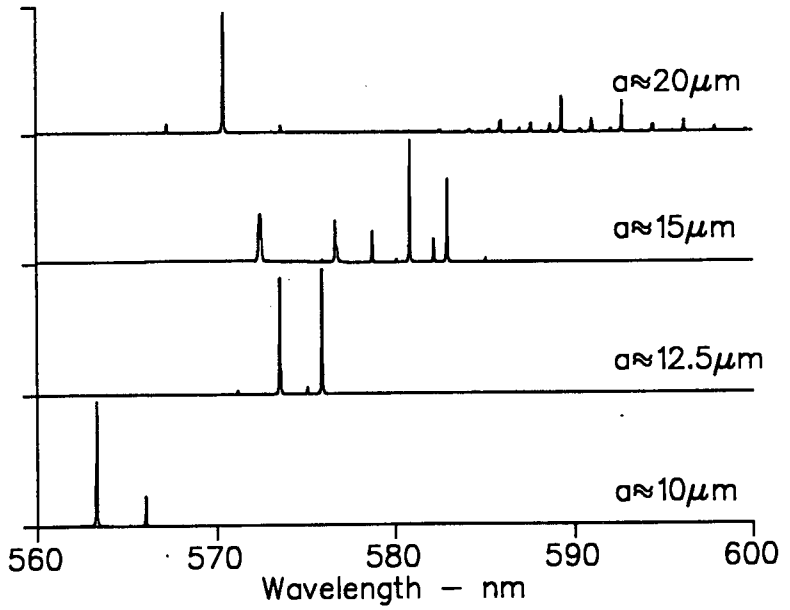

Figure 5.7: Observed laser spectra for 0.3mJ/pulse TM illumination of 10^{-4}M Rh6G quinoline flowing in capillaries of nominal core radii of 10, 12.5, 15 and 20μm. With increasing core size the first-order modes become intrinsically narrower, appearing at longer wavelengths. The second-order ($l = 2$) modes appear distinctly for the $a = 20\mu$m fiber.

served laser spectra from different fibers. Figure 5.7 shows observed laser spectra recorded from fibers of nominal sizes $b \sim 125\mu$m and $a \simeq 10$, 12.5, 15 and 20μm. The general trend for the three smaller fibers is a shift towards longer wavelengths with increasing size. The explanation for this lies in the wavelength dependence of the effective Q-values for the different fibers shown in figure 5.8 and the gain profile of the laser dye (figure 5.6). The values for Q_{ext} for $a \simeq 10\mu$m (corresponding to $x \simeq 160$ in figure 5.4) are $Q_{ext} \simeq 2 \times 10^4$. Such Q values are significantly smaller than the absorptive Q even at the peak of the gain profile at $\lambda \simeq 565$nm; therefor the effective Q for these modes is approximately equal to the Q_{ext} - see figure 5.6. Consequently the laser spectrum appears in the spectral region providing the greatest gain, corresponding to the peak of the gain profile. The $a \simeq 12.5\mu$m fibers have $Q_{ext} \simeq 10^5$ for the first-order modes, and these are seen to be substantially reduced at $\lambda = 565$nm (where $Q \simeq Q_{abs} = 3 \times 10^4$), the Q-values increasing towards longer

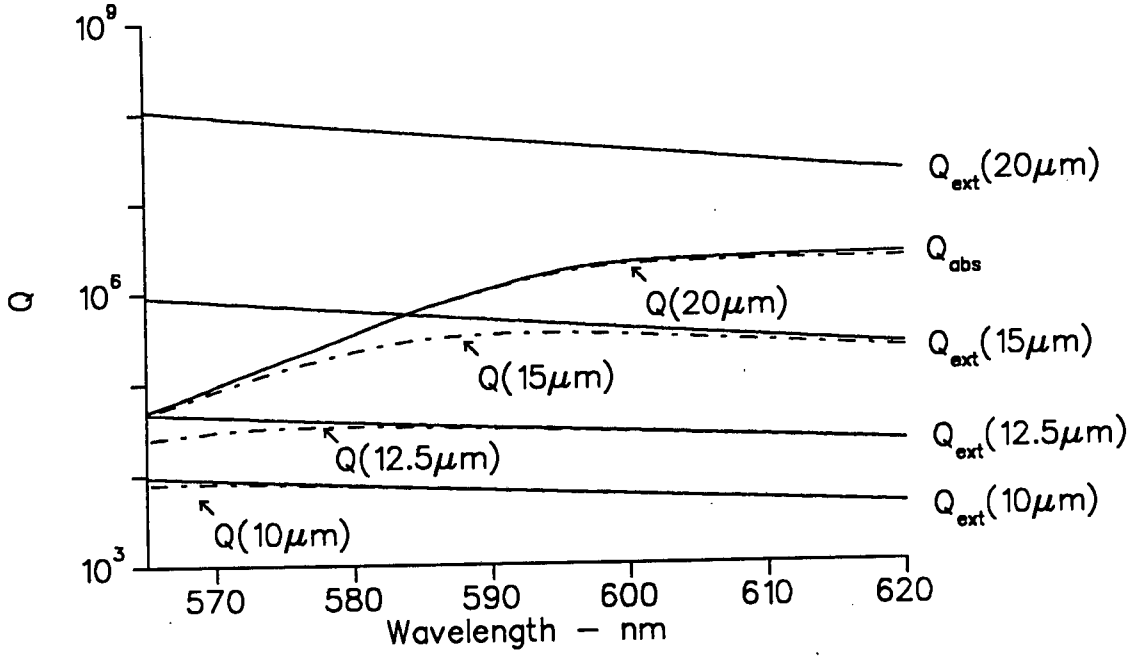

Figure 5.8: The approximate values for the total Q (broken curves) and the external and absorptive Q (solid curves) for the first-order resonances for fibers of different core sizes as a function of wavelength. The gain of the Rhodamine 6G is decreasing towards longer wavelengths over the spectral region shown here. Laser emission occurs at the wavelength which maximises the combination of cavity Q and gain. The calculated Q_{ext} values are for a homogeneous cylinder of refractive index 1.115, corresponding to the m_2/m_1 ratio for quinoline in the hollow fused-silica fiber.

wavelengths as the absorption decreases. The gain profile also decreases towards longer wavelengths, but more slowly. At $\lambda = 575$nm the Q's of these modes will be only slightly reduced by absorption, while the main effect at longer wavelengths will be a decrease in gain. The modes therefore reach threshold first at $\lambda \simeq 575$nm, where the effective Q has its maximum. Similarly for $a \simeq 15\mu$m, the laser emission appears at the shortest wavelength (highest gain) for which $Q_{abs} \geq Q_{ext}$. A new situation arises for the $a \simeq 20\mu$m fiber, where two discrete sets of peaks are observed. The longer-wavelength set which appears first as the pump intensity is increased from zero continues the trend of the three smaller fibers, appearing at longer wavelengths as the Q-values increase. These correspond to the first-order modes with $Q_{ext} \simeq 3 \times 10^7$. The new set of peaks occurring at $\lambda = 570$nm are the second-order modes with $Q_{ext} \simeq 9 \times 10^4$. These are not observed for smaller fibers because they have insufficient Q to reach threshold under the given dye concentration/pump intensity conditions. Figure 5.6 shows that the absorption of the 10^{-4}M Rh6G quinoline solution decreases only slowly for $\lambda > 590$nm; this decrease is comparable to that of the gain, and consequently the first-order modes lase at $\lambda = 590$nm, even though their $Q_{ext} > Q_{abs}$ at this wavelength. Consequently they are less efficiently coupled out of the fiber (with efficiency $Q_{ext}/Q \simeq 0.05$) than the second-order modes (with efficiency $\simeq 1$), and appear at reduced strength in the observed spectrum.

In general, the spectral profile of the laser emission consists of one or more sets of single or double peaks (depending on the degree of polarization – see page 126), each set corresponding to a given mode order with lower-order modes occurring at longer wavelengths. Modes appearing near the peak of the gain curve ($\lambda \simeq 565$nm) have $Q_{ext} < Q_{abs} (= 5 \times 10^4$ for 10^{-4}M Rh6G quinoline) at that wavelength. Peaks at the long-wavelength end of the gain profile ($\lambda > 595$nm for 10^{-4}M Rh6G in quinoline) have $Q_{ext} \geq Q_{abs}$ ($\simeq 10^6$ for 10^{-4}M Rh6G at $\lambda = 595$nm). If $Q_{ext} > Q_{abs}$, these peaks will appear at reduced strength. Peaks occurring between these two extremes will have $Q_{ext} \simeq Q_{abs}$. It should be noted that these statements are true when only a small fraction of dye molecules is in the excited state: if a significant proportion of dye molecules is in the excited state, the absorption of the dye will be decreased.

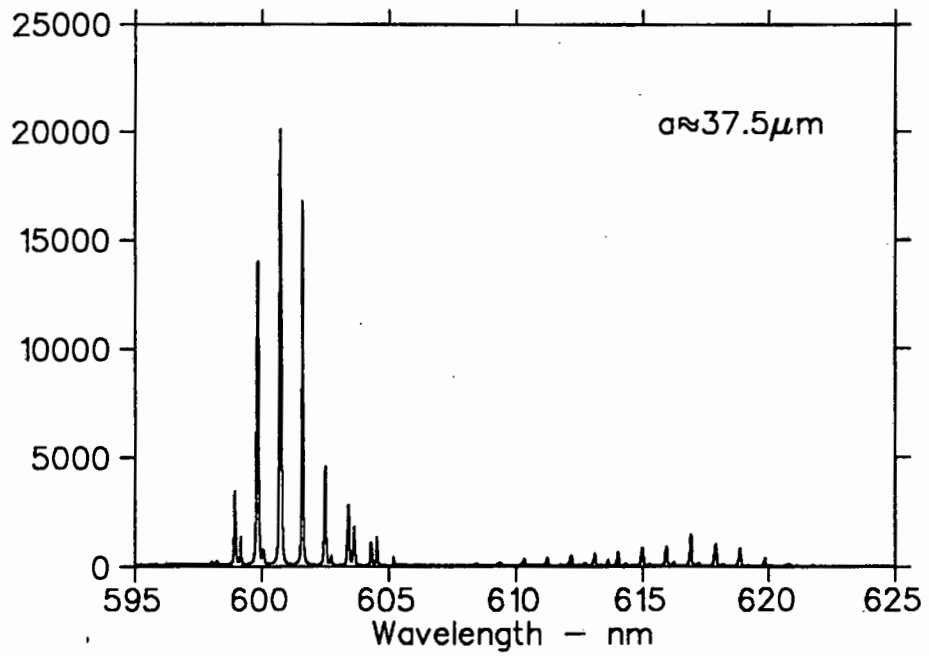

Figure 5.9: Laser spectrum recorded from a $2a = 75\mu$m fiber filled with 2×10^{-3}M Rh6G-doped quinoline, pumped with a pulse energy of 0.3mJ/pulse. The smaller set of peaks at longer wavelengths reach threshold first as the pump intensity is increased.

We demonstrate the application of these rules to the analysis of the laser spectrum from a large fiber by studying the spectrum shown in figure 5.9, recorded from a fiber with nominal core size $2a = 75\mu$m. The dye concentration used to record the spectrum in figure 5.9 was 2×10^{-3}M; the Q_{abs} for this solution is shown in figure 5.6. Figure 5.4 shows that for fiber with $a \simeq 37.5\mu$m the first-order modes are extremely narrow, having $Q_{ext} \sim 10^{16}$. Such modes will be greatly broadened by absorption and will be only very weakly coupled to the external field. The peaks observed at $\lambda \simeq 610 - 620$nm in the spectrum are expected to have $Q_{ext} \geq Q_{abs}$ at that wavelength, seen in figure 5.6 to be $Q_{abs} \simeq 3 - 6 \times 10^5$. Hence we may associate these with the $l = 4$ modes in figure 5.4, which have $Q_{ext} \simeq 5 \times 10^5$. The larger peaks at $\lambda \simeq 600$nm must be due to modes with $Q_{ext} \leq Q_{abs} \sim 10^5$; this is slightly larger than the external Q of the 5th-order modes. The fourth-order modes have $Q_{ext} > Q_{abs}$ (coupling efficiency~ 0.4), and so they appear at reduced intensity in the emitted spectrum. By reducing the pump intensity we have confirmed that the

longer-wavelength peaks appear at lower pump intensities than those at $\lambda \simeq 600$nm and must therefore be due to intrinsically higher-Q modes, providing additional evidence supporting the assignment of mode orders. More accurate estimates of the Q_{ext} values may be obtained by the use of the core size computed from the observed mode spacing (next section).

A point to note about our laser spectra such as those shown in figures 5.7 and 5.9 is the excellent signal-to-noise ratio. Under the conditions of figure 5.7 the typical peak height to background ratio in a summed spectrum is perhaps 5000. This is partly because of the different propagation characteristics of the fluorescent and laser emissions from the fiber - the laser emissions propagate as a cylindrical wave, their intensity decreasing approximately linearly with distance from the fiber, while the integrated fluorescence from the fiber decreases as $1/r^2$. Consequently our linear detector array which is in the plane of the laser emission receives a relatively weak signal from the incoherent fluorescence.

5.3.3 Mode spacing and assignment

The spacing of the resonant modes of the same polarization and order and with azimuthal mode number n differing by unity may be approximated for a homogeneous dispersionless cylinder using the Chýlek formula [134]. We have shown on page 66 how this may be extended to the core resonances in our capillary fiber. However, in order correctly to predict the mode spacings we need to consider the effects of the dispersion of the solvent and of the fused silica. This is most precisely done using *a priori* knowledge of the particle parameters a and b and of the functions $m_1(\lambda)$ and $m_2(\lambda)$ to perform the boundary-value calculations. However, by assuming that the dispersion is small, and that it may be modelled as linear over several nanometres, we have derived a simple correction factor expressing its effect. We use the fact that the resonances correspond to circumferentially travelling waves which are in phase with themselves after a round trip, which means that a small change in refractive index for a given mode must result in a corresponding change in the resonant wavelength, so that the ratio ma/λ remains constant. Applying this to our core resonances, and assuming that the dispersion of m_1 and m_2 are linear, one can

Wavelength - nm	quinoline index	fused silica index
560	1.6292	1.4595
570	1.6274	1.4591
580	1.6258	1.4587
590	1.6243	1.4584
600	1.6228	1.4580
610	1.6215	1.4577
620	1.6202	1.4574

Table 5.2: Refractive indexes for quinoline and fused silica over the laser wavelength range.

derive

$$\Delta x_c + \delta x_c = \Delta x_c \left(1 + \frac{K_2\lambda}{m_2} - \frac{K_1\lambda}{m_1}\right) \tag{5.2}$$

where Δx_c is the dispersion-free mode spacing, δx_c is the correction resulting from dispersion and K_1 and K_2 are the linear dispersion constants for media m_1 and m_2 respectively, such that e.g. $m_1(\lambda + \Delta\lambda) = m_1(\lambda) + K_1\Delta\lambda$. Values for the dispersion constants for fused-silica and quinoline were obtained by fitting a Cauchy formula to known values [7, 52] of the refractive index for the two media at wavelengths corresponding to several atomic emission lines. In the case of quinoline, the values were checked experimentally, by measuring the refractive index at three spectral lines using the angle of minimum deviation in a hollow prism. A summary of the refractive index data over the wavelength range of interest is in table 5.2. To investigate the validity of equations 5.2 and 3.48, we have plotted observed values of $\lambda^2/\Delta\lambda$ versus the manufacturers specified core size for a range of core sizes. Laser modes were observed using 10^{-4}M–10^{-2}M Rh6G quinoline at wavelengths in the range 565 – 610nm. Results are shown in figure 5.10: the solid line represents a best fit to the data points. This fit has a slope of 5.27, giving $\Delta x_c + \delta x_c = 0.87$ if the value for m_1 at 600nm is used. For comparison, equations 5.2 and 3.48 give $\Delta x_c + \delta x_c = 0.89$, using the values for m_1, m_2, K_1 and K_2 at $\lambda = 600$nm. This difference of 2%

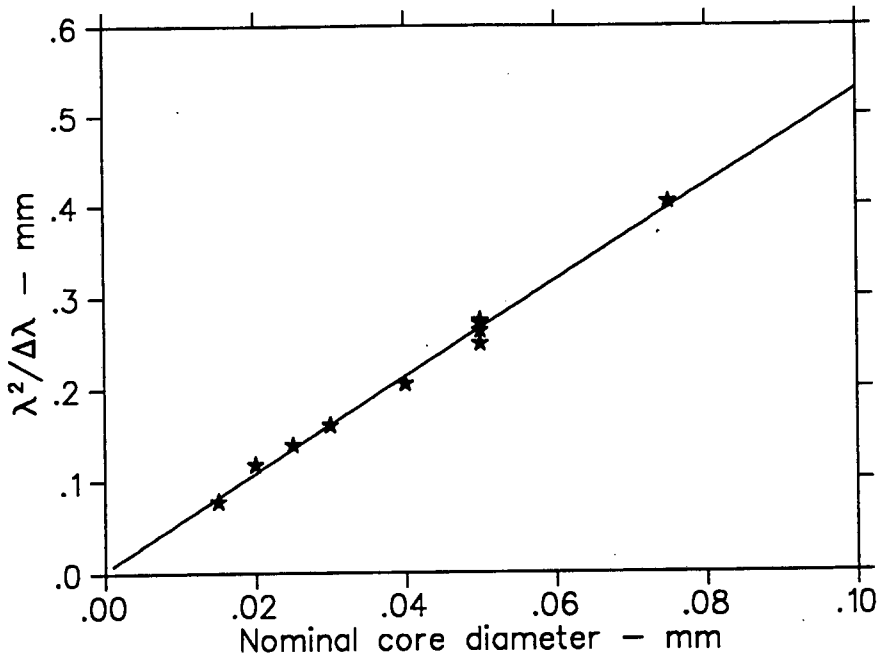

Figure 5.10: Observed $\lambda^2/\Delta\lambda$ as a function of the manufacturers specified core sizes for the capillaries investigated. The data points are represented by stars, the straight line is the best fit to the points.

can be ascribed to the approximation 3.48, which overestimates the mode spacing for narrow modes by typically a few percent [42], and to the uncertainties in the manufacturers core sizes. Taking these into consideration agreement between the observed slope and equations 5.2 and 3.48 is excellent.

The observed mode spacing can be used to estimate the core size of a lasing fiber: we can then compute the Q-values of the observed laser modes. For the fibers with nominal core sizes $2a = 15$, 20 and 25μm filled with quinoline ($m_2/m_1 \simeq 1.115$) only the first-order ($l = 1$) modes can reach threshold, as $l \geq 2$ modes have only low Qs. For example, for the $2a \simeq 20\mu$m fiber used to obtain the spectrum in figure 5.7, the observed value of $\lambda^2/\Delta\lambda$ is 0.1177mm. Using equations 3.48 and 5.2, the size may be estimated from the definition of the core size parameter and using equations 5.2 and 3.48

$$a = \frac{\lambda^2(\Delta x_c + \delta x_c)}{2\pi m_2 \Delta\lambda} \tag{5.3}$$

to be $a \simeq 11.33\mu$m, or $x_c \simeq 184.4$. In fact equation 3.48 overestimates the mode spacing for narrow modes, as mentioned above. Using the known relative refractive

index of the cavity at 563nm ($m = 1.116$, table 5.2) we have computed the the resonance locations and Q-values in the region of $x = 184$: these are shown in table 5.3. The dispersion-free mode spacing found thus is $\Delta x_c = 0.9138$, approximately 1.6% less than that computed using the Chýlek formula equation 3.48. Using this improved value for Δx_c in equations 3.48 and 5.3 gives $a \simeq 11.18\mu$m, or $x_c \simeq 181.7$ and $x_c \simeq 180.8$ for the two peaks observed. The azimuthal mode numbers for the first-order modes in this region of x_c are $n = 193$-194 and the Q-values $Q \simeq 3.3 \times 10^4$ for the TM modes (see table 5.3): ignoring the possibility of anomalous dispersion due to the presence of gain in the fiber core, the error in these mode assignments for n cannot be more than ± 1. The $l = 2$ modes have $Q \simeq 500$, and can be disregarded as potential laser modes under our conditions.

Similar mode assignments can be made for the $a \simeq 12.5$ and $a \simeq 15\mu$m core radius fibers, although the uncertainty in n increases to ± 2 for these. For the larger fibers, the situation is slightly more complex, as modes with orders $l > 1$ also need to be considered as potential lasing candidates. However, using the simple rule relating the laser wavelength to values of Q_{abs} and Q_{ext} which was derived in the previous section we can estimate the approximate Q_{ext} values and hence the order of the observed modes, as has been demonstrated for the $2a = 75\mu$m fiber. The Q_{ext} values can then be determined more precisely from the observed mode spacing by performing boundary-value computations.

We have attempted to confirm the mode assignments for the smaller fiber core sizes by studying the angular dependence of the laser emissions from a single mode in the scattering plane, in the hope of independently verifying the assignment of the mode number n. The smaller fibers (with core sizes $a = 10, 12.5\mu$m) can easily be made to lase predominantly in a single mode by using a suitable pump irradiance: unfortunately the light signal from a single laser shot under such conditions was too weak to record the angular pattern on the photographic film which we used for detection. The use of an intensified diode array might be sufficient to record such a pattern; however there is some uncertainty about the length of fiber over which emissions might be expected to be coherent, given the two-dimensional cavity geometry.

Polarization	Size Parameter x	Partial wave n	Order l	Q-value
TM	180.171	185	2	5.08×10^2
TE	180.343	185	2	4.20×10^2
TM	180.432	193	1	3.14×10^4
TE	180.742	193	1	2.62×10^4
TM	181.098	186	2	5.24×10^2
TE	181.271	186	2	4.32×10^2
TM	181.346	194	1	3.31×10^4
TE	181.657	194	1	2.77×10^4
TM	182.024	187	2	5.40×10^2
TE	182.199	187	2	4.45×10^2
TM	182.259	195	1	3.49×10^4
TE	182.571	195	1	2.92×10^4
TM	182.951	188	2	5.57×10^2
TE	183.126	188	2	4.60×10^2
TM	183.173	196	1	3.67×10^4
TE	183.485	196	1	3.07×10^4
TM	183.878	189	2	5.74×10^2
TE	184.054	189	2	4.74×10^2
TM	184.086	197	1	3.87×10^4
TE	184.399	197	1	3.24×10^4
TM	184.805	190	2	5.91×10^2
TE	184.982	190	2	4.89×10^2

Table 5.3: Modal locations and Q-values for a cylindrical cavity with $m = 1.116$ in the region of $x = 184$.

5.3.4 Interference modulation of Q-values

The enhancement and reduction of the core-resonance Q-values due to reflection of resonant light from the external surface of the fiber, which we described on page 68, plays an important role in determining the detailed structure of the observed laser spectra [93]. The fluctuations in the resonant Q_{ext} values for a single mode order as a function of the size parameter result in a corresponding series of maxima and minima in the strength of the observed laser peaks. This is particularly noticeable for the TM modes, for which the effect is stronger as demonstrated in figure 3.21. This is illustrated in figure 5.11, which shows observed laser spectra from 2×10^{-3}M Rh6G quinoline in fibers with core radius $a = 25\mu$m and with coating radius $b \simeq 63\mu$m and $b \simeq 83\mu$m. The interference period given by equation 3.49 calculated using the manufacturers specified values for a and b is marked on each spectrum. Spectra are shown for both pump polarizations, the modulation of the observed lasing strengths being more pronounced for the TM modes. Similar effects are observed for fibers of different sizes and are a prominent feature of observed laser spectra, particularly for larger core sizes. The modulations for the two mode polarizations are out of phase as a result of the different boundary conditions on reflection for the two polarizations. In a different experiment, we have studied the observed TM-pumped laser spectra from a fiber immersed in water. This has the effect of reducing the refractive index mismatch at the external surface, and thus the amount of internal reflection at this surface. Thus immersion of a fiber in water might be expected to reduce the interference effect.[1] Results from such an experiment using a length of the fiber used to record the upper traces in figure 5.11 are shown in figure 5.12. The figure shows observed laser spectra for TM pumped lasing from the fiber in air (lower trace) and when the same fiber is immersed in water (upper trace). The TM laser peak heights oscillate in a regular fashion in the lower spectrum as a result of the interference modulation of the Q-values. Immersion of the fiber in water (upper spectrum) substantially reduces the modulations, resulting in a relatively smooth variation in peak heights and further demonstrating that the observed modulations

[1] I wish to thank an anonymous referee for suggesting this experiment [93].

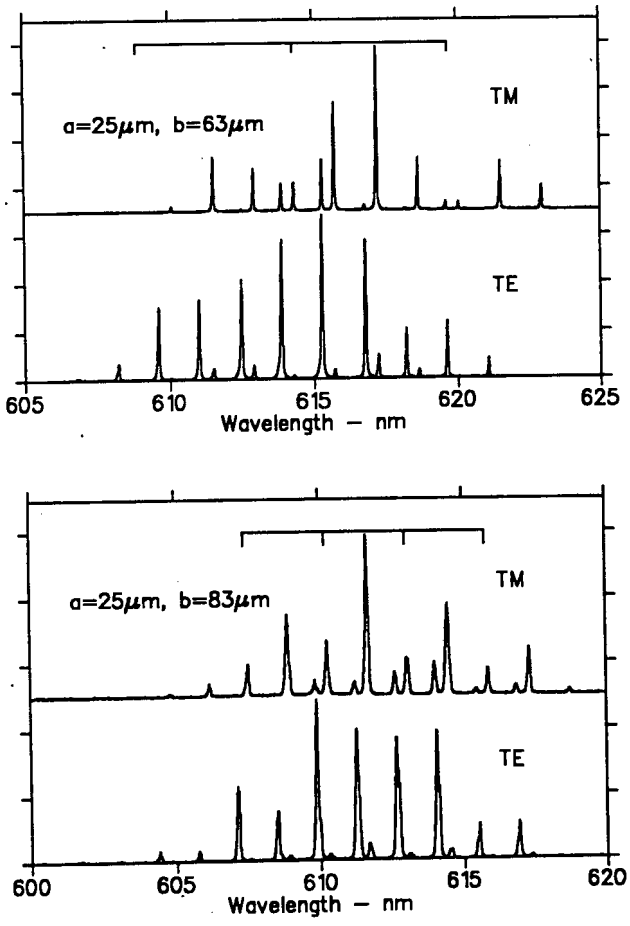

Figure 5.11: Laser spectra observed from Rh6G quinoline in two capillary fibers with nominally identical core radii but with different external radii, showing the modulation of the laser peak strengths caused by the interference effect. The expected period of the modulation is indicated on the figure for the two cases. Spectra are shown for both pump polarizations: the modulations are more visible for the TM pump case.

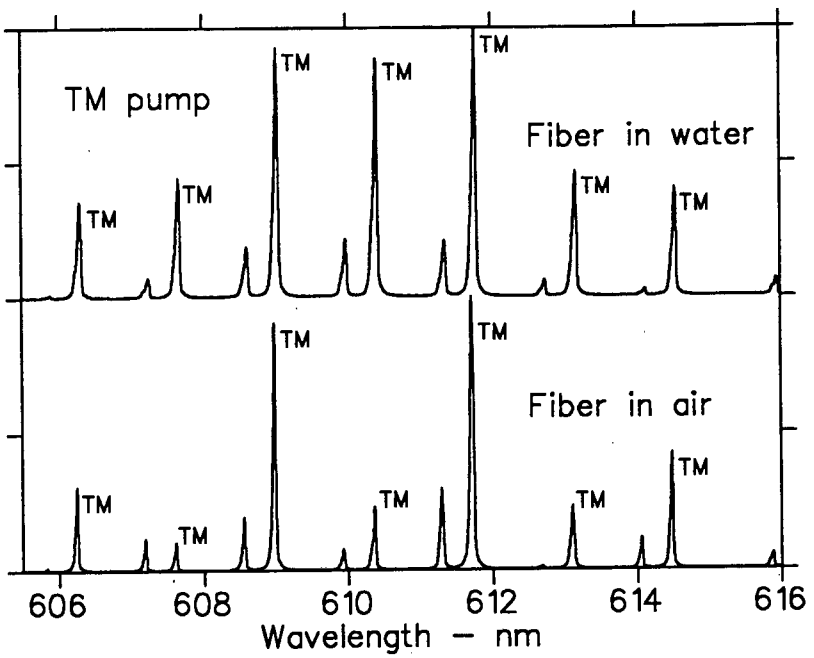

Figure 5.12: Effect on the TM-pumped laser spectrum of immersing the fiber under study in water. The water decreases the refractive index discontinuity at the external surface of the fiber, reducing the reflection at that surface, and hence the amplitude of the interference modulations.

are due to the interference effect.

The Q-value modulations will have a different effect depending on whether the Q-values of the modes being investigated are limited by absorption or not. If the effective Q-values are absorption-limited, an enhanced Q_{ext} will serve to decrease the output coupling Q/Q_{ext}, while the effective Q-value will remain $Q \simeq Q_{abs}$. Therefore the enhanced Q_{ext} value will lead to a smaller peak appearing in the observed spectrum, and vice versa. Conversely, if $Q_{ext} < Q_{abs}$, then $Q \simeq Q_{ext}$ will be enhanced if Q_{ext} is enhanced, while the output coupling will remain close to unity. In this case, enhanced (reduced) Q_{ext}-values will lead to enhanced (reduced) peaks in the observed spectra.

5.3.5 Rate equations

We have used a simplified rate equation approach to investigate the input versus output behaviour, the polarization, the time dependence and the possibility of ob-

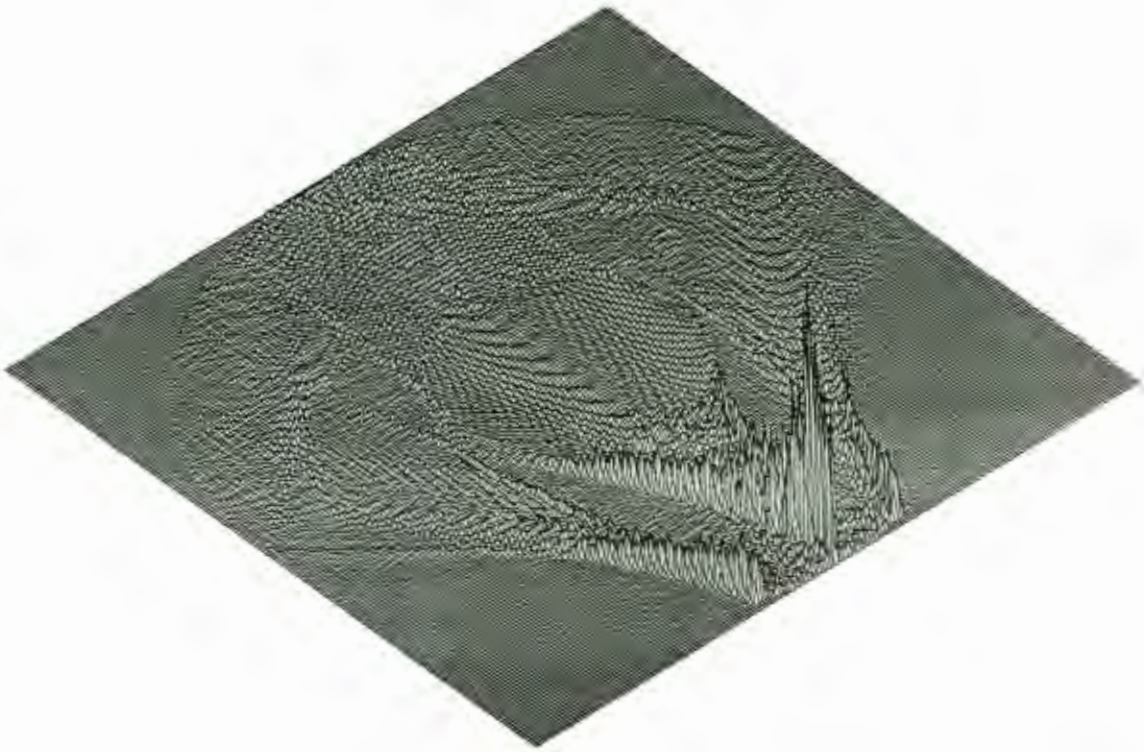

Figure 5.13: A surface plot of the source function representing the TM pump field at 532nm in an illuminated capillary with parameters $a = 25\mu$m, $b = 63\mu$m, $m_1 = 1.458$ and $m_2 = 1.626$. The maximum value of the source function in the core region is 5.3× the incident intensity.

serving cavity QED effects in our cylindrical whispering-gallery-mode laser. Such a simplified approach is inappropriate for the spherical droplet laser because of the highly inhomogeneous pump field within the droplet due to the focussing of the incident beam by the curved droplet surface, because of the substantial cavity QED alteration of the spontaneous and stimulated transition rates for excited dye molecules, and because of the large number of lasing modes. In our cylinder these effects are greatly reduced: figure 5.13 shows a sample calculation of the pump field in a fiber with $a = 25\mu$m, $b = 63\mu$m, $m_1 = 1.458$ and $m_2 = 1.626$ illuminated with a TM wave of wavelength $\lambda = 532$nm. There is little focussing of the incident beam in the fiber core, due to the small refractive index mismatch at the core/coating interface - the maximum value of $\underline{E}.\underline{E}^*$ is 5.3 times the incident field intensity in the core region, and even this is confined to only a small region of the fiber core, the source function being very close to unity over most of the core region. This maximum occurs near to the shadow face of the fiber and corresponds to the region

of the Descartes line previously observed in cylindrical liquid jets [134]. In practice, this peak in the source function is further reduced due to absorption in the fiber core at the excitation wavelength. In contrast to the typical source function enhancements of several hundreds occurring in homogeneous liquid droplets [16], the source function in the core region of our cylinder is virtually flat. Likewise, the alteration of the transition rates due to cavity QED effects is expected to be greatly reduced in our fiber compared to that observed in liquid droplets, due to the lower dimensionality of the cylindrical cavity [21]. Studies of the rate equations for microcavity lasers [118, 173, 174] have shown that one effect of increased coupling of spontaneous emission into a single cavity mode is to make the threshold in the input-output intensity curve less well defined. Observations of the emissions from our fiber show a well-defined laser threshold in the emissions from a given laser mode – the threshold is easy to examine experimentally because, as we have mentioned, our spectrometer detects the coherent emissions from the fiber preferentially due to their propagation as cylindrical rather than as spherical waves. A demonstration of the typically sharp laser threshold which we observe from a fiber is shown in figure 5.14, which shows a single laser mode as the pump intensity is increased in steps of two. The pump intensity is increased by a factor of 4× from the first to the third spectrum, while the maximum laser signal increases by a factor of almost 60. The observation of a sharp laser threshold implies that the coupling factor β of spontaneous emission from excited molecules in the mode volume into the laser mode is relatively low. This is to be expected because the emission profile of Rhodamine 6G is broad (perhaps 50nm) and there is a large number of different modes which are available to an excited dye molecule in the mode volume [21, 40, 91]. The value for β is expected to be limited to at most the ratio of the cavity resonance linewidth to that of the Rh6G spontaneous emission, giving an upper limit of $\beta \simeq 5 \times 10^{-4}$ for the fiber used to record figure 5.14. We have assumed a slightly smaller value for β in our calculations. A factor encouraging the use of a rate-equation approach in the cylindrical geometry is that for several reasons we see typically fewer modes above threshold than have been reported from spherical liquid droplets [18]. Thus our cylindrical laser offers an opportunity to uncouple to a certain extent the effects of the cavity

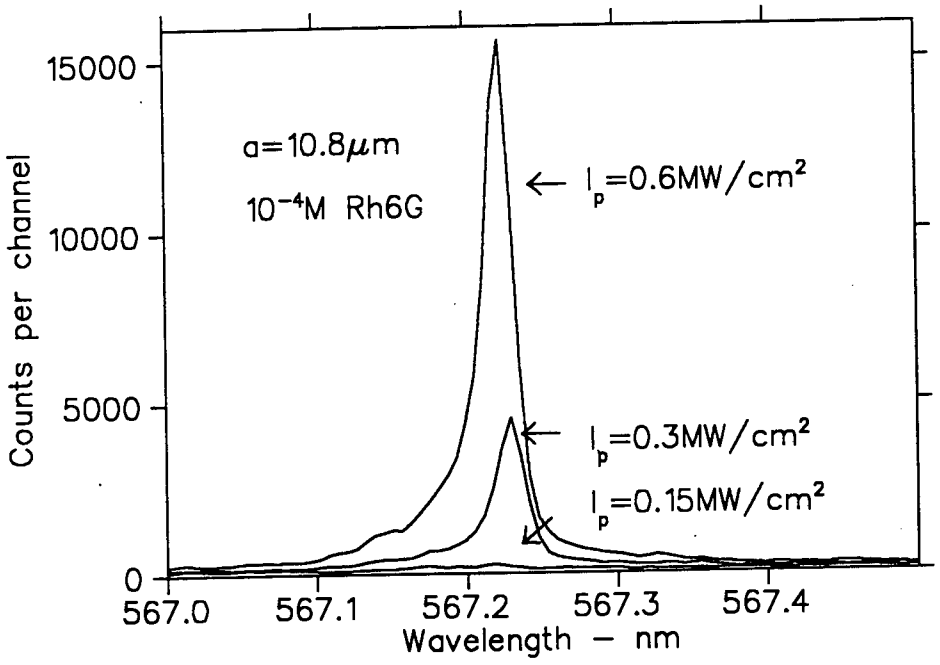

Figure 5.14: A portion of the spectrum observed from a fiber with $a = 10.8\mu$m as the pump intensity is increased, showing a sharp nonlinearity which is characteristic of laser threshold. The maximum signal observed at the laser wavelength increases by a factor of 57 while the pump intensity is increased by a factor of 4. Each curve represents the sum of thirty laser shots, which results in some smoothing of the apparent laser threshold due to the shot-to-shot fluctuations in the pump energy. The laser peak shown is one of two which reach threshold simultaneously.

QED enhancement of the spontaneous emission and the observed multimode lasing from the conventional laser physics, as a first step to quantitatively analysing laser processes in whispering-gallery-mode dye lasers.

We initially make the following assumptions in our rate equation analysis:

1. The Rhodamine 6G solution behaves as a simple four-level laser system [76], the transition probabilites for absorption, fluorescence and stimulated emission being identical to those in the bulk medium. The use of these bulk transition constants in our analysis, specifically the spontaneous emission lifetime and the stimulated emission cross-section of the Rh6G dye molecule, needs justification. Without a comprehensive analysis of the density of states in a cylindrical cavity such as that being investigated it is impossible to be sure whether our use of these constants is valid; however we believe that the excellent agreement which we find between our numerical analysis and the observed pump intensity thresholds and critical dye concentrations implies that the use of these constants is a reasonable approximation under the conditions of our experiments.

   The simplified four-level system assumes that in thermodynamic equilibrium virtually all the dye molecules are in the ground state. The pump pulse excites molecules into the upper excited state, whence they very quickly decay non-radiatively to the upper lasing level. Molecules in this level decay radiatively by fluorescence (with a lifetime τ_{21}) or stimulated emission to the lower lasing level. (We ignore the possibility of intersystem crossing to triplet excited states or of excited-state absorption, and assume that each absorbed photon will result in an emitted photon at a later time and a longer wavelength.) The lower lasing level again has a very short lifetime, molecules returning to the ground state at such a speed that we may assume that the population in the lower lasing level is zero. We assume that the gain profile of the dye is homogeneously broadened. We ignore the possibility of stimulated emission by longitudinal guided waves, which may act as an additional loss mechanism for the excited-state population – we believe that this is valid because of the

relatively short length of fiber illuminated in our experiments.

2. The internal field intensity in the core region at the illuminating frequency is uniform and equal to the irradiance of the pump beam: this gives the strength of the pump field.

3. Excited dye molecules have their dipole moment parallel to the electric field of the mode being studied.

4. Only a single mode exists above threshold.

5. The resonant Q-values may be expressed by equation 5.1, where Q_{abs} is calculated from the observed attenuation coefficient measured at low intensities.

For our capillary-fiber laser we assume that the round-trip distance is $2\pi a m_1/m_2$; we then easily derive

$$\frac{dN}{dt} = \frac{I_p \sigma_p}{h\nu_p}(N_t - N) - \frac{\sigma I}{h\nu}N - \frac{N}{\tau_{21}} \tag{5.4}$$

$$\frac{dI}{dt} = Ic\left[\frac{\sigma}{m_2}N - \frac{2\pi}{\lambda Q}\right] + \beta\frac{N}{\tau_{21}}\frac{h\nu c}{m_2} \tag{5.5}$$

where N_t is the total number of active molecules per unit volume, N is the number density of molecules in the upper lasing level, I is the laser intensity in the laser mode, I_p is the pump intensity, τ_{21} is the spontaneous-emission lifetime for excited dye molecules and σ and σ_p are the cross-sections for stimulated emission and pump absorption respectively. Values for the various constants were obtained from the literature: these are summarized, with sources, in table 5.4. Where several sources give different values, perhaps measured under different experimental conditions, we have chosen those which are near to the mean of the quoted values.

We have assumed a gaussian time dependence for our pump beam, and have solved these equations numerically using the Runge-Kutta method. The results show typical features of laser processes in the temporal and output-versus input response of the cavity, i.e. a low pump intensity regime where the output is dominated by fluorescence and is linearly related to the excitation strength, a sharp threshold discontinuity, and a high pump intensity region, with output again being linearly

Absorption cross-section $\sigma_p(\lambda = 532\text{nm})$	$3.8 \times 10^{-16}\text{cm}^2$	Ref: Hillman [76]
Stimulated emission cross-section σ	$2 \times 10^{-16}\text{cm}^2$ ($\lambda = 560\text{nm}$) $1 \times 10^{-16}\text{cm}^2$ ($\lambda = 600\text{nm}$)	Ref: Svelto [160]
Fluorescence decay lifetime τ_{21}	3.7ns	Ref: Hillman [76]

Table 5.4: Constants for Rhodamine 6G used in rate equation analysis.

related to input. The computed results assume a value for the spontaneous emission coupling factor β in equation 5.5 of $\beta = 10^{-4}$; however we have used a variety of coupling factors and find that the basic features of the observed processes remain unchanged as long as this coupling remains small. These features are demonstrated in figure 5.15 which shows the assumed time-dependence of the pump pulse (upper plot) and the computed population inversion and laser intensity as a function of time for a mode with $Q_{ext} = 1.6 \times 10^5$, $Q_{abs} = 10^8$, a dye concentration of 10^{-4}M and a peak pump irradiance of 0.5 MW/cm^2. The features shown are typical of those found in other laser systems; the population inversion builds up until the onset of laser action whereafter it falls to the saturated value while the laser intensity in the cavity builds up very rapidly when the gain is greater than the loss displaying relaxation oscillations. The magnitude of the relaxation oscillations depends upon the factor coupling fluorescence to the laser mode. However only a very small fraction of the laser energy is emitted during the unstable oscillation period.

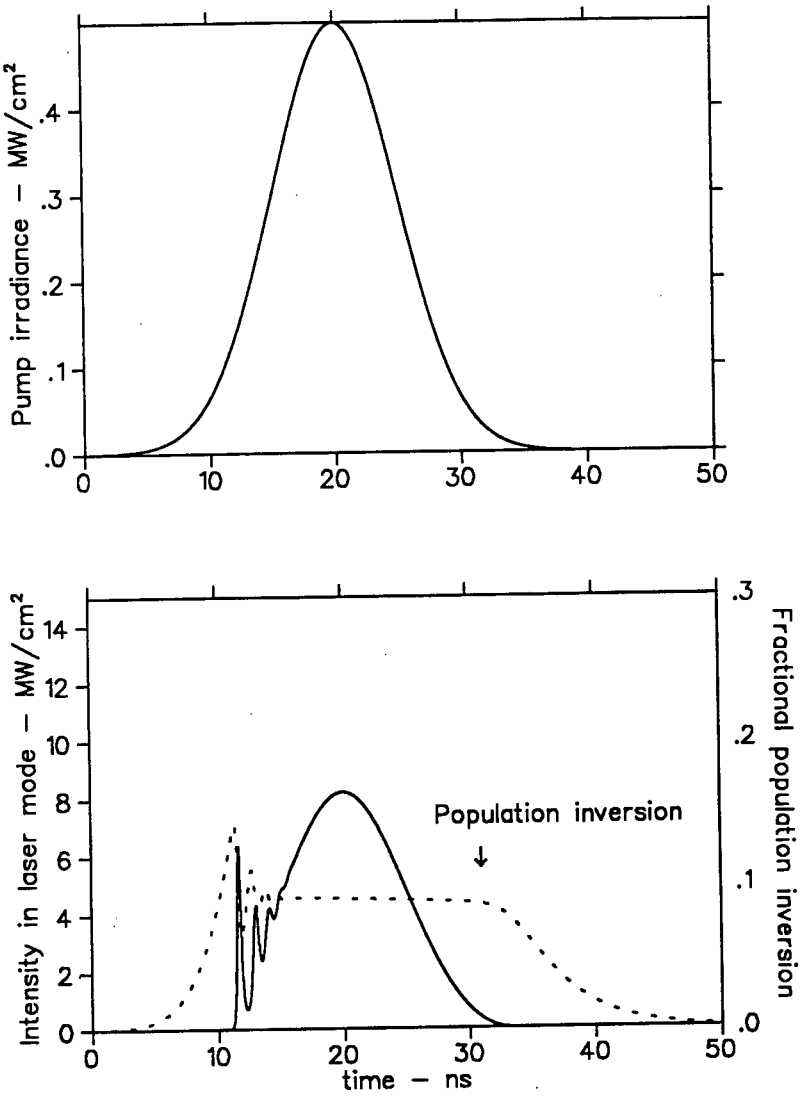

Figure 5.15: Assumed time dependence of the pump pulse (upper plot) and corresponding computed values for the population inversion and the intensity in the laser mode (lower plot) as the pump pulse develops. The parameters used in the computations were a Q-value of 1.6×10^5, a dye concentration of 10^{-4}M and a pump irradiance of 0.5MW/cm^2. β was assumed to be 10^{-4}.

5.3.6 Thresholds for laser emission

The laser threshold is reached when the gain per round trip inside the laser cavity just outweighs the losses due to leakage from the cavity, absorption, scattering out of the laser mode by imperfections in the cavity and any other loss mechanisms present. We can include all of these losses in a single value for the cavity Q; we can then express the condition for lasing (see equation 5.5) as

$$N \geq \frac{2\pi m_2}{\lambda \sigma Q} \tag{5.6}$$

N being the number density of dye molecules in the laser level. Equation 5.6 assumes no cavity QED enhancement of the stimulated transition rate in the microcavity, and violation of this condition has previously been used to place a lower limit on the enhancement factor in microdroplets [23]. We have investigated equation 5.6 by varying the dye concentration flowing in the laser cavity so as to determine the minimum concentration required to observe laser peaks in the emission spectrum at high pump intensity. The critical concentrations were determined to within a factor of 2. We can then study the validity of equation 5.6 by assuming a total population inversion, i.e. by equating the number density of dye molecules in the lasing level N with N_t, the total number density of dye molecules; this is approximately valid for a low dye concentration pumped with a short, highly intense pump beam. Results are shown for several fibers in table 5.5; the measurements were only made for the smaller fibers in order to ensure that $Q_{abs} >> Q_{ext}$, where Q_{abs} for the low dye concentrations used here is dominated by the absorption of quinoline and is of the order of 10^6. By thus restricting our investigation we also avoid the possible complications arising from spatial holeburning and effective gain reduction by supernarrow ($Q_{ext} >> Q_{abs}$) modes which may lase internally, not being observed in the emitted field due to low output coupling. We find that there is excellent agreement between the predictions of condition 5.6 and the observed critical dye concentrations, even for the smaller fibers. Results from the $2a \simeq 15\mu$m fibers are perhaps questionable as the high dye concentrations required to observe laser emission from the relatively low-Q ($Q \simeq 1000$) resonances may lead to fluorescence quenching. The good agreement between equation 5.6 and the experimental concentrations (columns 3 and

Fiber core radius	$Q_{ext}^{l=1}$-values	Observed C_{min}	Computed C_{min}	Observed I_{th} ($C = 50$mg/l)	Computed I_{th} ($C = 50$mg/l)
7.2μm	950	5000mg/l	1000mg/l	—	—
11.1μm	2.6×10^4	50mg/l	30mg/l	0.3MW/cm^2	0.4MW/cm^2
13.2μm	1.6×10^5	12mg/l	5mg/l	0.03MW/cm^2	0.05MW/cm^2
15.2μm	7×10^5	3mg/l	1mg/l	0.01MW/cm^2	0.01MW/cm^2

Table 5.5: Comparison of computed and observed minimum dye concentrations and irradiance thresholds at 10^{-4}M (50mg/l) for several different cavity sizes. The measurements were not extended to the larger core sizes because of the problems associated with determining the exact effective cavity Q-value and thresholds when solvent absorption is a significant factor.

4) imply that the bulk stimulated emission rate used in the analysis is a good approximation to the values found in a cylindrical cavity of size as small as 20μm. This is in sharp contrast to the behaviour observed in slightly smaller ($a \simeq 14\mu$m) ethanol droplets where enhancement factors of $\sim$ 120 have been reported for the stimulated transition rates for fairly broad ($Q \sim 10^3$) resonant modes. We attribute this to the lower dimensionality of the cylindrical cavity. As an example, Campillo *et al* [23] have reported evidence of lasing modes with cavity $Q_{ext} = 2600$ at a dye concentration of 10^{-5}M from 14μm diameter liquid microdroplets. In contrast, our fiber with core diameter 14.2μm and cavity $Q_{ext} = 980$ failed to lase at dye concentrations of 4×10^{-3}M at any pump intensity. We conclude that the enhancement of stimulated-emission transition rates in nonlinear optical processes at MDR's in a cylindrical geometry play a far less significant role than in liquid microdroplets, the rates appearing less by a factor of about a hundred for Q-values of the order of 10^3 for a 14μm cavity. The possibility of enhanced emissions into guided-wave modes affecting this result requires further investigation.

We have also compared the observed pump irradiance thresholds to those predicted by the numerical solution of the rate equations for two values of the dye concentration (2×10^{-3}M and 10^{-4}M) for several fibers. The results for the lower of these concentrations are summarized in table 5.5 columns 5 and 6, while com-

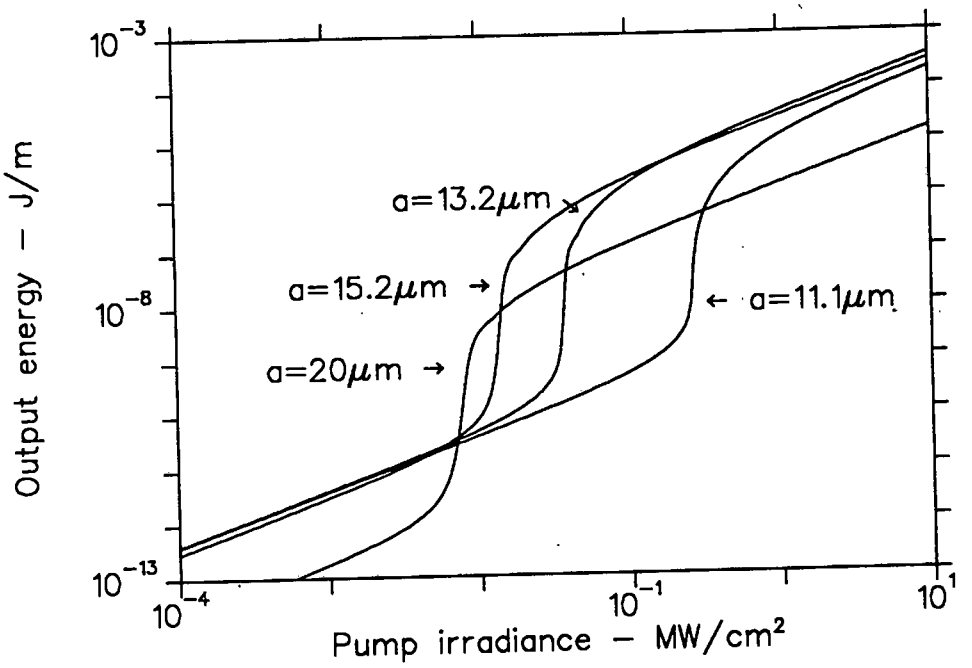

Figure 5.16: Computed values for the output energies per meter of length from the first-order resonances of several of the different fiber core sizes under increasing pump irradiance. These curves take the effect of output coupling into account: one consequence of this is that the output energy at threshold for the $a = 20\mu$m core fiber is less than for the smaller fibers, resulting in it being difficult to obtain an accurate value for this threshold experimentally. Computations assume a fluorescence coupling factor $\beta = 10^{-4}$.

puted curves showing the output energy per unit length of fiber as a function of the pump irradiance are shown for the different fibers in figure 5.16. A point to note about figure 5.16 is that the curve for the $a = 20\mu$m core fiber which has a laser threshold at the lowest pump irradiance (because of its higher Q) results in a lower output energy than the lower-Q, smaller fibers at higher pump irradiances because of its low output coupling. The exact values for the thresholds resulting from the rate equation computations and shown in table 5.5 depend to a small extent on the coupling β of the spontaneously emitted light into the laser mode, however this is not significant under the conditions of our experiments. It is worth noting several possible sources of error in the results of table 5.5; the theoretical values are dependent on the values of σ, σ_p and τ_{21} and there is some uncertainty about these

values in the literature. (For example, the values for σ at 580nm given by Svelto [160] and Hillman [76] vary by about 50%.) Also, the energy of the pump beam used in the experiments was measured using an electrically-calibrated calorimeter, which introduces some uncertainty into these values. Given these uncertainties, the agreement shown in table 5.5 is good. Similar agreement was obtained for the higher dye concentration. It is interesting to note that the thresholds observed for the larger of our core sizes at a dye concentration of 10^{-4}M are very similar to those reported by Lin and colleagues [117] for 10^{-4}M Rh6G water droplets under similar pump conditions.

Cavity QED enhancement effects in a cylindrical geometry provide an interesting alternative to studies in one-dimensional (Fabry-Perot) [75, 106] and three-dimensional (liquid droplet) cavities; as such the effective cross-section of the laser dye in these experiments warrants further experimental and theoretical investigation. These experiments have shown that the effect is substantially less than that found in liquid microdroplets.

An interesting point concerning table 5.5 is that by raising the dye concentration resonances with computed external cavity Q-values $Q < 1000$ may be brought above threshold. The widths of the observed laser peaks are $\Delta\lambda/\lambda \simeq 1.3 \times 10^{-4}$, approximately $10\times$ less than the computed theoretical zero-gain widths. This narrowing is due to the presence of gain in the core medium [101].

5.3.7 Polarization of laser emissions

Polarization effects in a lasing cylinder are easily studied experimentally, because the TM and TE modes may be isolated by the use of a linear polarizer, unlike those in a spherical microdroplet. In addition the coupling of the exciting electric vector to the electric field of the resonant modes is simpler for a cylinder, particularly for the TM case. Study of the polarization of the laser emissions from fibers of different sizes illuminated with TM or TE pump radiation shows that the laser emissions are polarized in varying degrees. The general features of the polarization are

1. for small fibers (with core diameters $\leq 40\mu$m, where the observed peaks are due to $l = 1$ modes), the emissions are strongly parallel polarized for TM pump illumination just above threshold. TM pump polarization corresponds to what would be considered s-wave polarization in a linear cavity dye laser [56] – the transition moments of the excited dye molecules are perpendicular the the cavity axis, defined in this case to be a circle of radius $r \leq a$ centered on the $\hat{z}$-axis. The observed parallel-polarized output is consistent with that expected and observed from such a configuration [56, 148]. Pumping the fiber harder results in the TE (cross-polarized) modes also being observed above threshold. The additional pump power required to bring the cross-polarized modes above threshold depends on the fiber core size: for the smaller core sizes a greater increase in the pump power is required. Indeed, for the smallest fibers (diameter $2a = 15, 20\mu$m) the cross-polarized modes are not observed above threshold even at intensities sufficient to break the fiber ($\geq 5\text{MW/cm}^2$), while for the largest fibers (see below) the cross-polarized modes appear as soon as the parallel modes. For TE pump, both TM and TE modes are observed, as expected based upon elementary considerations [56, 148] – in at least some portions of the mode volume the transition moments of the dye molecules are parallel to the cavity axis and can only be available as gain after polarization relaxation. For low intensity TE pump (just above threshold), the cross-polarized modes are the stronger, but their relative strength quickly decreases as the pump intensity is increased.

2. for larger fibers ($2a = 50, 75\mu$m), both polarizations of resonance are observed above threshold, for either pump polarization.

The variation in polarization ratio $(I_{\|} - I_{\perp})/(I_{\|} + I_{\perp})$ with increasing pump intensity described in (1) above is shown in figure 5.17 for TSP020/150 and TSP030/150 filled with 10^{-2}M Rh6G in quinoline. We have used this high dye concentration in order to obtain a strong signal at and just above the laser threshold. The plot shows that at the laser threshold the cross-polarized modes are actually stronger than those with parallel polarization for TE pump orientation. Lower dye concentrations show

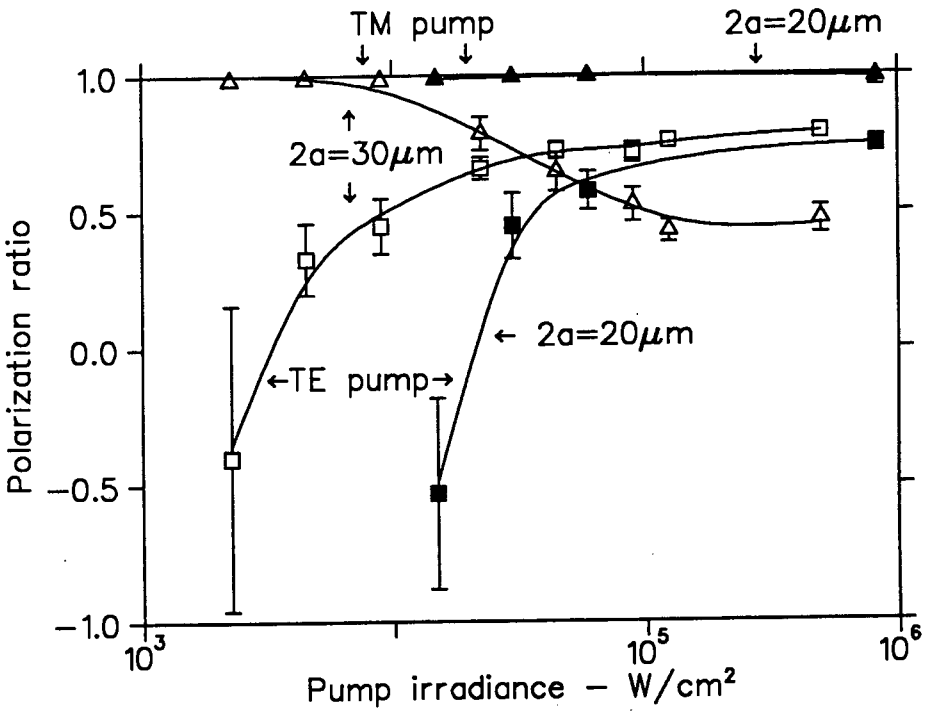

Figure 5.17: Polarization ratio as a function of the pump irradiance for $d = 20\mu$m and $d = 30\mu$m fibers filled with 10^{-2}M Rh6G quinoline, for the two pump polarizations. Error bars represent the standard deviation of the mean of thirty laser shots.

a similar trend, but do not show the polarization ratio becoming negative before the signal decreases beyond detection. The error bars represent the standard deviation of the mean polarization ratio for thirty laser shots. For TM pump, the laser emissions are strongly polarized parallel to the excitation field at all pump energies. The polarization behaviour of the 20μm core diameter fiber shown in figure 5.17 may be understood, at least qualitatively, by considering the following three facts:

1. the TM modes have slightly higher Q-values than the corresponding TE modes.

2. any dye molecule in the mode volume which is excited by a TM pump beam will by virtue of the orientation of its induced dipole moment (parallel to the cylinder axis under the assumption of isotropic polarizability) be strongly coupled to TM resonance modes, which have only a $\hat{z}$-component to their electric field; on the other hand molecules excited by a TE pump beam which have their induced dipole moment parallel to the electric vector of the internal electric field may be strongly coupled to neither polarization of resonance. This is demonstrated in figure 5.18 which shows separately the azimuthal and radial components of the TE internal electric field corresponding to a core resonance in a quinoline-filled fiber. Looking firstly at the resonant component of the field, note that this is almost entirely radial, as might be anticipated for a circumferentially travelling wave. On the other hand the off-resonant field which serves as the source function for exciting the dye molecules is seen to be dominated by an azimuthal component in the illuminated and shadow quadrants but by a radial component nearer the two sides of the fiber. (This is clearer in the upper azimuthal plot where the off-resonant source function in the core region is not obscured by the resonant field.) Thus dye molecules near to the illuminated and shadow faces will be excited with an induced dipole moment perpendicular to the electric vector of the resonant field, being consequently as strongly coupled to TM as to TE resonances.

3. the average excited-state lifetime of dye molecules in the mode volume decreases as the laser intensity increases. Below the laser threshold this lifetime is equal to the spontaneous emission lifetime of the excited dye molecule, of the

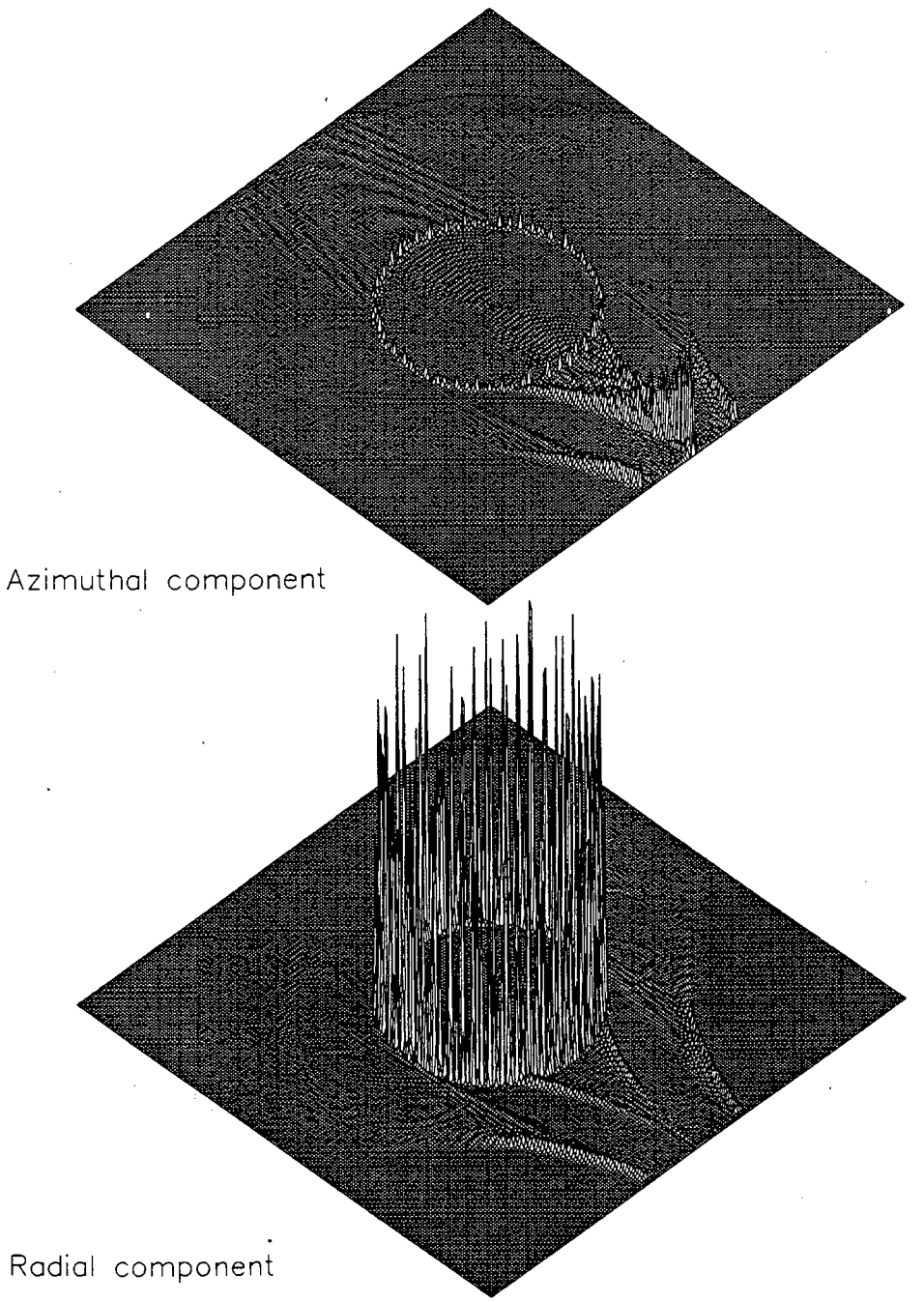

Figure 5.18: $\underline{E}.\underline{E}^*$ for the azimuthal and radial components of the internal field in a capillary fiber illuminated at a TE resonance frequency. The resonant fields are seen to be almost entirely in the radial direction, while the excitation field is azimuthally polarized in the illuminated and shadow quadrants (clearly visible in the upper plot). This has implications for the coupling between pump and laser fields, discussed in the text. The plots shown are for $m_2 = 1.626$, $m_1 = 1.458$, $a/b = 25/60$ and $x = 380.3156$, corresponding to the $l = 2$, $n = 402$ TE core mode.

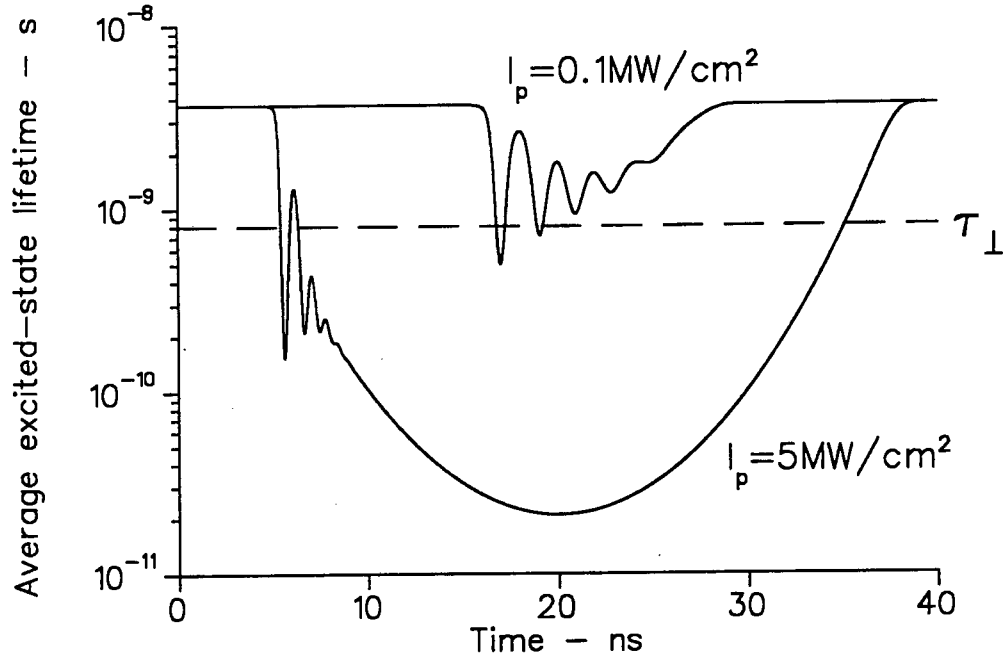

Figure 5.19: Average lifetime of an excited-state dye molecule in the laser mode volume resulting from the numerical solution of the rate equations for two values of the pump intensity, corresponding to just above threshold, and a further increase of a factor of 50. The plots show the average lifetime as the pump pulse (a 16ns gaussian pulse) develops as a function of time. The horizontal dotted line shows the value for $\tau_\perp$ given in the text.

order of 3.5ns for Rh6G. Above threshold, the lifetime decreases proportional to the number of laser photons in the cavity.

The mechanism for depolarization of excited dye molecules is rotational diffusion, and the depolarization lifetime $\tau_\perp$ for Rh6G in quinoline is not precisely known. However, a good estimate of this lifetime can be made based on the observation that the measured values for Rh6G in different solvents show a nearly linear dependence on viscosity [59]. The known viscosity of quinoline (3.95 centipoise) gives a value of the order of 0.8ns for $\tau_\perp$. The significance of this lifetime is demonstrated by the rate equation results shown in figure 5.19; these show the average excited-state lifetime for dye molecules at two different pump irradiances as the pump pulse develops. The lower intensity corresponds to a pump beam a factor of 2 above threshold, while the higher-intensity pump (lower curve) is for a further increase in the pump

by a factor of 50. For TM pump polarization, the combination of complete coupling of excited dye molecules to TM modes and their slightly higher Q-values ensure that these reach threshold first as the pump pulse develops. Thereafter, the excited-state lifetime of the dye molecules rapidly decreases below $\tau_\perp$, reducing the density of depolarized dye molecules in the mode volume. Consequently the TE modes are not expected to reach threshold. For TE pump, however, the cross-polarized modes have higher Q-values. As the excited-state population approaches threshold it is completely depolarized, the excited-state lifetime being equal to the spontaneous emission lifetime of the Rh6G (3.5ns) and the higher-Q cross-polarized TM modes reach threshold first. Nonetheless, due to the decreased coupling of these modes to the population inversion, the cross-polarised modes do not effectively saturate the gain, and the TE modes also reach threshold. As both sets of modes grow, the TE modes increasingly have an advantage over the TM modes, due to the decreasing time available for depolarization of excited-state molecules. At the same time for this pump polarization there are always spatial regions in the fiber where the excited-state lifetime is limited to a certain extent by $\tau_\perp$ (see (2) on page 129), and the TM modes never drop below threshold.

For the larger fibers the situation is not as well understood. In particular the observation of cross-polarized TE modes above threshold for the TM pump polarization even for low pump intensities is surprising, as the TM pump field is strongly coupled to the TM resonances at all points in the fiber. The presence of cross-polarized modes might perhaps be explained by the fact that the Rh6G dye molecule is not isotropically polarizable. This point requires further investigation.

5.3.8 Time dependence

We have studied the time dependence of the laser emissions from the fiber by imaging the illuminated fiber onto the entrance slit of a scanning monochromator, thereby isolating a narrow spectral region which was detected using a fast (2.7ns risetime) photomultiplier tube and a 350MHz oscilloscope. Oscilloscope traces were recorded for later analysis using a video camera while the monochromator was scanned across the laser spectrum. A reference pulse technique was used to measure the possible

delay of the observed laser emissions with respect to the excitation pulse. A reference pulse was split off the green Nd:YAG beam on the laser table and coupled into an optical fiber delay line, before being directed, suitably attenuated, onto the PM tube. This resulted in a double pulse being displayed on the oscilloscope when it was triggered, the first being the dispersed signal from the lasing fiber. The delay was calibrated using the elastically scattered light from the fiber at 532 nm. The monochromator was then tuned so as to study the laser modes from the fiber at longer wavelengths.

5.3.8.1 Low pump irradiances and dye concentrations

At very low irradiance, the observed time-dependence of the wavelength-shifted emissions was dominated by the fluorescence lifetime of Rh6G, resulting in a slightly longer pulse than the reference pulse. Increasing the pump pulse energy to just above the laser threshold (e.g. 0.02MW/cm^2 for 10^{-4}M Rh6G in TSP040/150) resulted in a substantial increase in the signal, and the time dependence showed the sharp risetime characteristic of laser action, occurring near to the center but in the first half of the pump pulse. We observed no evidence of relaxation oscillations, which have been reported several times from liquid microdroplets [102, 18, 167]; however, the $\geq$ 2.7ns resolution of our photomultiplier would probably preclude such observations. We did observe occasional irregular fluctuations in the time dependence with a period of several nanoseconds in this pump-intensity regime which we believe may be evidence of competition between the various modes of the same mode order. Increasing the pump intensity further (to perhaps 20$\times$ the threshold value) caused the time dependence of the laser emissions to follow that of the pump pulse closely, lasing being initiated early in the pulse. This behaviour is as predicted by the rate equation model.

5.3.8.2 High pump irradiance and dye concentration - thermal effects

Substantially increasing the pump intensity (to an irradiance $\sim$ 5MW/cm^2, 500$\times$ the threshold value for 10^{-4}M Rh6G quinoline in TSP040/150) resulted in a novel and unexpected observation: more laser light was emitted from the fiber during

the early part of the pump pulse than later on. Furthermore it was found that at high intensities the time-integrated spectra observed using the spectrometer/OMA displayed a small shift in peak position and asymmetrical broadening toward the shorter-wavelength side. The apparent broadening was more noticable for high dye concentrations (e.g. 2×10^{-3}M Rh6G). By studying the time delay of laser emissions from narrow spectral regions it was established that this apparent wavelength shift and asymmetrical broadening was a consequence of the laser frequency shifting towards shorter wavelengths as the pump pulse developed. Higher dye concentrations resulted in the laser emissions persisting further into the pump pulse and increased the shift and broadening of peaks.

These features are demonstrated in figures 5.20–5.24. The spectra shown in figure 5.20 were recorded with the OMA from a 30μm core diameter fiber with 2×10^{-3}M Rh6G under different pump irradiances. From about 100kW/cm^2 upwards the time-integrated spectra displayed here show a shift in the peak position and an increasing apparent broadening towards shorter wavelengths. No broadening is observed on the longer-wavelength side of the peaks. The time dependence of one of the broadened peaks is shown in figure 5.21, corresponding to the top curve in figure 5.20. The error bars on the plot indicate the FWHM of the observed pulse at different monochromator wavelength settings, while the dotted lines indicate the FWHM of the pump pulse. During the early part of the pump pulse the laser emissions occur at the same wavelength as do those observed under low pump irradiance conditions. However, these are quickly shifted towards shorter wavelengths as the pump and internal laser pulses develop. Comparing the spectral and temporal plots in figure 5.21 shows that more than half of the observed laser energy is observed during the first half of the pump pulse. The change in wavelength with time in figure 5.21 (upper plot) is approximately linear, while the halfwidths of the laser pulses stay approximately constant; therefore the observed decrease in the time-integrated spectra (lower plot) towards the shorter-wavelength side of the peak indicates that the emissions from the fiber are decreasing as the mode shifts towards shorter wavelengths. A further demonstration of the effects of high pump intensity is in figure 5.22 which shows low- and high-irradiance spectra

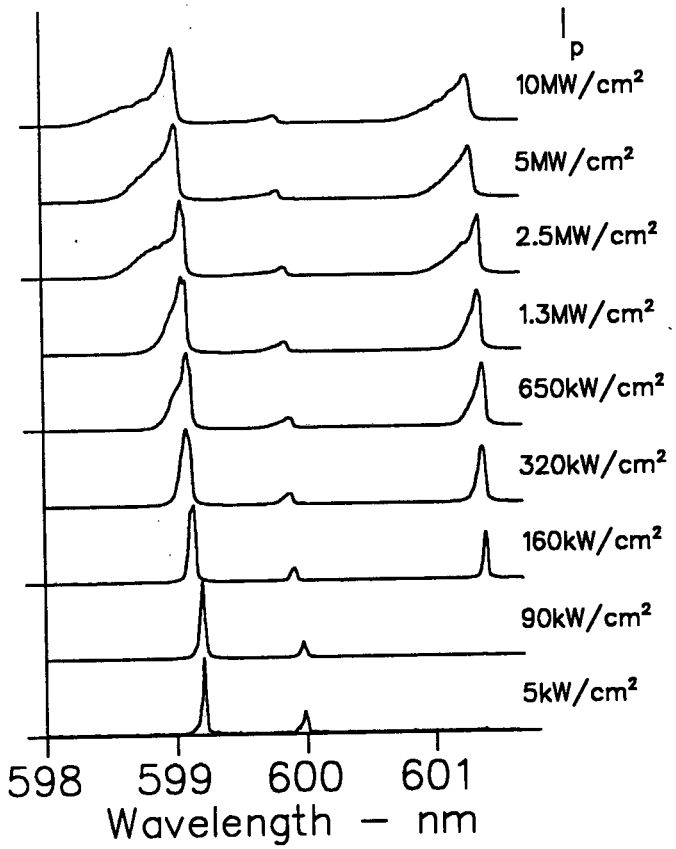

Figure 5.20: Spectra observed using the spectrometer/OMA for 2×10^{-3}M Rh6G quinoline in an $a \simeq 15\mu$m fiber under different TE illumination conditions.

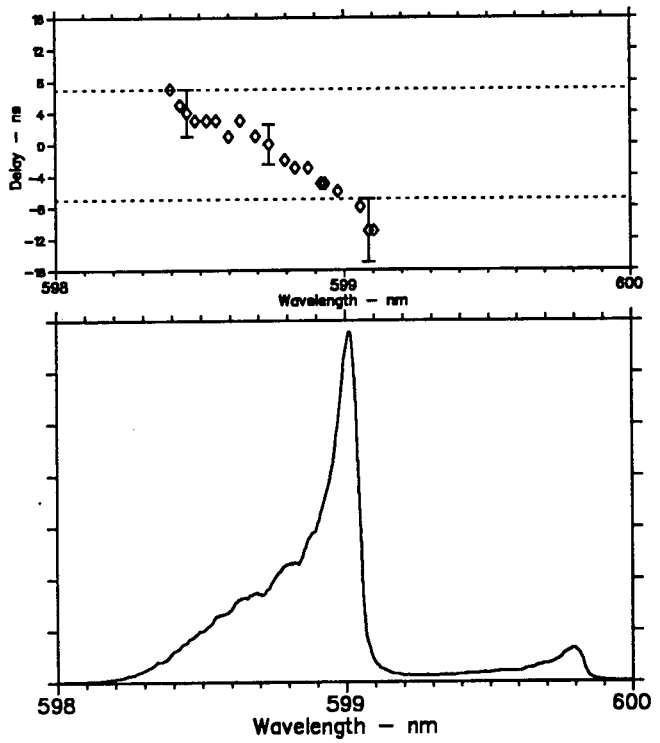

Figure 5.21: The lower plot shows a portion of the spectrum from the fiber of the previous figure under an illumination of 10MW/cm^2. The upper plot shows the measured delay of the laser emissions with respect to the center of the pump pulse. The error bars show representative full widths at half maximum for the observed laser emissions; the dotted lines show the FWHM of the pump pulse.

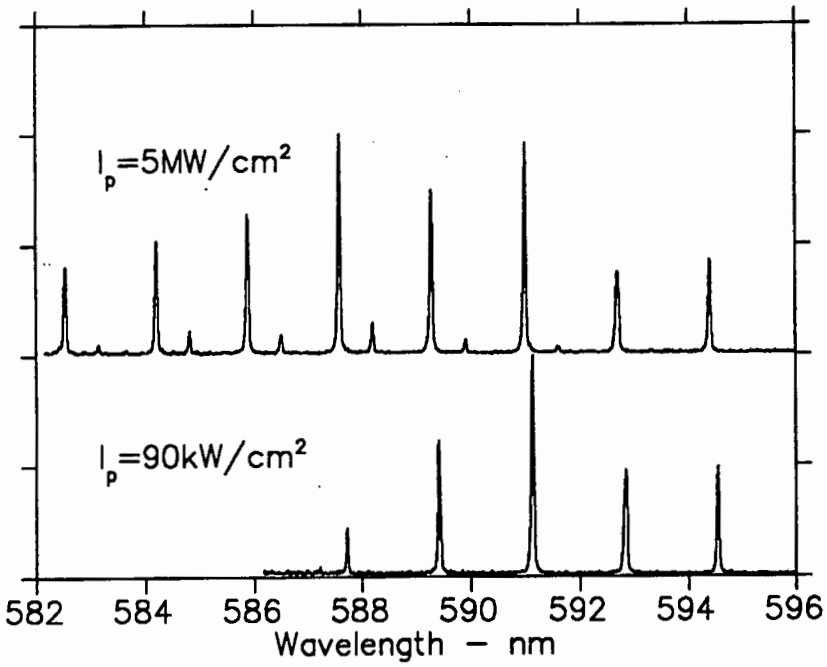

Figure 5.22: Laser spectra observed from a lower dye concentration (2×10^{-4}M Rh6G) in a $2a \simeq 40\mu$m fiber illuminated at low and higher pump irradiances. Significantly less broadening of the laser peaks is observed (although the laser emission still occurs mainly in the first part of the pump pulse). The time-integrated spectra show the peaks displaced towards shorter wavelengths at the higher pump irradiance. (The two spectra are independently scaled for comparison.)

recorded using the spectrometer/OMA from a lower dye concentration (2×10^{-4}M Rh6G) in a 40μm core diameter fiber. Significantly less broadening is observed but the time-integrated spectra show a shift towards shorter wavelengths at the higher pump irradiance. Another feature of the high-pump spectra is shown in figure 5.23, showing spectra recorded from the same fiber as in figure 5.22, but at a higher dye concentration (2×10^{-3}M Rh6G). Two new and broader peaks appear on the shorter wavelength side of the first-order modes. The time dependence of one of these clusters of peaks is shown in figure 5.24, which shows that these new peaks occur as the first-order modes are shifted to shorter wavelengths. The new peaks do not build up from noise as separate laser modes but appear when the first-order modes move across a spectral region where additional feedback is provided. This is what gives the spectrum the 'clustered' appearance. The discontinuities in the time

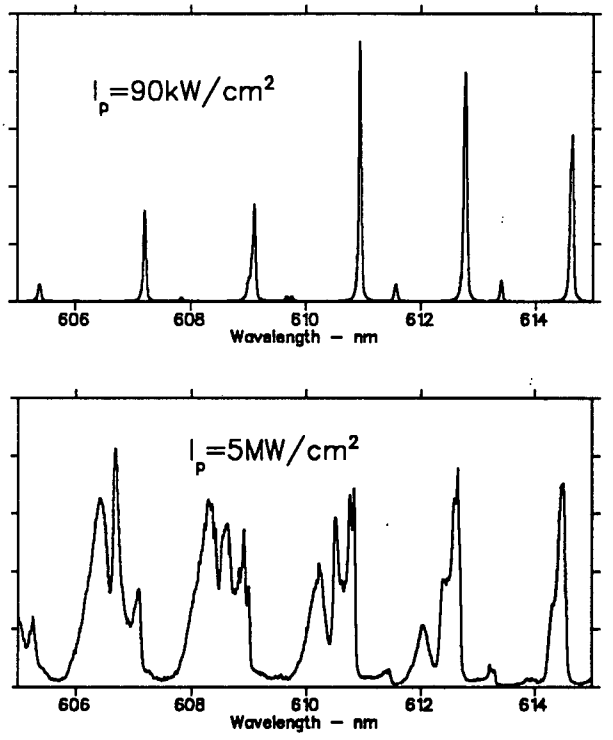

Figure 5.23: A portion of the spectra observed from a high dye concentration (2×10^{-3}M) in the same fiber as the previous figure, under low and high pump irradiance. Laser emission now occurs at a longer wavelength as a result of the higher dye concentration. On increasing the pump irradiance two new broader series of peaks appear on the shorter wavelength side of the $l = 1$ modes.

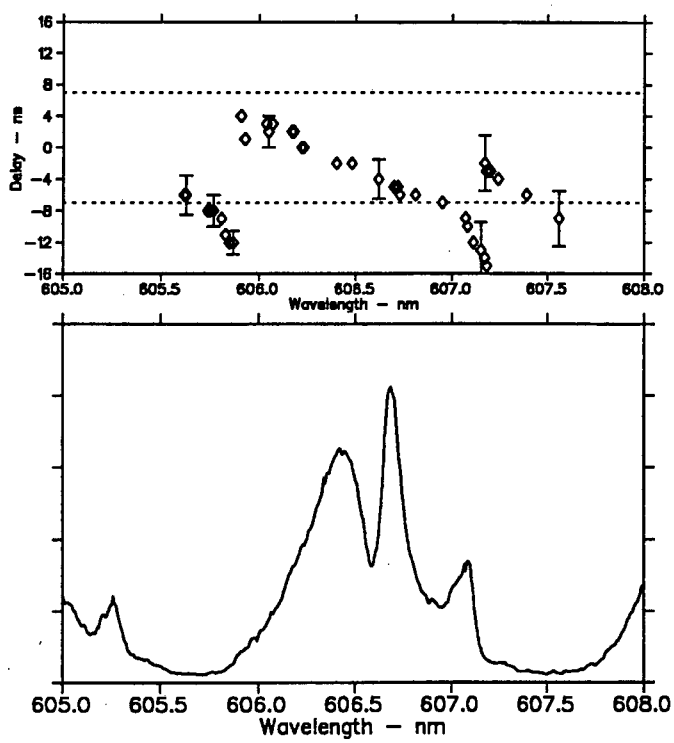

Figure 5.24: The time dependence of the spectral region from 605 – 608nm in the previous figure. Again most of the observed emissions occur in the first half of the pump pulse. The original peaks and the new, broader peaks are seen to appear consecutively as the laser emission is swept towards shorter wavelengths. The discontinuitites in the time dependence at 605.9nm and at 607.2nm correspond to the positions of the cross-polarized modes appearing in the low-irradiance spectrum.

dependence at 606nm and at 607.9nm correspond to the cross-polarized first-order modes appearing in the low-intensity spectrum. The apparent mode broadening under the conditions of figures 5.21 and 5.24 is such that laser light appears at all wavelengths in the range 600-620nm.

The observed effect cannot be due to the intensity-dependent refractive index (which would cause an increase in the effective refractive index, shifting resonances toward longer wavelengths), and is not the result of damage to the cavity or the catastrophic formation of a laser-induced plasma. We believe that the features demonstrated in figures 5.20–5.24 are due to laser heating of the dye solvent as the pump pulse and the internal laser pulse develop. Laser-induced heating of a dye-doped liquid droplet has previously been investigated by Chen *et al.* [28]; however it was found not to be a dominant process in their study of laser-induced radiation leakage from a droplet. Numerical estimates of the heating effects in a cylindrical dye microlaser are perhaps easier to obtain than in a liquid droplet because of the greatly reduced QED enhancement factors in the cylindrical case, enabling more precise estimates of the saturated population inversion for a mode of a given computed external Q-value. The heating of the dye solvent reduces the refractive index of the solvent, shifting the resonances towards larger x (smaller wavelength) while reducing the Q-values. There are several possible sources of laser heating to be considered, which differ somewhat depending on whether the region of interest corresponds to the laser mode volume (near to the core surface) or not. In what follows we shall describe the effects separately for these two regions: practically there is no clearly defined boundary between the two but clearly the laser mode volume arguments will apply to those regions where the radial mode function of the lasing mode order is near to its maximum (see e.g. figure 3.17). Under the conditions in which these effects are observed there are several modes with differing n above threshold, resulting in only a radial dependence in the population inversion.

In the laser mode volume the gain is saturated, with $N_2 = 2\pi m_2/\lambda\sigma Q$ dye molecules per unit volume in the upper lasing level. We assume that the remainder of the dye molecules are in the ground state, absorbing pump radiation with an absorption coefficient $\alpha = N_g\sigma_{S_1\leftarrow S_0}(\omega_p)$. Assume that any excited dye molecule

$\sigma_{S_1 \leftarrow S_0}(\omega_p)$	$3.8 \times 10^{-20}\mathrm{m}^2$
$\sigma_{S_2 \leftarrow S_1}(\omega_p)$	$4 \times 10^{-21}\mathrm{m}^2$
$\sigma_{S_2 \leftarrow S_1}(\omega_l)$	$1 \times 10^{-21}\mathrm{m}^2$

Table 5.6: Cross-sections for ground-state and excited-state absorption for Rhodamine 6G for $\lambda_p = 530\text{nm}$ and $\lambda_l = 580\text{nm}$.

will eventually decay back to the ground state radiatively, with efficiency $h\nu_l/h\nu_p$. (We neglect the possibility of decay to the triplet state as the lifetime for such decay is far longer than the duration of the pump or laser pulses under consideration.) The molecules in the upper laser level may be further excited by either the pump or the laser field to the second excited state, whence they quickly decay nonradiatively back to the laser level. The total energy per unit volume deposited in the mode volume may thus be written

$$\Delta E = \epsilon N_g \sigma_{S_1 \leftarrow S_0}(\omega_p) I_p \Delta t + N_2 \left[\sigma_{S_2 \leftarrow S_1}(\omega_p) I_p \Delta t + \sigma_{S_2 \leftarrow S_1}(\omega_l) I_l \Delta t\right] \qquad (5.7)$$

where ϵ is the fraction of the absorbed pump energy which is not emitted radiatively, and which remains in the dye laser medium as heat $(\nu_p - \nu_l/)\nu_p$. Outside of the mode volume where the cavity Q is small the dye molecules will spend most of their time in the upper lasing lasing level for high pump irradiance. Excited-state absorption of the pump beam will therefore be a major contributor to thermal heating. We express the thermal energy transferred in this region as

$$\Delta E = \epsilon \frac{\Delta t}{\tau_{21}} h\nu_p N + N\sigma_{s_2 \leftarrow S_1}(\omega_p) I_p \Delta t \qquad (5.8)$$

Hence the heating rates corresponding to the lasing and non-lasing regions differ, and modes above and below threshold will be affected differently by the heating effect. Values for the cross-sections of Rhodamine 6G are given by Hillman [76] for $\lambda_p = 530\text{nm}$ and $\lambda_l = 580\text{nm}$: these are shown in table 5.6. Values for the refractive

C M	I_p MW/cm^2	Q	N_g m^{-3}	N_2 m^{-3}	I_l/I_p	ΔT_{las} °C	ΔT_{flu} °C	Δn_{las}
2×10^{-3}	5	2×10^5	1.2×10^{24}	0.6×10^{22}	450	3.7	2.5	−0.0019
2×10^{-4}	5	2×10^5	1.14×10^{23}	0.6×10^{22}	45	0.37	0.25	−0.00019

Table 5.7: Laser heating of the dye solvent during a single 14ns irradiating pulse.

index change upon irradiation can be calculated from equations 5.7 and 5.8 using

$$\Delta n = \frac{\partial n}{\partial T} \frac{\Delta E}{C_p \rho} \tag{5.9}$$

$C_p\rho$ for quinoline is $1.5 \times 10^6 \mathrm{Jm}^{-3}K^{-1}$, while $\partial n/\partial T = -5 \times 10^{-4}K^{-1}$. Some numerical values corresponding to the experimental conditions of figures 5.20-5.21 are given in table 5.7. The values for N_2 and I_l/I_p are calculated using the rate equation approach. The calculated values for the temperature changes in the illuminated fiber result in refractive index changes of the order of $\Delta n \simeq 0.002$ for dye concentration $C = 2 \times 10^{-3}$M. The mode shifts corresponding to such a change in refractive index are easily calculated to be of the order of 0.7nm for a homogeneous fiber; the corresponding changes in mode locations and Q-values for the inhomogeneous refractive indexes resulting from our analysis are not as easily computed, but can be expected to be of the same order of magnitude, in excellent agreement with the observed shifts. Exact computations would have to take into account the different temperature changes in the lasing and nonlasing regions: Chowdhury and co-workers have shown how this can be done for a spherical particle [38]. The temperature variation in table 5.7 scales approximately linearly with dye concentration for a given pump intensity, and the lower concentration values in table 5.7 also agree well with the observed spectral shift shown in figure 5.22. The reduction of the refractive index decreases the cavity Q-value as well as shifting the resonant modes towards shorter wavelengths. For the higher dye concentration above, homogeneous-fiber computations suggest that this reduction is of the order of 20%. This is not sufficient to

explain the termination of the laser emissions from the high-Q cavity modes shortly after the peak of the pump pulse or the fact that the emissions are already substantially reduced even before the pump pulse has reached its peak (see figures 5.21 and 5.24). This can be explained by the rapid change of the resonant wavelength with time as the solvent heats up during the pump pulse; consequently there is insufficient time for the cavity resonance to build up before the resonant frequency changes. This will begin to be significant when the resonance wavelength changes by about one halfwidth due to heating during an interval of one cavity lifetime.(The lifetime of a resonant mode is $\tau_r = Q/\omega$ [39].) For a cavity Q-value of 2×10^5 this requires a wavelength shift of $\partial\lambda/\partial t \simeq 0.05$nm/ns. The observed slope of the delay in e.g. figure 5.24 is $\partial\lambda/\partial t > 0.1$nm/ns, consistent with such an explanation.

Due to the fact that the temperature increase at a specific location inside the fiber core depends on the modal field strength at that point the inhomogeneous temperature distribution inside the fiber core can result in different effective refractive indexes for modes of different order. Consequently different mode orders may be shifted by differing amounts, those which have the highest Q-values being affected the most. Hence as the pump pulse develops, high-Q modes may be shifted across resonant modes of a higher order. We believe that the additional feedback provided when the two modes are coincident may be responsible for the appearance of broader peaks superimposed on the asymmetrically broadened peaks from our larger fibers (see e.g. figure 5.23). The appearance of two new broader peaks in the 40μm core diameter fiber is consistent with the computed modal Q-values for this fiber, for which the $l = 2$ and $l = 3$ mode orders have $Q_{ext} \simeq 5 \times 10^4$ and 2×10^3 respectively. Such additional peaks are not observed for small fibers, for which the second- and subsequent-order modes have very low Qs. It should be noted that the simple heating analysis given above predicts large heating effects for lasing microdroplets under highly intense pump irradiation, even for low or moderate dye concentrations. Typically, pump irradiances used in the study of pulsed lasing microdroplets are several orders of magnitude higher than those used in this study.

5.4 Characterization of core size and taper using core-resonance laser emission

It has been shown in section 5.3.3 that the observed mode spacing for a given resonance order l contains information about the size of the capillary fiber core. We have used scanning electron microscope images of several cleaved fiber tips to verify that the fibers sizes fall within the manufacturers tolerances. Hence we have shown that the observed mode spacings may be used with knowledge of the refractive index and dispersion of the core and cladding media to determine the size of the fiber core. The accuracy of this determination is limited in practice by the knowledge of the refractive index and dispersion of the liquid solvent; in our case such uncertainties amounted to between about one half and two percent, depending on the size. The possibility of anomalous dispersion due to the presence of gain in the fiber core remains to be investigated: we consider this unlikely because the saturated gain for large-Q resonances is small, and no such effects have been observed in liquid droplets [62]. This possibility could be investigated by more careful calibration and analysis of electron microscopy images of the capillary fiber core.

Highly accurate measurements can be made of the variation in the core size along a length of fiber using the laser spectrum. We have done this by translating a fiber vertically, successively imaging the laser emissions from different points on the capillary fiber onto the entrance slit of the spectrometer. The observed shift in the wavelengths of laser peaks with changing position on the fiber reflects the changing cavity size. In the case of zero dispersion the fractional change in core size is simply equal to the fractional change in laser wavelength: $\Delta a/a = \Delta\lambda/\lambda$, and this relation has previously been used to monitor evaporation and condensation rates of liquid droplets flowing in a stream. The effects of dispersion may be modelled as in section 5.3.3; the result is

$$\frac{\Delta a}{a} = \frac{\Delta\lambda}{\lambda}\left(1 - \frac{K_2\lambda}{m_2}\right) \tag{5.10}$$

the correction factor being greater than unity for normal dispersion. A set of spectra recorded at 2mm intervals from a length of TSP050/192 is shown in figure 5.25. The corresponding values for the changes in the core size along the length calculated

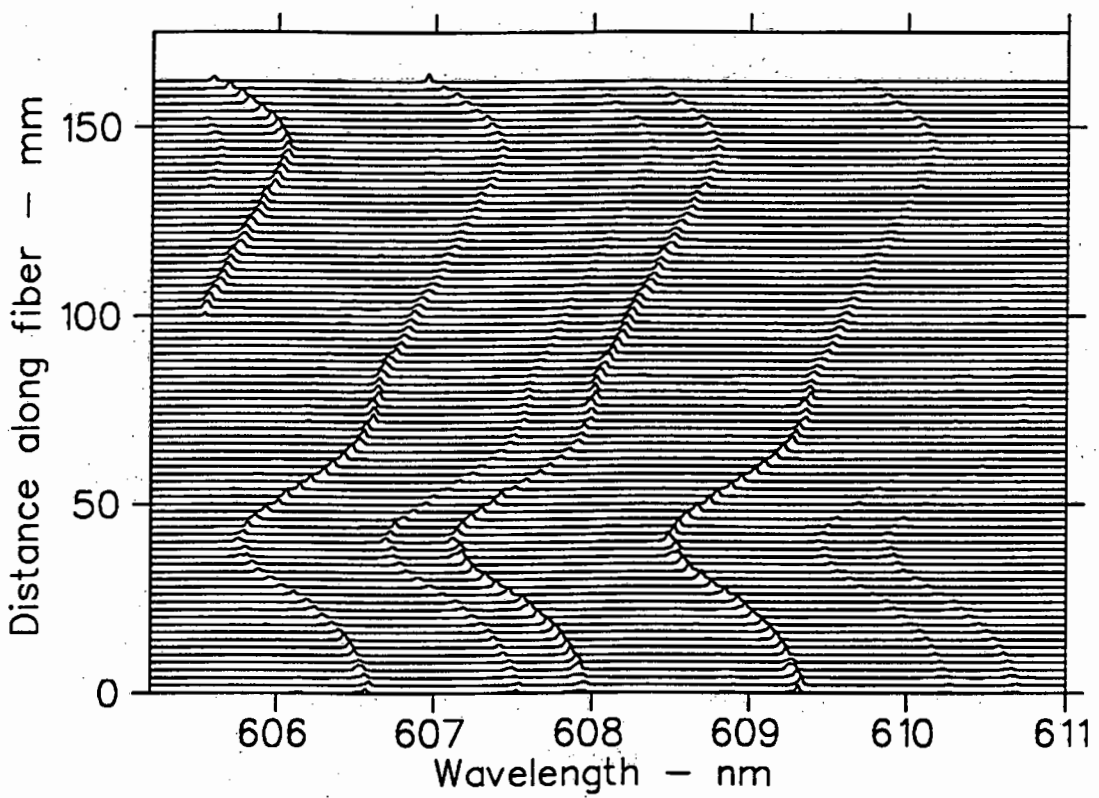

Figure 5.25: Spectra recorded at 2mm intervals from 2×10^{-3}M Rh6G in quinoline flowing in a length of fiber with nominal core diameter $2a = 50\mu$m. The observed shifts of the modal wavelengths correspond to changes in the cavity size.

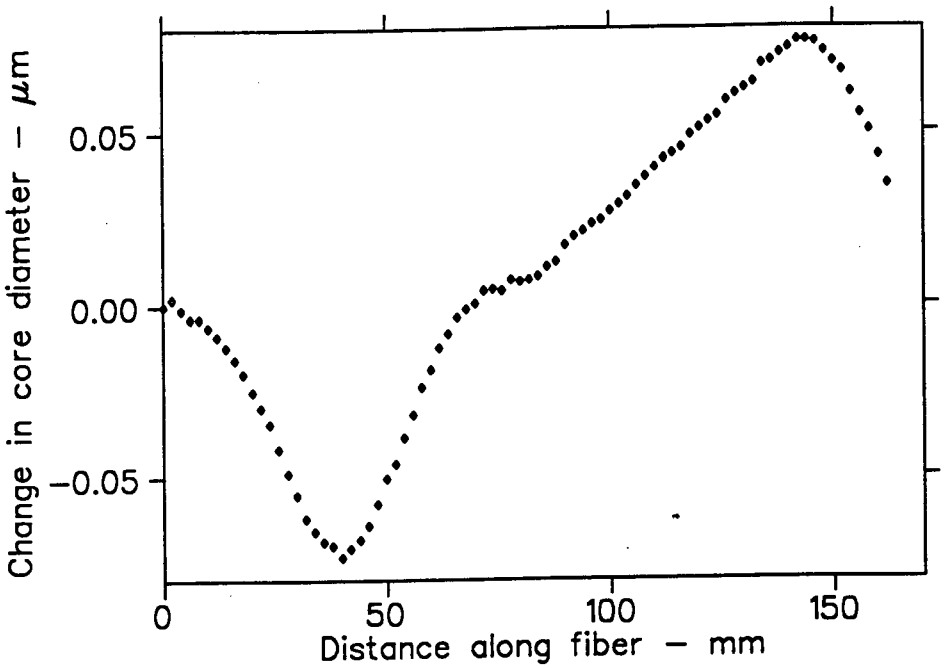

Figure 5.26: Changes in the core diameter corresponding to the spectra shown in the previous figure.

using the observed spectral shifts, the value for the core size computed using the mode spacing and equation 5.10 are shown in figure 5.26. Changes of the order of a few parts in 10^5, corresponding in the present case to changes of 2 or 3nm in the nominally 50μm core diameter are easily detected. The average taper of the core is of the order of 1nm/mm - clearly such a small change must be interpreted as a change in the average size. An interesting feature of the result shown in figure 5.26 is the change in the sign of the taper at the two ends. This piece of fiber was cut by the manufacturers to a length of $\simeq$ 170mm. The one cut end is within a millimeter of the zero distance point on the graph: the other end was embedded in the dye reservoir approximately 2–3mm from the last data point. Similar changes in the sign of the taper near to the tips of the fiber have been observed in the other lengths of fiber supplied by the manufacturer, while no such changes are observable near the tip of a fiber which is snapped or crushed. We believe that this effect may be due to stresses set up in the fiber during either the manufacturing or the cutting process.

Chapter 6

Summary, conclusions and suggestions for further work

Elastic scattering computations We have rederived the boundary-value solution to the problem of the elastic scattering of a plane electromagnetic wave incident normally on a layered dielectric cylinder and have developed computer programs to evaluate the resulting equations for the internal and external electromagnetic fields for given values of the core and cladding radii a and b and the corresponding complex refractive indexes m_2 and m_1. The programs have been used to evaluate these fields for size parameters up to $x \simeq 700$; where possible results have been compared to published values, giving good agreement in all cases. The general features of the internal and scattered fields can be understood as extensions of the known scattering characteristics of a homogeneous cylinder. The main features of the internal and external near-field patterns have been explained using a geometrical-optics approach while the interference fluctuations in the computed extinction efficiency are well predicted by an anomalous-diffraction theory for a range of core and cladding indexes.

The nature of optical whispering-gallery-mode resonances in a layered fiber has been investigated by studying resonant internal field patterns. We reach the following conclusions:

1. For small core sizes ($a < b/m_1$) and if $m_2 < m_1$ the resonance spectrum of the

composite fiber is identical to that of a homogeneous fiber with $m = m_1$. The resonance locations and Q-values are unaffected by the exact size or refractive index of the fiber core.

2. If $a << b/m_1$ and $m_2 > m_1$ additional modes may appear in the resonance spectrum corresponding to excitation of the cavity formed by the fiber core. These appear for increasingly smaller core sizes as the relative refractive index of the core increases. The locations and Q-values of these resonances are approximately those of a homogeneous fiber of refractive index m_2/m_1 and radius a illuminated with light of wavelength λ/m_1. However these are modulated slightly by their interaction with the low-Q feedback provided by internal reflections from the external surface of the fiber.

3. For $b > a > b/m_1$ the resonance spectrum differs from that of a homogeneous cylinder, the degree of change depending on the refractive index difference between the core and the cladding. Resonances are shifted towards smaller x and narrowed if $m_2 > m_1$, and *vice versa.*

4. For $a \simeq b/m_1$ resonances are more strongly affected for $m_2 > m_1$ than for $m_2 < m_1$ as in this case additional feedback into the cavity is provided by the core/cladding interface.

Fluorescence from a layered fiber The model of Chew *et al.* for inelastic light scattering from a molecule in a cylindrical dielectric particle has been extended to allow for the possibility of a layer of differing refractive index on the cylinder. We find that the model predicts that the signal from a collection of molecular fluorescent centers in a capillary core is proportional to the number of scatterers when neither the illuminating nor the emitted frequencies are resonant. We have used the extended model to investigate the effects of the various resonant configurations on the fluorescence from a liquid in a capillary fiber. If the capillary has thin walls, or if the solvent in the core region has a higher refractive index than that of the walls, resonance enhancement of the fluorescence process can occur, resulting in large spectrally narrow peaks in the fluorescence spectrum. The origin of these peaks is the

enhancement of the molecular transition rates at resonant frequencies as a result of the increased density of final states.

Laser emission corresponding to core whispering-gallery modes By passing quinoline doped with the laser dye Rhodamine 6G through a fused-silica capillary fiber and illuminating it normally with a frequency-doubled Nd:YAG laser beam we have observed laser emission from the dye at wavelengths corresponding to the high-Q resonances of the cavity formed by the fiber core. The laser emission is emitted in all directions in a plane perpendicular to the fiber axis. The spectral characteristics of the laser emission are well explained by the computed modal Q-values and by the optical properties of the bulk dye solution. The spacing between modes with the same radial mode number and with azimuthal mode number differing by one follows from the computed resonance spacing when the effects of dispersion are properly accounted for. The effect of the interference modulation of the core resonance Q-values is to modulate the strengths of the observed laser peaks, particularly for the TM modes. For large fibers more than one set of laser peaks may be observed, corresponding to different orders of resonance with differing radial mode numbers.

We have used a simplified rate equation analysis based on a four-level laser scheme for a dye laser to predict critical dye concentrations and pump intensity thresholds in fibers of different core sizes. We find that the results are in good agreement with observations when the bulk cross-sections of the laser dye are used in the analysis. From this we conclude that the cavity quantum electrodynamic enhancement of the cross-sections is not as significant in a cylindrical as in a spherical geometry, which is expected due to the lower dimensionality of the cavity. A theoretical treatment of the transition rates in a cylindrical cavity is needed before this result can be fully understood - the possibility of enhanced emissions into guided-wave modes, which would reduce the gain for whispering-gallery modes, requires investigation. Polarization studies are simpler in a cylindrical than in a spherical geometry both because of the better coupling of the pump and laser fields via the induced dipole moment and because the two sets of modes are easily identifiable experimentally by the use of a linear polarizer. Several features of the polarization

of the laser emissions can be explained, at least qualitatively, in terms of the depolarization lifetime of excited dye molecules in solution, the decrease in the average excited-state lifetime of dye molecules with increasing laser power and the differing Q-values of the laser modes. On the other hand the appearance of cross-polarized modes under high-intensity TM pump irradiance is not fully understood and merits further investigation. The extension of these polarization studies to the slightly more complex case of a lasing microdroplet and a comparison of the polarization characteristics of the lasing with those of SRS from a microdroplet would be interesting.

We have observed a shift of laser modes towards shorter wavelengths during the evolution of the pump and internal laser pulses, particularly for high dye concentrations and pump intensities. We believe that this is a manifestation of heating of the dye solvent by the intense fields at the pump and laser wavelengths, which alters the refractive index and hence the resonant mode frequencies of the laser cavity. The observed spectral shift is consistent with a temperature increase of several degrees predicted by a simple analysis of the heating effect of pumped Rh6G dye molecules. The heating rates are different for those regions of the core which are above threshold (in the mode volume near to the core surface) and those regions which are not, resulting in a radially varying refractive index profile developing during the laser pulse. Hence modes which are above and below threshold (with different modal field pattterns) will be affected differently by the heating. It would be interesting to study this effect using a train of mode-locked pulses to confirm the cumulative nature of the effect. Another possibility would be to attempt to vary the heating rate in the fiber by the addition of some suitable absorber to the dye-doped solvent. It is worth considering the possibility of similar effects occurring in lasing microdroplets.

We have not attempted to explain the number of laser peaks observed above threshold for the different fibers, pump intensities and dye concentrations. Such an explanation would require a dynamical treatment of spatial hole-burning of modes with different azimuthal mode numbers. However a clear trend has emerged from our experimental data of more modes of the same radial mode number being observed above threshold for the larger fibers; this may be a consequence of the larger

azimuthal mode numbers and hence more complex resonant internal field configurations for these fibers, or due to the shapes of the absorption and gain curves at the shorter or longer wavelengths where the smaller or larger fibers respectively lase, or simply due to the mode spacing. Another point of interest is the length along the lasing fiber for which the internal laser field is coherent. The internal fields build up from fluorescent noise at the laser frequency - essentially from a single photon. However, the internal field can only be coherent over a finite length of fiber which may be limited by the fiber taper or by the finite time for a laser mode to spread coherently along the length of the fiber, which might require many round trips. Our measurements of the fiber core taper, which were easily made with a high degree of accuracy by recording core resonance laser spectra from different points along a length of fiber, suggest that it would limit this length to the order of 1mm for narrow ($Q = 10^5$) modes. However competition between laser fields at the same frequency with different phases initiated at different points along the pumped length could limit this length to substantially less than this. By isolating the emissions from a short length of fiber such that the emissions from the length are coherent it may be possible to detect the angular fine structure in the emissions from a single mode. To our knowledge such fine structure has not previously been observed in the emissions from a whispering-gallery-mode laser. Such an observation could confirm the assignment of mode numbers to laser peaks by providing a direct measurement of the azimuthal mode number n.

The possibility of high-Q whispering-gallery modes needs to be considered in the design of fiber lasers and fiber laser amplifiers for optical communications, where such modes could result in whispering-gallery-mode lasing and consequent loss of gain for travelling waves. Such modes could be suppressed by choice of suitable parameters for the fiber size and relative refractive index.

The capillary-fiber laser described in this thesis provides a useful means of studying the resonance spectrum of a coated microparticle experimentally, which might be relevant in any application requiring a protective coating on a microparticle laser. Coated microparticles might also be a means of creating a bulk medium consisting of a large number of independent microparticle cavities. The very small amount of

laser dye required for operation ($1cm^3$ of dye-doped solvent is sufficient for several hours of laser operation) and the predictable and consistent laser operation might make the system useful for investigating the laser characteristics of dyes. We believe that further theoretical and experimental study of this cylindrical laser is warranted as it provides an ideal test for certain aspects of laser processes in whispering-gallery-mode lasers.

Bibliography

[1] *Handbook of Mathematical Functions*, M. Abramowitz and I. Stegun, Eds., Dover, New York (1972)

[2] D. Abromson and W.S. Bickel, "Fluorescent angular scattering emissions from dye-filled fibers", Appl. Opt. **30** 21 2980-2984 (1991)

[3] W.P. Acker, D.H. Leach and R.K. Chang, "Third-order optical sum-frequency generation in micrometer-sized liquid droplets", Opt. Lett. **14** 8 402-404 (1989)

[4] W.P. Acker, A. Serpengüzel, R.K. Chang and S.C. Hill, "Stimulated Raman Scattering of Fuel Droplets", Appl. Phys. B **51** 9-16 (1990)

[5] A.L. Aden and M. Kerker, "Scattering of Electromagnetic Waves from Two Concentric Spheres", Journ. Appl. Phys. **22** 1242-1246 (1951)

[6] G. S. Agarwal and S. Dutta Gupta, "Spherical microstructures for the study of strong coupling between radiation and matter", Opt. Commun. **9** 3 173-178 (1992)

[7] *American Institute of Physics Handbook*, 3rd edition, D.E. Gray, ed., McGraw-Hill, New York (1972)

[8] R.L. Armstrong, J.-X. Gie, T. E. Ruekgauer, J. Gu and R.G. Pinnick, "Effects of submicrometer-sized particles on microdroplet lasing", Opt. Lett. **18** 2 119-121 (1993)

[9] S. Arnold, J. Comunale, W.B. Whitten, J.M. Ramsey and K.A. Fuller, "Room-temperature microparticle-based persistent hole-burning spectroscopy", Journ. Opt. Soc. Am B **9** 5 819-824 (1992)

[10] S. Arnold, D.E. Spock and L.M. Folan, "Electric-field-modulated light scattering near a morphological resonance of a trapped aerosol particle", Opt. Lett. **15** 20 1111-1113 (1990)

[11] A. Ashkin, "Applications of Laser Radiation Pressure", Science **210** 4474 1081-1088 (1981)

[12] A. Ashkin and J.M. Dziedzic, "Observation of Resonances in the Radiation Pressure on Dielectric Spheres", Phys. Rev. Lett. **38** 23 1351-1354 (1977)

[13] A. Ashkin and J.M. Dziedzic, "Observation of optical resonances of dielectric spheres by light scattering", Appl. Opt. **20** 10 1803-1814 (1981)

[14] A. Ashkin, J.M. Dziedzic and R.H. Stolen, "Outer diameter measurement of low birefringence optical fibers by a new resonant backscatter technique", Appl. Opt. **20** 13 2299-2303 (1981)

[15] P.W. Barber, J.F. Owen and R.K. Chang, "Resonant Scattering for Characterization of Axisymmetric Dielectric Objects", I.E.E.E. Trans. Antennas Propag. **AP-30** 2 168-172 (1982)

[16] D.S. Benincasa, P.W. Barber, J.-Z. Zhang, W.-F. Hsieh and R.K. Chang, "Spatial distribution of the internal and near-field intensities of large cylindrical and spherical scatterers", Appl. Opt. **26** 71 348-1356 (1987)

[17] R.E. Benner, P.W. Barber, J.F. Owen and R.K. Chang, "Observation of Structure Resonances in the Fluorescence Spectra from Microspheres", Phys. Rev. Lett. **44** 7 475-478 (1980)

[18] A. Biswas, H. Latifi, R.L. Armstrong and R.G. Pinnick, "Time-resolved spectroscopy of laser emission from dye-doped droplets", Opt. Lett. **14** 4 214-216 (1989)

[19] C.F. Bohren and D.R. Huffman, *Absorption and Scattering of Light by Small Particles*, Wiley, New York (1983)

[20] H. Born and E. Wolf, *Principles of Optics*, Pergamon, Oxford (1959)

[21] S.D. Brorson, H. Yokoyama and E.P. Ippen, "Spontaneous Emission Rate Alteration in Optical Waveguide Structures", I.E.E.E. Journ. Quantum Electron. **26** 9 1492-1499 (1990)

[22] H.E. Bussey and J.H. Richmond, "Scattering by a Lossy Dielectric Circular Cylindrical Multilayer, Numerical Values", I.E.E.E. Trans. Ant. Propag. **AP-23** 723-725 (1975)

[23] A.J. Campillo, J.D. Eversole and H.-B. Lin, "Cavity Quantum Electrodynamic Enhancement of Stimulated Emission in Microdroplets", Phys. Rev. Lett. **67** 4 437-440 (1991)

[24] R.K. Chang, "Some of Bloembergens nonlinear optical effects revisited in single micrometer-sized droplets" in *Resonances*, M.D. Levenson, E. Mazur, P.S. Pershan and Y.R. Shen, Eds., World Scientific, Singapore (1990)

[25] R.K. Chang, G. Chen, S.C. Hill and P.W. Barber, "Nonlinear optical processes in droplets with single-mode laser excitation", SPIE **1497** - Nonlinear Optics and Materials, 2-13 (1992)

[26] R.K. Chang, J.F. Owen, P.W. Barber, B.J. Messinger and R.E. Benner, "Inelastic Light Emission from Spherical Particles and Cylindrical Fibers", Journ. Raman Spectrosc. **10** 178-182 (1981)

[27] G. Chen, W.P. Acker, R.K. Chang and S.C. Hill, "Fine structures in the angular scattering distribution of stimulated Raman scattering from single droplets", Opt. Lett. **16** 3 117-119 (1991)

[28] G. Chen, D.Q. Chowdhury, R.K. Chang and W.-F. Hsieh, "Laser-induced radiation leakage from microdroplets", Journ. Opt. Soc. Am. **10**,4 620-632 (1993)

[29] H. Chew, "Transition rates of atoms near spherical surfaces", J. Chem. Phys. **87** 2 1355-1360 (1987)

[30] H. Chew, "Radiation and lifetimes of atoms inside dielectric particles", Phys. Rev. A **38** 7 3410-3416 (1988)

[31] H. Chew, D.D. Cooke and M. Kerker, "Raman and fluorescent scattering by molecules embedded in dielectric cylinders", Appl Opt. **19** 1 44-52 (1980)

[32] H. Chew, M. Kerker and P.J. McNulty, "Raman and fluorescent scattering by molecules embedded in concentric spheres", Journ. Opt. Soc. Am. **66** 5 440-444 (1976)

[33] H. Chew, P.J. McNulty and M. Kerker, "Model for Raman and fluorescent scattering by molecules embedded in small particles", Phys. Rev. A **13** 1 396-404 (1976)

[34] H. Chew, M. Sculley, M. Kerker, P.J. McNulty and D.D. Cooke, "Raman and fluorescent scattering by molecules embedded in small particles: results for coherent optical processes", Journ. Opt. Soc. Am. **68** 12 1686-1689 (1979)

[35] H. Chew and D.-S. Wang, "Double-Resonance in Fluorescent and Raman Scattering by Molecules in Small Particles", Phys. Rev. Lett. **49** 7 490-492 (1982)

[36] S.C. Ching, H.M. Lai and K. Young, "Dielectric microspheres as optical cavities: thermal spectrum and density of states", Journ. Opt. Soc. Am. B **4** 12 1995-2003 (1987)

[37] S.C. Ching, H.M. Lai and K. Young, "Dielectric microspheres as optical cavities: Einstein A and B coefficients and level shift", Journ. Opt. Soc. Am. B **4** 12 2004-2009 (1987)

[38] D.Q. Chowdhury, S.C. Hill and P.W. Barber, "Morphology-dependent resonances in radially inhomogeneous spheres", Journ. Opt. Soc. Am. A **8** 11 1702-1705 (1991)

[39] D.Q. Chowdhury, S.C. Hill and P.W. Barber, "Time dependence of internal intensity of a dielectric sphere on and near resonance", Journ. Opt. Soc. Am. A **9** 8 1364-1373 (1992)

[40] D.Y. Chu and S.-T. Ho, "Spontaneous emission from excitons in cylindrical dielectric waveguides and the spontaneous-emission factor of microcavity ring lasers", Journ. Opt. Soc. Am. **10** (2) 381-390 (1993)

[41] P. Chylek, "Partial-wave resonances and the ripple structure in the Mie normalized extinction cross section", Journ. Opt. Soc. Am. **66** 3 285-287 (1976)

[42] P. Chylek, "Resonance structure of Mie scattering: distance between resonances", Journ. Opt. Soc. Am. A **7** 9 1609-1613 (1990)

[43] P. Chylek, A. Biswas, M.A. Jarzembski, V. Srivastava and R.G. Pinnick, "Time delay of stimulated Raman scattering of micron-size droplets", Appl. Phys. Lett. **52** 19 1642-1644 (1988)

[44] P. Chylek, J.T. Kiehl and M.K.W. Ko, "Optical levitation and partial-wave resonances", Phys. Rev. A **18** 5 2229-2233 (1978)

[45] P. Chylek, J.T. Kiehl and M.K.W. Ko, "Narrow resonance structure in the Mie scattering characteristics", Appl. Opt. **17** 19 3019-3021 (1978)

[46] P. Chylek and J.D. Klett, "Extinction cross sections of nonspherical particles in the anomalous diffraction approximation", Journ. Opt. Soc. Am. A **8** 2 272-281 (1991)

[47] P. Chylek, H.-B. Lin, J.D. Eversole and A.J. Campillo, "Absorption effects on microdroplet resonant emission structure", Opt. Lett. **16** 22 1723-1725 (1991)

[48] P. Chylek, J.D. Pendleton and R.G. Pinnick, "Internal and near-surface field of a spherical particle at resonant conditions", Appl. Opt. **24** 23 3940-3942 (1985)

[49] P. Chylek, V. Ramaswamy, A. Ashkin and J.M. Dziedzic, "Simultaneous determination of refractive index and size of spherical dielectric particles from light scattering data", Appl. Opt. **22** 15 2302-2307 (1983)

[50] P. Chylek and J. Zhan, " Interference structure of the Mie extinction cross section ", Journ. Opt. Soc. Am. A **6** 12 1846-1851 (1989)

[51] P.R. Conwell, C.K. Rushforth, R.E. Benner and S.C. Hill, "Efficient automated algorithm for the sizing of dielectric microspheres using the resonance spectrum", Journ. Opt. Soc. Am. A **1** 12 1181-1187 (1984)

[52] *C.R.C. Handbook of Chemistry and Physics*, 53rd edition, R.C. Weast, ed., The Chemical Rubber Company, Cleveland (1972)

[53] V.V. Datsyuk, "Some Characteristics of Resonant Electromagnetic Modes in a Dielectric Sphere", Appl. Phys. B **54** 184-187 (1992)

[54] J. V. Dave, "Scattering of Electromagnetic Radiation by a Large Absorbing Sphere", IBM Journ. Res Develop., May 1969, 302-313 (1969)

[55] C.C. Dobson and J.W.L. Lewis, "Survey of the Mie problem source function", Journ. Opt. Soc. Am. A **6** 3 463-466 (1989)

[56] F.J. Duarte in *Dye Laser Principles*, F.J. Duarte and L.W. Hillman, Eds., Academic, New York (1990)

[57] P.W. Dusel, M. Kerker and D.D. Cooke, "Distribution of absorption centres within irradiated spheres", Journ. Opt. Soc. Am. **69** 1 55-59 (1979)

[58] J.H. Eickmans, S.-X. Qian and R.K. Chang, "Detection of Water Droplet Size and Anion Species by Nonlinear Optical Scattering", Part. Charact. 4 85-89 (1987)

[59] K.B. Eisenthal in *Ultrashort Light Pulses*, S.L. Shapiro, Ed., Topics in Applied Physics Vol. 18, Springer-Verlag (1977)

[60] M. Essien, R.L. Armstrong and J.B. Gillespie, "Lasing emission from an evaporating layered microdroplet", Opt. Lett. **18** 10 762-764 (1993)

[61] L.B. Evans, J.C. Chen, and S.W. Churchill, "Scattering of Electromagnetic Radiation by Infinitely Long, Hollow and Coated Cylinders", Journ. Opt. Soc. Am. **54** 8 1004-1007 (1964)

[62] J.D. Eversole, H.-B. Lin and A.J. Campillo, "Cavity-mode identification of fluorescence and lasing in dye-doped microdroplets", Appl. Opt. **31** 12 1982-1991 (1992)

[63] J.D. Eversole, H.-B. Lin, A.L. Huston and A.J. Campillo, "Spherical-cavity-mode assignments of optical resonances in microdroplets using elastic scattering", Journ. Opt. Soc. Am. A **7** 12 2159-2168 (1990)

[64] L.M. Folan, "Characterization of the accretion of material by microparticles using resonant ellipsometry", Appl. Opt. **31** 12 2066-2071 (1992)

[65] D.H. Freedman, "Drawing a Bead on Superdense Data Storage", Science **255** 1213-1214 6 March 1992

[66] K.A. Fuller, "Some novel features of morphology-dependent resonances of bispheres", Appl. Opt. **28** 18 3788-3790 (1989)

[67] K.A. Fuller, "Optical resonances and two-sphere sytems", Appl. Opt. **30** 33 4716-4731 (1991)

[68] K.A. Fuller, "Scattering of light by coated spheres", Opt. Lett. **18** 4 257-259 (1993)

[69] C.G.B. Garret, W. Kaiser and W.L. Bond, "Stimulated Emission into Optical Whispering Modes of Spheres", Phys. Rev. **12** 46 1807-1809 (1961)

[70] E. Gassman, J.E. Kuo and R.N. Zare, "Electrokinetic Separation of Chiral Compounds", Science **230** 813-814 (1985)

[71] M. Golombok and D.B. Pye, "Multimode stimulated Raman scattering in fuel droplets", Chem. Phys. Lett. **151** 1,2 161-165 (1988)

[72] M. Golombok and D.B. Pye, "Droplet sizing in fuel injections by stimulated Raman scattering", Opt. Lett. **15** 15 872-874 (1990)

[73] M. Golombok and D.B. Pye, "Droplet evaporation measured by non-linear Raman method", Journ. Phys. D: Appl. Phys. **23** 1 103-1108 (1990)

[74] L.G. Guimaraes and H.M. Nussenzveig, "Theory of Mie resonances and ripple fluctuations", Opt. Comm. **8** 9 363-369 (1992)

[75] S. Haroche and D. Kleppner, "Cavity Quantum Electrodynamics", Physics Today, January 1989, pg. 24

[76] L.W. Hillman in *Dye Laser Principles*, F.J. Duarte and L.W. Hillman, Eds., Academic, New York (1990)

[77] R.L. Hightower and C.B. Richardson, "Resonant Mie scattering from a layered sphere", Appl. Opt. **27** 23 4850-4855 (1988)

[78] S.C. Hill and R.E. Benner, "Morphology-dependent resonances associated with stimulated processes in microspheres", Journ. Opt. Soc. Am. B **3** 11 1509-1514 (1986)

[79] S.C. Hill,R.E. Benner, C.K. Rushforth and P.R. Conwell, "Structural resonances observed in the fluorescence emission from small spheres on substrates", Appl. Opt. **23** 11 1680-1683 (1984)

[80] S.C. Hill, C.K. Rushforth, R.E. Benner and P.R. Conwell, "Sizing dielectric spheres and cylinders by aligning measured and computed resonance locations: algorithm for multiple orders", Appl. Opt. **24** 15 2380-2390 (1985)

[81] X.C. Huang, M.A. Quesada, and R.A. Mathies, "Capillary Array Electrophoresis Using Laser-Excited Confocal Fluorescence Detection", Anal.Chem. **64** 967-972 (1992)

[82] A.L. Huston, H.-B. Lin, J.D. Eversole and A.J. Campillo, "Nonlinear Mie scattering: electrostrictive coupling of light to droplet acoustic modes", Opt. Lett. **15** 21 1176-1178 (1990)

[83] W.-F. Hsieh, J. Zheng and R.K. Chang, "Time dependence of multiorder stimulated Raman scattering from single droplets", Opt. Lett. **13** 6 497-499 (1988)

[84] F.A. Jenkins and H.E. White, *Fundamentals of Optics*, McGraw-Hill, New York (1957)

[85] S. John, "Localization of Light", Physics Today, May 1991 32-40 (1991)

[86] B.R. Johnson, "Theory of morphology-dependent resonances: shape resonances and width formulas", Journ. Opt. Soc. Am. A **10** 2 343-352 (1993)

[87] M. Kerker, *Scattering of Light and Other Electromagnetic Radiation*, Academic, New York (1969)

[88] M. Kerker and E. Matijević, "Scattering of Electromagnetic Waves from Concentric Infinite Cylinders", Journ. Opt. Soc. Am. **51** 5 506-508 (1961)

[89] M. Kerker and S.D. Druger, "Raman and fluorescent scattering by molecules embedded in spheres with radii up to several multiples of the wavelength", Appl. Opt. **18** 8 1172-1179 (1979)

[90] M. Kerker, P.J. McNulty, M. Scully, H. Chew and D.D. Cooke, "Raman and fluorescent scattering by molecules embedded in small particles: Numerical results for incoherent optical processes", Journ. Opt. Soc. Am. **68** 12 1676-1686 (1978)

[91] D. Kleppner, "Inhibited Spontaneous Emission", Phys. Rev. Lett. **47** 4 233-236 (1981)

[92] J.C. Knight, H.S.T. Driver, R.J. Hutcheon and G.N. Robertson, "Core-resonance capillary-fiber whispering-gallery-mode laser", Opt. Lett. **17** 18 1280-1282 (1992)

[93] J.C. Knight, H.S.T. Driver and G.N. Robertson, "Interference modulation of Q-values in a cladded-fiber whispering-gallery-mode laser", Opt. Lett., in press.

[94] J.P. Kratohvil, M.-P. Lee and M. Kerker, "Angular distribution of fluorescence from small particles", Appl. Opt. **17** 13 1978-1980 (1978)

[95] M. Kuwata-Gonokami, K. Ema and K. Tadeka, "Lasing and intermode correlation of whispering-gallery mode in dye-doped polystyrene microsphere", Mol. Cryst. Liq. Cryst. **21** 6 21-25 (1992)

[96] A.S. Kwok, A. Serpengüzel, W.-F. Hsieh, R.K. Chang and J.B. Gillespie, "Two-photon-pumped lasing in microdroplets", Opt. Lett. **17** 20 1435-1437 (1992)

[97] H.M. Lai, P.T. Leung, C.K. Ng and K. Young, "Nonlinear elastic scattering of light from a microdroplet: role of electrostrictively generated acoustic vabrations", Journ. Opt. Soc. Am. B **10** 5 924-932 (1993)

[98] H.M. Lai, P.T. Leung and K. Young, "Electromagnetic decay into a narrow resonance in an optical cavity", Phys. Rev. A **37** 5 1597-1606 (1988)

[99] H.M. Lai, P.T. Leung and K. Young, "Limitations on the storage lifetime in electromagnetic resonances of highly transparent microdroplets", Phys. Rev. A **41** 9 5199-5204 (1990)

[100] C.C. Lam, P.T. Leung and K. Young, "Explicit asymptotic formulas for the positions, widths and strengths of resonances in Mie scattering", Journ. Opt. Soc. Am. B **9** 9 1585-1592 (1992)

[101] R. Lang, M.O. Scully and W.E. Lamb, "Why is the laser line so narrow? A theory of single-quasimode laser operation", Phys. Rev. A, **7** 5 1788-1797 (1973)

[102] H. Latifi, A. Biswas, R.L. Armstrong, and R.G. Pinnick, "Lasing and stimulated Raman scattering in spherical liquid droplets: time, irradiance and wavelength dependence", Appl. Opt. **29** 36 5387-5392 (1990)

[103] D.H. Leach, W.P. Acker and R.K. Chang, "Effect of the phase velocity and spatial overlap of spherical resonances on sum-frequency generation in droplets", Opt. Lett. **15** 16 894-896 (1990)

[104] D.H. Leach, R.K. Chang and W.P. Acker, "Stimulated anti-Stokes Raman scattering in microdroplets", Opt. Lett. **17** 6 387-389 (1992)

[105] E.-H. Lee, R.E. Benner, J.B. Fenn and R.K. Chang, "Angular distributionof fluorescence from monodispersed particles", Appl. Opt. **17** 13 1980-1982 (1978)

[106] C. Lei and D.G. Deppe, "Optical gain enhancement in Fabry-Perot microcavity lasers", Journ. Appl. Phys. **71** 6 2530-2535 (1992)

[107] T.R. Lettieri and W.D. Jenkins, "A Review of Ultrahigh Resolution Sizing of Single Droplets by Resonance Light Scattering" in *Liquid Particle Size Measurement Techniques*, ASTM STP848, J.M. Tishkoff, R.D. Ingebo and J.B. Kennedy, Eds.,American Society for Testing and Materials, 98-108 (1984)

[108] A.F.J. Levi, R.E. Slusher, S.L. McCall, T. Tanbun-Ek, D.L. Coblentz and S.J. Pearton, "Room temperature operation of microdisc lasers with submilliamp threshold current", Electron. Lett. **28** 11 1010-1011 (1992)

[109] B.G. Levi, "What's the shape of things to come in semiconductor lasers?", Physics Today September 1992 17-18 (1992)

[110] H.-B. Lin, J.D. Eversole and A.J. Campillo, "Identification of morphology-dependent resonances in stimulated Raman scattering from microdroplets", Opt. Commun. **77** 5,6 407-410 (1990)

[111] H.-B. Lin, J.D. Eversole and A.J. Campillo, "Frequency pulling of stimulated Raman scattering in microdroplets", Opt. Lett. **15** 7 387-389 (1990)

[112] H.-B. Lin, J.D. Eversole and A.J. Campillo, "Spectral properties of lasing microdroplets", Journ. Opt. Soc. Am. B **9** 1 43-50 (1992)

[113] H.-B. Lin, J.D. Eversole and A.J. Campillo, "Continuous-wave stimulated Raman scattering in microdroplets", Opt. Lett. **17** 11 828-830 (1992)

[114] H.-B. Lin, J.D. Eversole, C.D. Merritt and A.J. Campillo, "Cavity-modified spontaneous-emission rates in liquid microdroplets", Phys. Rev. A **45** 9 6756-6760 (1992)

[115] H.-B. Lin, A.L. Huston, J.D. Eversole and A.J. Campillo, "Double-resonance stimulated Raman scattering in micrometer-sized droplets", Journ. Opt. Soc. Am. B **7** 10 2079-2089 (1990)

[116] H.-B. Lin, A.L. Huston, J.D. Eversole, A.J. Campillo and P. Chylek, "Internal scattering effects on microdroplets resonant emission structure", Opt. Lett. **17** 14 970-972 (1992)

[117] H.-B. Lin, A.L. Huston, B.L. Justus and A.J. Campillo, "Some characteristics of a droplet whispering-gallery-mode laser", Opt. Lett. **11** 10 614-616 (1986)

[118] K.-H. Lin and W.-F. Hsieh, "Transient response of a thresholdless microdroplet dye laser", Opt. Lett. **16** 20 1608-1610 (1991)

[119] N.A. Logan, "Survey of some early studies of the scattering of plane waves by a sphere", Proc. I.E.E.E. 773-785 (1965), Reprinted in *Selected Papers on Light Scattering*, M. Kerker, Ed., SPIE Milestone series, SPIE 951 (1988)

[120] J.A. Lock, "Interference enhancement of the internal fields at structural scattering resonances of a coated sphere", Appl. Opt. **29** 21 3180-3187 (1990)

[121] J. A. Lock and L. Yang, "Interference between diffraction and transmission in the Mie extinction efficiency", Journ. Opt. Soc. Am. A **8** 7 1132-1134 (1991)

[122] Md.M. Mazumder, S.C. Hill and P.W. Barber, "Morphology-dependent resonances in inhomogeneous spheres: comparison of the layered T-matrix method and the time-independent perturbation method", Journ. Opt. Soc. Am. A **9** 10 1844-1853 (1992)

[123] S.L. McCall, A.F.J. Levi, R.E. Slusher, S.J. Pearton and R.A. Logan, "Whispering-gallery mode microdisk lasers", Appl. Phys. Lett. **60** 3 289-291 (1992)

[124] P.J. McNulty, S.D. Druger, M. Kerker and H.W. Chew, "Fluorescent scattering by anisotropic molecules embedded in small particles", Appl. Opt. **18** 10 1484-1486 (1979)

[125] J. Mevel, "Étude de la structure détailée des courbes de diffusion des ondes électromagnétiques par les sphères diélectric", Journ. de Physique et le Radium **19** 7 630-636 (1958), Reprinted in *Selected Papers on Light Scattering*, M. Kerker, Ed., SPIE Milestone series, SPIE 951, (1988)

[126] J.D. Murphy, P.J. Moser, A. Nagl and H. Uberall, "A Surface Wave Interpretation for the Resonances of a Dielectric Sphere", I.E.E.E. Trans. Antennas Propag. **AP-28** 6 924-927 (1980)

[127] J.F. Owen, P.W. Barber and R.K. Chang, "Morphology-dependent Raman spectra from microparticles" in *Microbeam Analysis*, K.F. Heinrich, Ed., San Francisco Press, San Francisco (1982)

[128] J.F. Owen, P.W. Barber, P.B. Dorain and R.K. Chang, "Enhancement of Fluorescence Induced by Microstructure Resonances of a Dielectric Fiber", Phys. Rev. Lett. **45** 15 1075-1078 (1981)

[129] J.F. Owen, P.W. Barber, B.J. Messinger and R.K. Chang, "Determination of optical-fiber diameter from resonances in the elastic-scattering spectrum", Opt. Lett. **6** 6 272-274 (1980)

[130] J.F. Owen, R.K. Chang and P.W. Barber, "Internal electric field distributions of a dielectric cylinder at resonance wavelengths", Opt. Lett. **6** 11 540-542 (1981)

[131] J.F. Owen, R.K. Chang and P.W. Barber, "Morphology-Dependent Resonances in Raman Scattering, Fluorescence Emission, and Elastic Scattering from Microparticles", Aerosol Sci. Technol. 1 293-302 (1982)

[132] R.G. Pinnick, A. Biswas, R.L. Armstrong, H. Latifi, E. Creegan, V. Srivastava, M. Jarzembski and G. Fernandez, "Stimulated Raman scattering in micrometer-sized droplets: time-resolved measurements", Opt. Lett. **13** 6 494-496 (1988)

[133] R.G. Pinnick, A. Biswas, R.L. Armstrong, H. Latifi, E. Creegan, V. Srivastava and G. Fernandez, "Stimulated Raman scattering in micrometer-sized droplets: measurements of angular scattering characteristics", Opt. Lett. **13** 12 1099-1101 (1988)

[134] R.G. Pinnick, G.L. Fernandez, J.-G. Xie, T.E. Ruekgauer, J. Gu and R.L. Armstrong, "Stimulated Raman scattering and lasing in micrometer-sized cylindrical liquid jets: time and spectral dependence", Journ. Opt. Soc. Am. B **9** 6 865-870 (1992)

[135] A.B. Pluchino, "Emissivity spectra of composite microscopic particles" Appl. Opt. **20** 4 531-533 (1981)

[136] A.B. Pluchino, "Surface waves and the radiative properties of micron-sized particles", Appl. Opt. **20** 17 2986-2992 (1981)

[137] R.E. Preston, T.R. Lettieri and H.G. Semerjian, "Characterization of Single Levitated Droplets by Raman Spectroscopy", Langmuir **1** 3 365-367 (1985)

[138] J.R. Probert-Jones, "Resonance component of backscattering by large dielectric spheres", Journ. Opt. Soc. Am. A **1** 8 822-830 (1984)

[139] I.E. Psarobas and K.M. Leung, "Morphology-dependent resonances in a large dielectric sphere: An asymptotic calculation using local coordinates", Phys. Rev. A **46** 4 2111-2116 (1992)

[140] S.-X. Qian and R.K. Chang, "Phase-modulation broadened line shapes from micrometer-size CS_2 droplets", Opt. Lett. **11** 6 371-373 (1986)

[141] S.-X. Qian and R.K. Chang, "Multiorder Stokes Emission from Micrometer-Size Droplets", Phys. Rev. Lett. **56** 9 926-929 (1986)

[142] S.-X. Qian, J.B. Snow and R.K. Chang, "Coherent Raman mixing and coherent anti-Stokes Raman scattering from individual micrometer-size droplets", Opt. Lett. **10** 10 499-501 (1985)

[143] S.-X. Qian, J.B. Snow, H.-M. Tzeng and R.K. Chang, "Lasing Droplets: Highlighting the Liquid-Air Interface by Laser Emission", Science **231** 486-488 31 January 1986

[144] Lord Rayleigh, "On the electromagnetic theory of light", Phil. Mag. **12** 81-101 (1881), reprinted in *Scientific Papers*, Vol. 1, Cambridge University Press, Cambridge (1899-1920)

[145] Lord Rayleigh, "The problem of the whispering gallery", Phil. Mag **XX** 1001-1004 (1910) , reprinted in *Scientific Papers*, Vol. 5, Cambridge University Press, Cambridge (1899-1920)

[146] G.J. Rosasco and H.S. Bennet, "Internal field resonance structure: Implications for optical absorption and scattering by microscopic particles", Journ. Opt. Soc. Am. **68** 9 1242-1250 (1978)

[147] A. Saissy, D.B. Ostrowsky and G. Maze, "Fluorescence in rare earth-doped fluorozirconate fibers", Appl.Opt. **30** 15 1933-1938 (1991)

[148] F.P. Schäfer in *Dye Lasers*, F.P. Schäfer, Ed., Topics in Applied Physics Vol. 1, 3rd ed., Springer Verlag, Berlin (1990)

[149] S. Schiller and R.L. Byer, "High-resolution spectroscopy of whispering-gallery modes in large dielectric spheres", Opt. Lett. **16** 15 1138-1140 (1991)

[150] B. Schlicht, K.F. Wall, R.K. Chang and P.W. Barber, "Light scattering by two parallel glass fibers", Journ. Opt. Soc. Am. A **4** 5 800-808 (1987)

[151] G. Schweiger, "In-situ Determination of the Molecular Composition of Aerosol Particles in a monodisperse Model Aerosol", Part. Charact. **4** 67-73 (1987)

[152] G. Schweiger, "Observation of input and output structural resonances in the Raman spectrum of a single spheroidal dielectric particle", Opt. Lett. **15** 3 156-158 (1990)

[153] G. Schweiger, "Raman scattering on microparticles: size dependence", Journ. Opt. Soc. Am. B **8** 8 1770-1778 (1991)

[154] A. Serpengüzel, G. Chen and R.K. Chang, "Stimulated Raman scattering of aqueous droplets containing ions: concentration and size determination", Part. Sci. Technol. **8** 179-189 (1990)

[155] A. Serpengüzel, G. Chen, R.K. Chang and W.-F. Hsieh, "Heuristic model for the growth and coupling of nonlinear processes in droplets", Journ. Opt. Soc. Am. B **9** 6 871-883 (1992)

[156] A.E. Siegman, *Lasers*, Oxford University Press, Oxford (1986)

[157] J.B. Snow, S.-X. Qian and R.K. Chang, "Stimulated Raman scattering from individual water and ethanol droplets at morphology-dependent resonances", Opt. Lett. **10** 1 37-39 (1985)

[158] G.L. Stephens, "Scattering of plane waves by soft obstacles: anomalous diffraction theory for circular cylinders", Appl.Opt. **23** 6 954-959 (1984)

[159] J.A. Stratton, *Electromagnetic Theory*, McGraw-Hill, New York (1941)

[160] O. Svelto, *Principles of Lasers*, Plenum, New York (1982)

[161] C.-T. Tai, *Dyadic Green's Functions in Electromagnetic Theory*, Intext, San Francisco (1971)

[162] C.C.H. Tang, "Backscattering from Dielectric-Coated Infinite Cylindrical Obstacles", Journ. Appl. Phys. **28** 5 628-633 (1957)

[163] R. Thurn and W. Kiefer, "Raman-Microsampling Technique Applying Optical Levitation by Radiation Pressure", Appl. Spectr. **38** 1 78-83 (1984)

[164] R. Thurn and W.F. Kiefer, "Structural resonances observed in the Raman spectra of optically levitated liquid droplets", Appl. Opt. **24** 10 1515-1519 (1985)

[165] T.-G. Tsuei and P.W. Barber, "Multiple scattering by two parallel dielectric cylinders", Appl. Opt. **27** 16 3375-3381 (1988)

[166] H.-M. Tzeng, M.B. Long, R.K. Chang and P.W. Barber, "Laser-induced shape distortions of flowing droplets deduced from morphology-dependent resonances in fluorescence spectra", Opt. Lett. **10** 5 209-211 (1985)

[167] H.-M. Tzeng, K.F. Wall, M.B. Long, R.K. Chang, "Evaporation and condensation rates of liquid droplets deduced from structure resonances in the fluorescence spectra", Opt. Lett. **9** 7 273-275 (1984)

[168] H.-M. Tzeng, K.F. Wall, M.B. Long and R.K. Chang, "Laser emission from individual droplets at wavelengths corresponding to morphology-dependent resonances", Opt. Lett. **9** 11 499-501 (1984)

[169] H.C. van de Hulst, *Light Scattering by Small Particles*, Dover, New York (1981)

[170] G. Videen, W.S. Bickel and J.M. Boyer, "Coherent fluorescent emission and scattering from a uniform cylinder", Phys. Rev. **43** 10 5655-5664 (1991)

[171] W.J. Wiscombe, "Mie Scattering Calculations: Advances in Technique and Fast, Vector-Speed Computer Codes", NCAR Technical Note, NCAR/TN-140+STR, National Center for Atmospheric Research, Boulder, Colorado (1979)

[172] A. Yariv, *Quantum Electronics*, Wiley, New York (1967)

[173] H. Yokoyama, "Physics and Device Applications of Optical Microcavities", Science **256** 66-70, 3 April 1992

[174] H. Yokoyama and S.D. Brorson, "Rate equation analysis of microcavity lasers", Journ. Appl. Phys. **66** 10 4801-4805 (1989)

[175] J.-Z. Zhang and R.K. Chang, "Shape distortion of a single water droplet by laser-induced electrostriction", Opt. Let. **13** 19 916-918 (1988)

[176] J.-Z. Zhang and R.K. Chang, "Generation and suppression of stimulated Brillouin scattering in single liquid droplets", Journ. Opt. Soc. Am. B **6** 2 151-153 (1989)

[177] J.-Z. Zhang, D.H. Leach and R.K. Chang, "Photon lifetime within a droplet: temporal determination of elastic and stimulated Raman scattering", Opt. Lett. **13** 4 270-272 (1988)